ABSTRACT

A STUDY OF ^{192,194,196,198}Pt USING THE (p,t) AND (p,p') REACTIONS AND THE INTERACTING BOSON APPROXIMATION MODEL

by

Paul Thomas Deason, Jr.

The low-lying collective states of the ^{192,194,196,198}Pt nuclei have been studied with the (p,t) and (p,p') reactions at E_p = 35 MeV. Approximately 45 levels were populated below 3 MeV for each nucleus in both reactions, with many levels seen for the first time. Angular distributions have been obtained in each reaction using a delay-line proportional counter in the focal plane of an Enge split-pole spectrograph and accurate energies were obtained from high-resolution, nuclear emulsion plate data. Distorted-wave Born approximation (DWBA) calculations were performed for transitions in the ^{194,196,198}Pt(p,t)^{192,194,196}Pt reactions, and were used, in addition to empirical angular distribution shapes, to make J^π assignments. No new levels were seen below 1.5 MeV excitation. A new state with $J^\pi = 0^+$ at 1.628 MeV was found in ^{192}Pt and new levels tentatively assigned $J^\pi = 4^+$ were seen in all three final nuclei near 1.9 MeV. In ^{196,198}Pt(p,t), these 4^+ levels are populated with 15% of the

ground state strength at 7^{o}. Enhancement factors, ε, were calculated for simple two-neutron pickup configurations.

A comparison is made between experimental (p,t) strengths and those calculated in the O(6) limit of the interacting boson approximation (IBA) model for L = 0 and L = 2 transitions. The calculations included a small, quadrupole-quadrupole symmetry breaking term and allowed for both neutron and proton bosons. The calculations are generally in good agreement with the data, particularly the prediction that the second excited 0^{+} level should be more strongly populated than the first excited 0^{+} level.

In the inelastic proton scattering studies, high resolution data are presented for ^{194,196,198}Pt. In ^{198}Pt thirty-eight of the forty-four levels seen are reported for the first time. Assignments of J^{π} were made in each reaction by comparisons of angular distributions to those for states with well-known spin and parity. Coupled channels calculations have been performed for each reaction using a deformed optical model potential for the radial form factors, with relative matrix elements obtained from the IBA model near the O(6) limit. Good fits to the data are obtained for the ground band (up to spin 4) and second 2^{+} level. Best fits are obtained in ^{194,196}Pt with a negative value for the interference term P_3 (= $M_{02}M_{22}M_{02'}$), in agreement with recent (α,α') studies of ^{194}Pt and with the predictions of the O(6) limit of the IBA model. To explain the strength of

the second 4^+ state in all three reactions a large value for M_{04}, is needed, indicating a strong, direct E4 transition competes with the various multi-step paths.

The quadrupole (E2) and hexadecapole (E4) potential moments have been calculated from the parameters of the deformed optical model potential used in the inelastic proton scattering. The moments are in better agreement with the charge moments from Coulomb excitation in each case than those from the potential moments calculated from alpha scattering. This may indicate that inelastic proton scattering is a more reliable method for extracting potential moments than α-scattering due to the more complex intrinsic structure of the alpha particle.

A STUDY OF ^{192,194,196,198}Pt USING THE (p,t) AND (p,p') REACTIONS AND THE INTERACTING BOSON APPROXIMATION MODEL

by

Paul Thomas Deason, Jr.

A DISSERTATION

Submitted to
Michigan State University
in partial fulfillment of the requirements
for the degree of

DOCTOR OF PHILOSOPHY

Department of Chemistry

1979

To my family:

Kimberly and Debbie,

Ed, Pam, Nancy, Mom, and Dad

ACKNOWLEDGMENTS

I am most thankful to Dr. Fred Bernthal, who served as my research advisor, for his friendship, advice, and genuine interest in this project, myself, and my future. His guidance and advice will always be welcome.

I am also pleased to acknowledge the teaching and guidance of Drs. Chuck King and Reg Ronningen, who provided the day-to-day interactions and discussions which have contributed so much to my graduate school education. I consider myself very fortunate to have worked with such authorities in this area of nuclear science.

Many thanks are due Drs. Teng Lek Khoo and Jerry Nolen, for their many hours of help in taking the data for this dissertation and sharing their expertise on the experimental electronics and the operation of the MSU cyclotron.

I would like to thank Dr. Henry Blosser and the staff of the MSU Cyclotron Laboratory for providing and maintaining a truly unique experimental facility and research environment.

I am most grateful to Richard Au and the computer staff for keeping the Sigma-7 alive and well and for those extra hours of computing time on maintenance days.

Financial support in the form of a Quill Fellowship from the MSU Chemistry Department and the Eastman Kodak Company

and numerous research assistantships funded by the Energy Research and Development Administration and the National Science Foundation is gratefully acknowledged.

Thanks to the Nuclear Beer Group and "Athletic Club" for those memorable Friday afternoons and unforgettable night games - but mostly for your friendship and good times during the last five years.

I would also like to thank Norval Mercer for his special kindness to myself and family and for teaching an ACC fan the merits of the Big 10.

A special thanks is due Earvin and Greg for making the Winters of '78 and '79 more than just long and cold.

Many thanks are in order for Mrs. Carol Cole for her efforts in the typing of this thesis. Her skills are evident throughout the entire text. Her willingness to complete this task before her "deadline" as well as mine is appreciated.

I especially thank my parents, my lifelong teachers, for their encouragement, advice, and love.

Most of all, I wish to thank my wife, Debbie, for her many sacrifices, for her understanding of my hours away from home, and especially for her love and unselfishness for Kim and myself.

TABLE OF CONTENTS

LIST OF TABLES

LIST OF FIGURES

CHAPTER I

INTRODUCTION

A. Orientation

The Pt isotopes lie in a shape transitional region, between well-deformed rare-earth nuclei and the spherical nuclei near doubly magic ^{208}Pb. Since the Pt nuclei are not well described by simple model limits for collective nuclear motion (e.g. the symmetric rotor or the harmonic vibrator), they provide a valuable testing ground for more current models.

Figure I–1 shows the low-lying energy levels for three of the four Pt nuclides studied in this work. The first item one notes is the similarity of the levels from ^{192}Pt to ^{196}Pt. Most of the levels decrease or increase in energy very gradually in these nuclei, part of the evidence for the slowly changing shape characteristics in this region. Within a particular nucleus the most obvious features are the nearly equal spacing between the first three levels, and the low-lying second 2^+ state. Understanding these relatively simply systematics, along with the many electromagnetic branching ratios, has provided the framework for comparing the predictions of several nuclear models.

Figure I-1. Systematics of Experimentally Determined Energy Levels for Positive Parity States in ^{194,196,198}Pt.

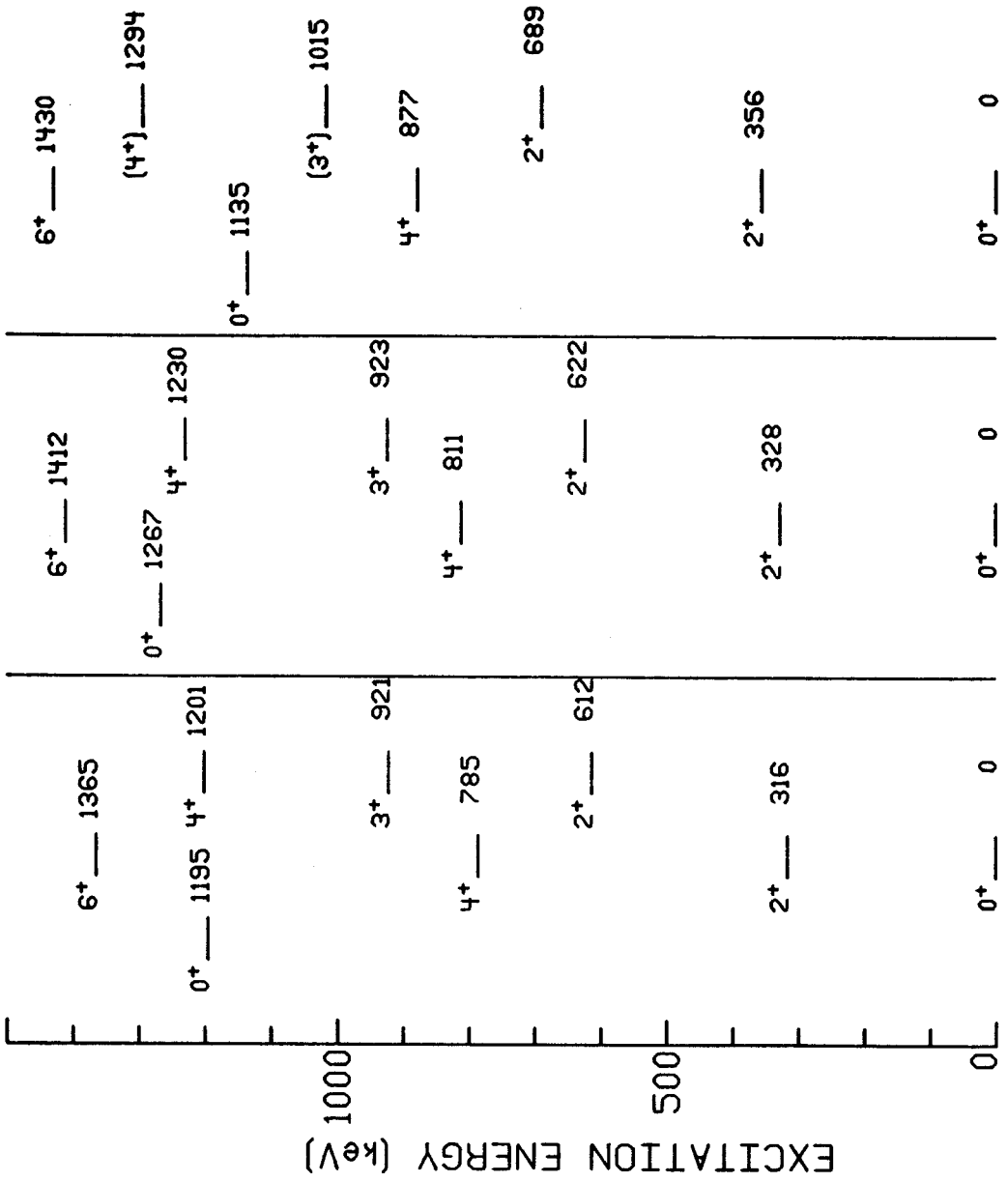
EXCITATION ENERGY (keV)
1000
500
0
192Pt
194Pt
196Pt
6+ 1365
0+ 1195
4+ 1201
3+ 921
4+ 785
2+ 612
2+ 316
0+ 0
6+ 1412
0+ 1267
4+ 1230
3+ 923
4+ 811
2+ 622
2+ 328
0+ 0
6+ 1430
(4+) 1294
0+ 1135
(3+) 1015
4+ 877
2+ 689
2+ 356
0+ 0

Figure I-1.

It has been known for several years that a transition from prolate (negative quadrupole moment) to oblate (positive quadrupole moment) shapes occurs among the heavier Os and the lighter Pt nuclides [Gl 68, Gl 69, Pr 70]. For the heavier Pt nuclides ($^{192-198}$Pt) the quadrupole deformation parameter, β, has a value [Ba 76, Ba 78] of approximately 0.15, or about one-half the value determined for the well-deformed rare earth nuclei. Consequently, these Pt isotopes exhibit few rotational features. Some aspects of the lowest energy levels of these nuclides, such as the nearly equal level spacings and a small $2_2^+ \rightarrow 0_1^+$ transition, can be interpreted in terms of a harmonic vibrator. However, a notable problem with this picture is the lack of a candidate for the 0^+ member of the 2-phonon triplet. Moreover, the platinum isotopes are farther away from closed shells than those nuclei for which vibrational models have been applied most successfully.

Because of the difficulty with vibrational models, various other collective models have been explored, such as the γ-unstable [Wi 56] or the asymmetric [Da 58] rotor models. These models predict only one 0^+ state (the ground state) and allow the second 2^+ state (2_2^+) to be degenerate with or below the energy of the first 4^+. Figure I-1 shows that the Pt nuclides display both these features.

The asymmetric rotor model [Me 75, To 76, Do 77, Pa 77, Sa 77] has had considerable success in describing the odd-A nuclei in the Pt region by coupling the odd particle to a

triaxial core. However, the predictions for this approach have been shown to be experimentally indistinguishable thus far from those obtained by a variety of other particle core couplings [Do 77, Pa 77], including that for a γ-unstable core. Several attempts [Ku 68, Gn 71, Le 76] have been made to treat this region by solving the full Bohr-Hamiltonian, beginning with the work of Kumar and Baranger [Ku 68] in which the parameters of the Hamiltonian were determined by using the pairing-plus-quadrupole (PPQ) model. The PPQ model has demonstrated considerable success in predicting the prolate-to-oblate shape transition, but only addresses the properties of lower energy levels. It also predicts the potential energy surface to be γ-soft. This is one of several predictions of γ-soft potentials in the Os-Pt region. (Another model with similar predictions for the Pt nuclei is the boson expansion technique of Kishimoto and Tamura [Ki 72, Ki 76].) One problem with these more complete treatments of the collective properties of heavy nuclei is the rather complex numerical methods needed to solve the Hamiltonians.

A simpler description of the nuclides in the Pt-Os region has recently emerged from the interacting boson approximation (IBA) model of Arima and Iachello [Ar 76, Ar 78, Ia 78, Sc 78]. In this model the emphasis is on the symmetries of the nuclear structure rather than the geometry, while also including the finite dimensionality of the subshells. The IBA model treats the nucleus in terms of a set

of bosons, one for each pair of neutrons or protons outside a closed shell. The bosons can be in either of two states, denoted by their angular momentum, L = 0 or L = 2 (s or d bosons), and are allowed to interact.

The most general Hamiltonian describing such a system possesses an SU(6) group symmetry. Particularly simple descriptions are possible when the Hamiltonian is symmetric with respect to subgroups of SU(6). Analytical solutions have been found for both the energy levels and electromagnetic transitions for three subgroups, SU(5), SU(3), and O(6). These symmetries are applicable at the beginning, middle, and end of shells respectively. The SU(5) subgroup corresponds approximately to the vibrational limit of the collective model, and SU(3) to the rotational limit. The third limiting symmetry, O(6), is most like the γ-unstable model of Wilets and Jean [Wi 56]. It has been shown by Cizewski et al. [Ci 78] that this limit is capable of accounting for most of the energy and decay properties of all positive parity levels below the pairing gap for ^{196}Pt. Moreover, it predicts no 0^+ level with 2-phonon components near the 4^+ and 2_2^+ level, and it has no equivalent to the 3-phonon 2^+ level. In fact, the structure of ^{196}Pt and most of the lighter mass even-even Os and Pt nuclides can be understood [Ca 78] by adding a small but gradually increasing symmetry-breaking term to the Hamiltonian as one goes further away from the O(6) limit. This A-dependent deviation from

the O(6) limit is predicted to occur within the more complete SU(6) representation of the IBA.

The majority of the experimental information on the heavier Pt isotopes has come from γ-ray studies following the $\varepsilon,\beta^{\pm}$ decay of Au and Ir isotopes [Be 64, Ny 66, Ja 68, Be 70, Fi 72, Cl 76]. There have also been several publications on γ-decay following neutron capture [Gr 68, Sa 68, Su 68, Ci 79]. More recently the nature of the high-spin levels of the platinum nuclides up to spin 20 has been studied by (α,xnγ) in-beam γ-ray spectroscopy [Ya 74, Fu 75, Hi 76, Sa 77].

There have been numerous inelastic scattering experiments [Gl 68, Ba 76, Le 77, Ro 77, St 77, Ba 78, Ba 78a] performed on the Pt nuclides, primarily by Coulomb excitation of the first 2^+ states. However, three more detailed Coulomb excitation studies have recently been performed yielding conflicting conclusions when the results are interpreted in terms of various models. Lee et al. [Le 77] see evidence for a stable triaxial shape, Baktash et al. [Ba 78a] favor the PPQ model, while the third study proved inconclusive [St 77]. The bulk of the transfer reaction data is from one-neutron transfer studies of the odd-A platinum nuclei [Mu 65, Ya 76, Sm 77, Be 78, Ya 78], but there have been searches for strong L = 0 transitions in the $^{190-196}$Pt(p,t) reactions [Ma 72, Ve 76, Ve 78].

B. Motivation

When this study began, most of the information on the Pt region was obtained from decay works and Coulomb excitation of the first 2^+ states. The intention of this study was to utilize the high resolution capabilities of the Michigan State University cyclotron in collecting transfer reaction data on the even-even Pt nuclides to complement the existing data. The (p,t) and (p,p') reactions were chosen because both reactions populate primarily the collective levels of a nucleus and it is this type of state that most models of heavier nuclei attempt to explain. Specifically, the (p,t) reaction was chosen for the distinctive, diffractive angular distributions of tritons from the L = 0 transfers, which populate $J^\pi = 0^+$ levels in the residual nucleus when using even-even targets. Information on the spin and parity of these and other states seen in transfer reactions are obtained by interpreting the shapes of the transitions in terms of the distorted-wave Born approximation (DWBA) reaction formalisms. The low-lying 0^+ states play an important role in any attempt to distinguish the models mentioned above, although additional information on branching ratios from the decay of these states is also necessary.

In addition to locating the 0^+ states, the strength of the transition populating such states in a (p,t) reaction can also provide information on the shape of a nucleus, as was seen in the Sm isotopes [Bj 66]. If the ground states of Os

or Pt nuclei are relatively rigid in the γ-direction, and γ varies rapidly, strong L = 0 transitions are expected to populate excited 0^+ levels, which have shapes similar to the target ground state. However, Sharma and Hintz [Sh 76] observe no strong L = 0 transitions in the Os nuclei, possibly because the γ shape parameter appears to be changing slowly. The present study would extend this search into the Pt isotopes.

The (p,p') reaction study was initiated as a probe of the macroscopic structure of the transitional Pt nuclides. Techniques have been established for determining deformation parameters and charge/potential moments from such inelastic scattering studies. These experimental parameters, obtained using matrix elements from some nuclear model, can then be used to determine the shape of the nucleus. The procedure has primarily been used for well deformed nuclei in (α,α') experiments. The work described here, along with (p,p') experiments on well deformed rare-earths and actinide nuclei at this laboratory [Ki 78], is an attempt to extend the technique from alpha [He 68, Ba 76] to proton scattering (which is now thought to be a better probe of the nuclear matter distribution than high energy (α,α') experiments [Ha 77]). The most widely used code for analyzing inelastic scattering data, ECIS [Ra 73], is capable of calculating several different sets of matrix elements, thus affording an excellent means of testing several models by using them to interpret scattering data.

The (p,p') study also complements the two-nucleon transfer study because each reaction populates collective states, particle-hole types in (p,p') and two-particle or two-hole configurations in (p,t). Due to these similarities, one would expect to see some correlation between the levels populated in each reaction and thus aid in the assignment of spin and parity for new levels.

C. Organization

The next two chapters of this dissertation are an introductory discussion of the theoretical background used in the study. Chapter II deals with the primary nuclear models used in the remainder of the text, while in Chapter III the theoretical methods of describing nuclear reactions and calculating transition strengths and shapes are presented, including the standard Distorted-Wave Born Approximation and the method of coupled channels for inelastic scattering. Chapter IV discusses the experimental procedures and the methods used in the data analysis.

In Chapters V and VI the experimental results are presented for the ^{194,196,198}Pt(p,t)^{192,194,196}Pt and ^{194,196,198}Pt(p,p') reactions, respectively. Also included in each chapter is an interpretation of the results, primarily with the O(6) limit of the interacting boson approximation model. The last chapter is a summary of the

results for both sets of reactions and a discussion of the effectiveness of the IBA model in explaining the data.

CHAPTER II

THEORETICAL BACKGROUND - NUCLEAR MODELS

A. Introduction

When one is studying a complex problem or situation where all the forces or variables involved are not known, some type of model is usually used to gain insight, answers, and ultimately predictions. The study of the nucleus is an excellent example of this situation. First, the nucleus must be handled as a many-body problem ($A > 2$, of course), which has no analytical solution. But the situation is even more complex than the atomic many-body problem because of the complicated nature of the nuclear force. The force between nucleons is very strong, with many complexities. In the atomic case the force involved is the simple electrostatic force between charged particles. Second, the dynamics involved in the nucleus are extremely complex due to the high particle density and the short range of the nuclear force.

These complexities thus compel one to use a model to describe the nucleus and to predict experimental quantities. In the past forty years there have been numerous models developed in an attempt to understand the nucleus. For the

most part, these models work well only for limited special cases because of assumptions that are necessarily made to make the problem tractable. There are basically two kinds of models: one describing the particle-like or intrinsic features of nuclei; the other deals with the collective features often exhibited by heavier nuclei. This section will concern itself with the latter kind of model because of the collective nature of the Pt nuclides and also because the reactions employed in this study, (p,t) and (p,p'), are probes of collective structure. Extensive detail is not necessary as there exist many classic works and review articles on the subject [Bo 53, Da 58, Bo 69, Pr 75, Ra 75].

The most widely used model for collective nuclei is the phenomenological, hydrodynamic model of Bohr and Mottelson [Bo 53, Bo 69]. The nucleons are treated as a deformable liquid drop, whose macroscopic properties such as surface tension, volume, and Coulomb energy are included in the total Hamiltonian. Two idealized limits arise, one due to vibrational modes and the other from rotations. The vibrational model applies in first order to spherically shaped nuclei, where the nuclear excitations (of a collective nature rather than intrinsic) are assumed to be small-amplitude, harmonic vibrations about the equilibrium spherical shape. In the rotational model, which best describes well deformed nuclei in the middle of shells, two collective modes of excitation are considered, viz. rotations and small vibrations of a permanently deformed system.

B. The Vibrational Model

The usual parameterization of the surface of a distorted body involves an expansion in terms of spherical harmonics,

$$R = R_o[1 + \sum_{\lambda\mu} \alpha_{\lambda\mu}(t) Y_{\lambda\mu}(\theta,\phi)] \ , \qquad \text{(II-1)}$$

where the $Y_{\lambda\mu}$ are the spherical harmonics expressed in terms of the laboratory angles θ and ϕ, and the $\alpha_{\lambda\mu}$ are time-dependent parameters defining the distortion of a sphere of volume $4/3\ \pi R_o^3$. The kinetic energy, T, can be expressed as

$$T = \frac{1}{2} \sum_{\lambda\mu} B_\lambda |\dot{\alpha}_{\lambda\mu}|^2 \qquad \text{(II-2)}$$

and the potential energy V as,

$$V = \frac{1}{2} \sum_{\lambda\mu} C_\lambda |\alpha_{\lambda\mu}|^2 \ , \qquad \text{(II-3)}$$

where the B_λ are "mass parameters" and the C_λ are the vibrational "force constants". Values are determined either empirically or via some microscopic model. The total Hamiltonian for this system is given by

$$H = \frac{1}{2} \sum_{\lambda\mu} [B_\lambda |\dot{\alpha}_{\lambda\mu}|^2 + C_\lambda |\alpha_{\lambda\mu}|^2] \ , \qquad \text{(II-4)}$$

which corresponds to a set of uncoupled harmonic oscillators with frequencies, ω_λ

$$\omega_\lambda = (C_\lambda/B_\lambda)^{1/2}, \ \lambda \geq 2 \ , \qquad \text{(II-5)}$$

where λ is associated with the order of the excitation and also the magnitude of the angular momentum. The modes

arising from $\lambda = 0$ and $\lambda = 1$ have been neglected since $\lambda = 0$, the compression mode, corresponds to a volume change of the nucleus and $\lambda = 1$ refers to a translation of the center of mass of the nucleus. The energy levels of this simple harmonic oscillator are given by

$$E_\lambda = \hbar\omega_\lambda \sum_\mu (n_{\lambda\mu} + 1/2) \ , \qquad \text{(II-6)}$$

where $n_{\lambda\mu}$ is the number of vibrational quanta, called phonons, which have angular momentum λ and parity $(-1)^\lambda$.

Thus, the energy spectrum of a simple vibrator has a ground state with zero phonons and spin and parity $J^\pi = 0^+$. The first excited state has one $\lambda = 2$ phonon with an energy of $\hbar\omega_2$ and $J^\pi = 2^+$. Since one $\lambda = 3$ phonon has nearly the same energy as two $\lambda = 2$ phonons, the next excited state, which appears at $2\hbar\omega_2$, could be either a 3^- state or the three degenerate states formed via the coupling of two quadrupole phonons. In practice these states are not degenerate due to anharmonicities, so the third excited state could be either the 3^- state mentioned above or a 0^+, 2^+, or 4^+ state from the 2-phonon triplet.

Some of the electromagnetic properties of this model include: (i) strong E2 transitions from the first excited 2^+ state to the ground state as well as from the members of the three phonon triplet to the first 2^+ state, (ii) no E2 transition from the second 2^+ state to the ground state, and (iii) no quadrupole moment for the first 2^+ level. The

nuclei which should exhibit these energy and decay properties lie near the closed shells, far from the strongly deformed regions and should be nearly spherical.

C. The Symmetric Rotor Model

Measurements of the quadrupole moments of nuclei have shown that the larger values occur in the region between major shell closures. This implies that these nuclei are not spherical, but ellipsoidal, and one would expect to see energy and decay properties quite different from those of a spherical vibrator. These strongly deformed nuclei exhibit a rotational structure much like that seen in molecules. To describe such nuclei in the Bohr-Mottelson model the nucleus is assumed to be strongly deformed with axial symmetry. The expansion of the nuclear surface is handled in a fashion similar to the spherical case except that the $\alpha_{\lambda\mu}$ parameters are replaced by $a_{\lambda\mu}$ values related to the body-fixed system and the Euler angles $(\theta_1, \theta_2, \theta_3)$ of the principal axes of the nucleus with respect to the space-fixed axes.

Thus, for quadrupole ($\lambda = 2$) shapes the nuclear surface can be expressed as

$$R = R_o[1 + \sum_{\mu} a_{2\mu} Y_{2\mu}(\theta', \phi')] \ . \qquad \text{(II-7)}$$

The axes of the body-fixed frame are chosen such that $a_{21} = a_{2,-1} = 0$ and $a_{22} = a_{2,-2}$. So for the rotational system, a_{20}, a_{22} along with the three Euler angles are used

to describe the system rather than the five $\alpha_{\lambda\mu}$ variables. For later convenience, a_{20} and a_{22} are defined in terms of two new parameters β and γ:

$$a_{20} = \beta\cos\gamma, \quad a_{22} = \frac{\beta}{\sqrt{2}}\sin\gamma \ . \tag{II-8}$$

The significance of β and γ can best be shown by the value of $R(\theta',\phi') - R_o$ along each axis

$$R(\theta',\phi') - R_o = \delta R_k = \frac{\sqrt{5}}{\sqrt{4\pi}}\beta R_o\cos(\gamma - \frac{2\pi k}{3}), \quad k = 1,2,3 \ , \tag{II-9}$$

where k represents the body-fixed axes, x', y', and z'. From (II-9) one sees that β is a measure of the size of the deformation,the departure of the nucleus from sphericity. The value of γ determines the type of ellipsoid. For values of $\gamma = 0$ or multiples of $\pi/3$, there is one axis of symmetry. With $\beta > 0$ and $\gamma = 0, 2\pi/3, 4\pi/3$ a prolate (football) shape is obtained, while for $\beta > 0$ and $\gamma = \pi, \pi/3, 5\pi/3$ an oblate (doorknob) shaped ellipsoid is formed. If $\beta < 0$ the two shapes would be reversed in the examples above. For other values of γ there is no symmetry axis in the nucleus. This case (asymmetric rotor) will be discussed in the next section. Now one can discuss the shape of a nucleus in a two dimensional $\beta-\gamma$ plane, which can be reduced to a 60^o sector of polar coordinates due to the symmetries about $\pi/3$. Figure II-1 shows a schematic view of this 60^o sector.

To derive an expression for the energy levels of a symmetric rotor the terms of the Bohr-Mottelson Hamiltonian

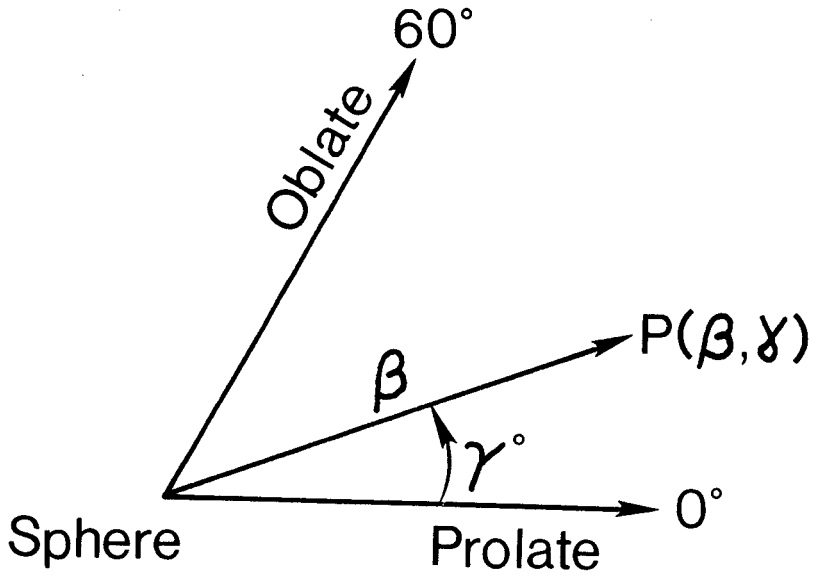

Figure II-1. A 60^{o} Sector of the β-γ Plane. The point P represents an asymmetric shape with magnitude β and an asymmetry parameter γ.

must be recast in terms of the body-fixed frame. After this transformation the expression for the kinetic energy is given by

$$T = \frac{1}{2} B(\dot{\beta}^2 + \beta^2\dot{\gamma}^2) + \frac{1}{2} \sum_{k=1}^{3} I_k\omega_k^2 , \qquad \text{(II-10)}$$

where ω is the angular velocity of the principal axes with respect to the space-fixed axes and I, the effective moment of inertia, is given by

$$I_k = 4B\beta^2 \sin (\gamma - \frac{2\pi k}{3}) . \qquad \text{(II-11)}$$

The first term of Equation (II-10) represents the vibrational energy and the second term is the rotational contribution. The potential energy can be expressed in terms of the β-γ plane mentioned earlier so that the total Hamiltonian has the form

$$H = T_\beta + T_\gamma + T_R + V(\beta,\gamma) . \qquad \text{(II-12)}$$

From this general Hamiltonian, solutions for both the rotational and vibrational limits can be obtained. For a spherical nucleus,

$$V(\beta,\gamma) \rightarrow V(\beta) = \frac{1}{2} C\beta^2 \qquad \text{(II-13)}$$

is obtained straightforwardly from Equation (II-3). Substituting this expression into (II-12) leads to the same energy spectrum obtained in the previous section for a vibrational nucleus (see Figure (II-2)). If one assumes that β and γ change very little, which implies a very steep $V(\beta,\gamma)$

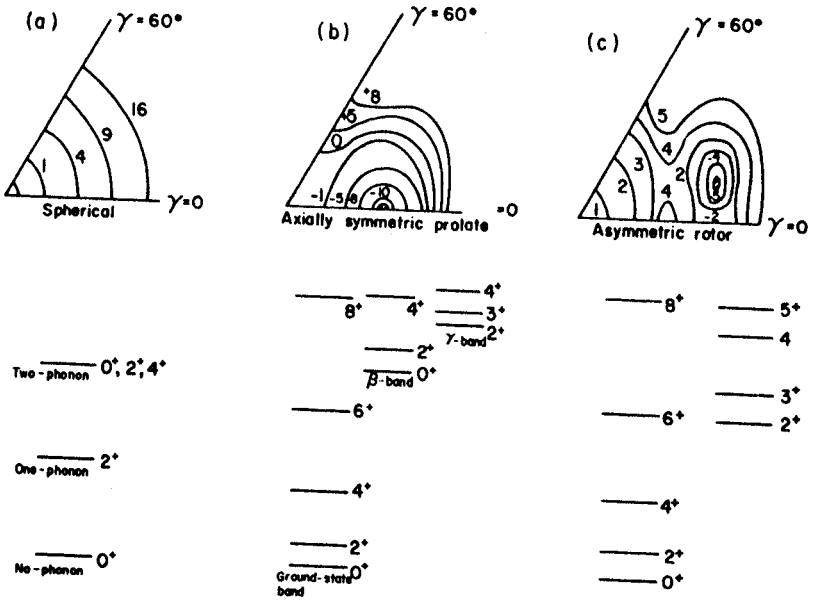

Figure II-2. Schematic Plots of $V(\beta,\gamma)$ for (a) Spherical, (b) Axially Symmetric Prolate, and (c) Asymmetric Shapes. Also shown are typical energy level spectra associated with these potentials. Taken from Reference [Pr 75].

about the equilibrium value of β and γ, the Hamiltonian simplifies to

$$H = \frac{1}{2} \sum_{k=1}^{3} I_k \omega_k^2 = \sum_{k=1}^{3} \frac{L_k^2}{2I_k} \quad . \tag{II-14}$$

For an axially symmetric nucleus, the moment of inertia about the symmetry axis is zero as no rotations about this axis are observable. From (II-11) one sees that the two remaining I_k values are equal in this case. This leads to the simple energy expression

$$E_J = \frac{\hbar^2}{2I} J(J + 1) \quad , \tag{II-15}$$

with the total angular momentum J = 0, 2, 4... for the ground band. An example of this band structure is shown in Figure II-2. If small vibrations are allowed about $V(\beta_o, \gamma_o \simeq 0)$ two additional low-lying bands may be seen in a strongly deformed nucleus. These are called β and γ vibrations. The β vibration causes a distortion from the equilibrium value of β_o while preserving axial symmetry ($\gamma = 0$, for a prolate example). The γ vibrational mode involves oscillations about $\gamma = 0$ with β fixed. This type of oscillation disrupts the axial symmetry. These vibrational states will usually have a rotational band built on them which have the same J(J + 1) spacing (see Figure II-2). The quantum number K, the projection of J onto the symmetry axis, is often used to describe these bands. The β vibrations preserve axial symmetry so K = 0, while the γ vibrations have

K = 2 since they represent motion out of the symmetry plane. It is possible to have a two γ-phonon vibration, much like the simple 2-phonon states described in Section II-A. This would result in a K = 0 and K = 4 bandhead, but these would be expected at approximately twice the single γ-phonon energy. This type of state will be discussed further in Chapter V.

D. The Asymmetric Rotor Model

The asymmetric rotor model of Davydov and Fillippov [Da 58] is actually not too different from the basic framework of the simple rotor except that the zero-point value of γ is allowed to be non-zero. This allows for rotation about all three axes and thus three different K_k values. Cast in its simplest form, this model has a potential $V(\beta,\gamma)$ with a steep minimum about a fixed β and some $\gamma \neq 0$. If this condition is relaxed, similar β and γ vibrations will be predicted at lower excitation energies, much like the symmetric rotor case of Section II-B.

The Hamiltonian is identical to Equation (II-14) except that each I_k is allowed to be non-zero. The solution of the Hamiltonian is somewhat more involved in this case, however, since the quantum number K, the projection of J onto the symmetry axis, is no longer a good quantum number because the non-zero γ-value destroys the axial symmetry. The eigenfunctions are thus mixed in terms of K and can be expressed as

$$|\psi_{JM}> = \sum_{K \leq J} g^{J}_{k_i}(\gamma)\,|JMK> \ , \qquad \text{(II-16)}$$

where the mixing coefficients $g^{J}_{k_i}$ will be derived from Equation (II-17) and the $|JMK>$ are the eigenfunctions of an axially symmetric rotor [Pr 75]. Solving the Hamiltonian in the $|JMK>$ basis shows that only one 0^+ state, two 2^+ states, one 3^+ state, three 4^+ states, etc. are formed. This is due to the allowed values of J and K as a result of symmetry considerations

$$K = 0,\ 2,\ 4\ldots$$
$$J = \begin{cases} K,\ K+1,\ K+2\ldots & \text{if } K \neq 0 \\ 0,\ 2,\ 4\ldots & \text{if } K = 0\ . \end{cases} \qquad \text{(II-17)}$$

Solutions for the energies of these states are obtained by solving the following equation for each value of K

$$<JMK|\sum_{k=1}^{3} \frac{L_k^2}{2I_k} - E|\psi_{JM}> = 0\ . \qquad \text{(II-18)}$$

Figure II-2 shows a typical energy level pattern and $V(\beta,\gamma)$ surface for an asymmetric rotor. The level spacing is quite similar to the simple $J(J+1)$ rule of a symmetric rotor. In fact, if one "softens" the asymmetric rotor to permit β-vibrations following Davydov and Chaban [Da 60] there are actually very few differences between the electromagnetic properties and the energy levels predicted from this model or from an axially symmetric model with the rotation-vibration coupling terms included [Fa 65]. Yamazaki has shown [Ya 63] there are really no discernable differences in the two models

unless one studies the higher-lying bands, in particular the K = 4, two γ-phonon band. Thus, distinguishing between the two models on the basis of data related to the ground band and lowest K = 2 band is quite difficult.

E. The Interacting Boson Approximation (IBA) Model

1. Introduction

All the models previously mentioned in this chapter and in the introduction have a common framework in the hydrodynamical model of Bohr and Mottelson. The only differences between the models lie in the assumptions made in deriving certain parameters or in those assumptions which simplify the Hamiltonian. In this section an entirely different approach to the modeling of the nucleus will be described. Arima and Iachello [Ar 76] have proposed a group-theoretical approach to explain the collective properties of nuclei with $A \geq 100$ except those near closed shells. The cutoff of the model at $A \geq 100$ is due to the proximity of the shell closures in lighter nuclides and the small number of particles outside the core available for this type of collective interpretation. This discussion will be confined to even-even nuclei, although the model is capable of describing odd-A nuclei as well [Ar 76a].

In this model pairs of particles (protons or neutrons) are treated as bosons, which can occupy two levels, a ground state, associated with s bosons, and one excited state

occupied by d bosons. All possible interactions are allowed between the two types of bosons. The energy and angular momentum of s bosons is ε_s and L = 0, and for the d bosons, ε_d and L = 2. The total number of bosons for a particular nucleus, $N = n_s + n_d$, is a fixed parameter. N is determined from the number of neutron and proton pairs (or holes) outside their respective closed shells. For the nuclides $^{192-198}_{78}Pt_{114-120}$ the nearest shell closures are 126 for neutrons and 82 for protons. Thus, the number of neutron pairs ranges from 6 to 3 while there are 2 proton pairs, (82–78)/2 = 2. This gives values of N for $^{192,194,196,198}Pt$ of 8, 7, 6, and 5 respectively. The following derivation of the many IBA expressions follows very closely the formalism of Reference [Ar 76].

The simplest Hamiltonian for the IBA which contains only one- and two-body terms is

$$H = \varepsilon_s s^\dagger s + \varepsilon_d \sum_m d_m^\dagger d_m + \sum_{i<j}^{N} V_{ij} \,, \qquad \text{(II-19)}$$

where $s^\dagger$(s) is the creation (annihilation) operator for s bosons, $d^\dagger$(d) is the creation (annihilation) operator for d bosons, and V is the interaction between the bosons. The sum is taken over the (2L + 1) spin projections of the d bosons which gives 5 terms. Group theory is introduced by allowing the six components of the s and d bosons to provide a basis for the representation of the SU(6) group. Then the Hamiltonian can be written in a more general second quantized

form where only symmetric representations are allowed. These terms are comprised of generators of the SU(6) group, which are $(s^{\dagger}s)^{(0)}$, $(d^{\dagger}d)^{(L)}$, $(d^{\dagger}s)^{2}$... totaling 36 generators.

Equation (II-19) can now be written as

$$H = \varepsilon_s s^{\dagger}s + \varepsilon_d \sum_m d^{\dagger}_m d_m + \sum_{L=0,2,4} \frac{1}{2}(2L+1)^{1/2}$$

$$\times C_L[(d^{\dagger}d^{\dagger})^{(L)}(dd)^{(L)}]^{(0)} \qquad \text{(II-20)}$$

$$+ \frac{1}{2} V_2[(d^{\dagger}d^{\dagger})^{(2)} \cdot (ds)^{(2)} + (s^{\dagger}d^{\dagger})^{(2)} \cdot (dd)^{(2)}]^{(0)}$$

$$+ \frac{1}{2} V_o[(d^{\dagger}d^{\dagger})^{(0)} \cdot (ss)^{(0)} + (s^{\dagger}s^{\dagger})^{(0)} \cdot (dd)^{(0)}]^{(0)}$$

$$+ U_2[(d^{\dagger}d^{\dagger})^{(2)} \cdot (ds)^{(2)}]^{(0)} + \frac{1}{2} U_o[(s^{\dagger}s^{\dagger})^{(0)} \cdot (ss)^{(0)}]^{(0)}$$

where the parentheses denote angular momentum couplings and the C_L, V_L, U_L represent the two-body matrix elements

$$C_L = \langle d^2 L|V|d^2 L\rangle$$

$$V_2 = \langle ds2|V|d^2 2\rangle\sqrt{5/2}$$

$$V_o = \langle d^2 0|V|s^2 0\rangle \frac{\sqrt{2}}{2} \qquad \text{(II-21)}$$

$$U_2 = \langle ds2|V|ds2\rangle \sqrt{5}$$

$$U_o = \langle s^2 0|V|s^2 0\rangle$$

The complex Hamiltonian of Equation (II-20) actually only has 4 types of terms. The first two terms are just s and d boson counting terms. Terms with the coefficients C_L and

U_L do not change the number of s or d bosons, n_s and n_d. The third type of term has the coefficient V_2 and changes n_d by one unit, while the fourth type, with V_o as its coefficient, changes n_d by two units. The dominance of one or more of these terms allows for the simplification of the IBA Hamiltonian and in three special situations will even allow analytical solutions to be obtained. These three limits are denoted by the group designations SU(5), SU(3), and O(6), and are attained by requiring the Hamiltonian to contain terms that are generators of each subgroup. In the case of the SU(5) limit, the Hamiltonian would contain only terms that conserve n_d. For the SU(3) limit, both one and two d-boson number changing terms are included, while only the two d boson changing terms are allowed in the O(6) system.

The basis states for the IBA Hamiltonian can be written as

$$|\psi\rangle = |Nn_d n_\beta n_\Delta JM\rangle = \frac{1}{A} \sum_{k=0}^{N} C_k d^{\dagger k} s^{\dagger N-k} |0\rangle \ , \qquad \text{(II-22)}$$

where $|0\rangle$ represents the closed shell, and A is a normalization constant. The $d^\dagger$ operators are coupled to some definite angular momentum J,M. Here n_d, n_β, and n_Δ are the number of d bosons, number of pairs of d bosons coupled to spin zero, and the number of zero-coupled triplets of d bosons respectively.

The full SU(6) Hamiltonian of Equation (II-20) can also be written in terms of the specific boson-boson interactions

$$H = \varepsilon \sum_m d_m^\dagger d_m - k \sum_{ij} \vec{Q}_i \cdot \vec{Q}_j - k' \sum_{i<j} L_{ij} + k'' \sum_{i<j} P_{ij} \,, \tag{II-23}$$

where $\varepsilon = \varepsilon_d - \varepsilon_s$ (ε_s is usually set equal to zero), $\vec{Q}_i$ is the quadrupole moment of the i^{th} boson, $L_{ij} = 2\vec{\ell}_i \cdot \vec{\ell}_j$ with $\vec{\ell}_i$, $\vec{\ell}_j$ being the angular momentum of the i^{th} and j^{th} boson, P_{ij} is the pairing operator between bosons, and k, k', k" are constants determining the strengths of each interaction. This form of the Hamiltonian is considerably more convenient to use when one is studying nuclei that lie between the three analytical limits as will be seen later. It should be noted that the spin dependent part of Equation (II–23) contains only $\Delta n_d = 0$ terms, the pairing interaction only $\Delta n_d = \pm 2$ terms, and the Q·Q interaction only $\Delta n_d = \pm 1,2$ terms.

The relationship between the coefficients of Equations (II–23) and (II–20) can be found in the computer code PHINT [Se 77], and are shown in Table II–1. The program PHINT is a general program written to diagonalize the IBA Hamiltonian whether expressed in terms of Equation (II–20) or (II–23), or as a mixture of both. With this program several properties [Sc 78] of most nuclei with $A \geq 100$ can be solved numerically with relatively small matrices, typically of order N.

One of the most useful aspects of the IBA model is its simplicity for several regions of nuclei. When certain terms dominate in the Hamiltonian, simplifications can be made

Table II-1. The Relationship Between the Coefficients of Equation (II–20) and (II–23).

Equation (II-20)		Equation (II-23)[a]				
	=	κ	+	κ'	+	κ''
ε^{b}		$9/2\,\kappa$		$-6\kappa'$		0
C_0		-7κ		$12\kappa'$		$5\kappa''$
C_2		$3/2\,\kappa$		$6\kappa'$		0
C_4		-2κ		$-8\kappa'$		0
V_0		$-(20)^{1/2}\kappa$		0		$-(5/4)^{1/2}\kappa''$
V_2		$2(35)^{1/2}\kappa$		0		0
U_0		0		0		κ''
U_2		-4κ		0		0

[a] These factors have been obtained from the IBA program PHINT [Sc 77].

[b] The values for Equation (II–23) are additional contributions to ε not explicitly included in the first term of Equation (II–23).

which greatly reduce the problem. Arima and Iachello [Ar 76, Ia 78] have shown that in three cases these simplifications lead to a Hamiltonian which contains the generators of a particular subgroup of SU(6). Then, by exploiting the symmetry properties of each group, an analytical solution can be obtained. The three subgroups, SU(5), SU(3), and O(6), have been used to solve for closed expressions for the energy levels and transition probabilities. The following sections will provide a more detailed discussion of each of these limiting cases, particularly the O(6) limit which seems applicable in the Pt region.

2. The SU(5) Limit - Vibrational Nuclei

When the energy gap $\epsilon = \epsilon_d - \epsilon_s$ is much larger than the value for the various 2-body matrix elements shown in Equation (II-21), the Hamiltonian reduces to a simple d boson counting term, $\epsilon \sum_m d_m^\dagger d_m$ with eigenvalues

$$E(N, n_d, n_\beta, n_\Delta, L, M) = \epsilon n_d \ , \qquad \text{(II-24)}$$

where $n_d = 1, 2, 3 \ldots N$. This gives the same energy spectrum as the Bohr-Mottelson Hamiltonian of Equation (II-4). A typical spectrum is shown in Figure II-3, which is characterized by a constant level spacing and multiple degeneracies for a given n_d. If the $\Delta n_d = 0$ terms of the IBA Hamiltonian are small but non-zero, $C_L \neq 0$, the full SU(5) "invariant" Hamiltonian can be expressed as

Figure II-3. Energy Levels in the IBA With No Boson Interactions. This spectrum is identical to that for a harmonic vibrator. The energies are calculated from Equation (II–25).

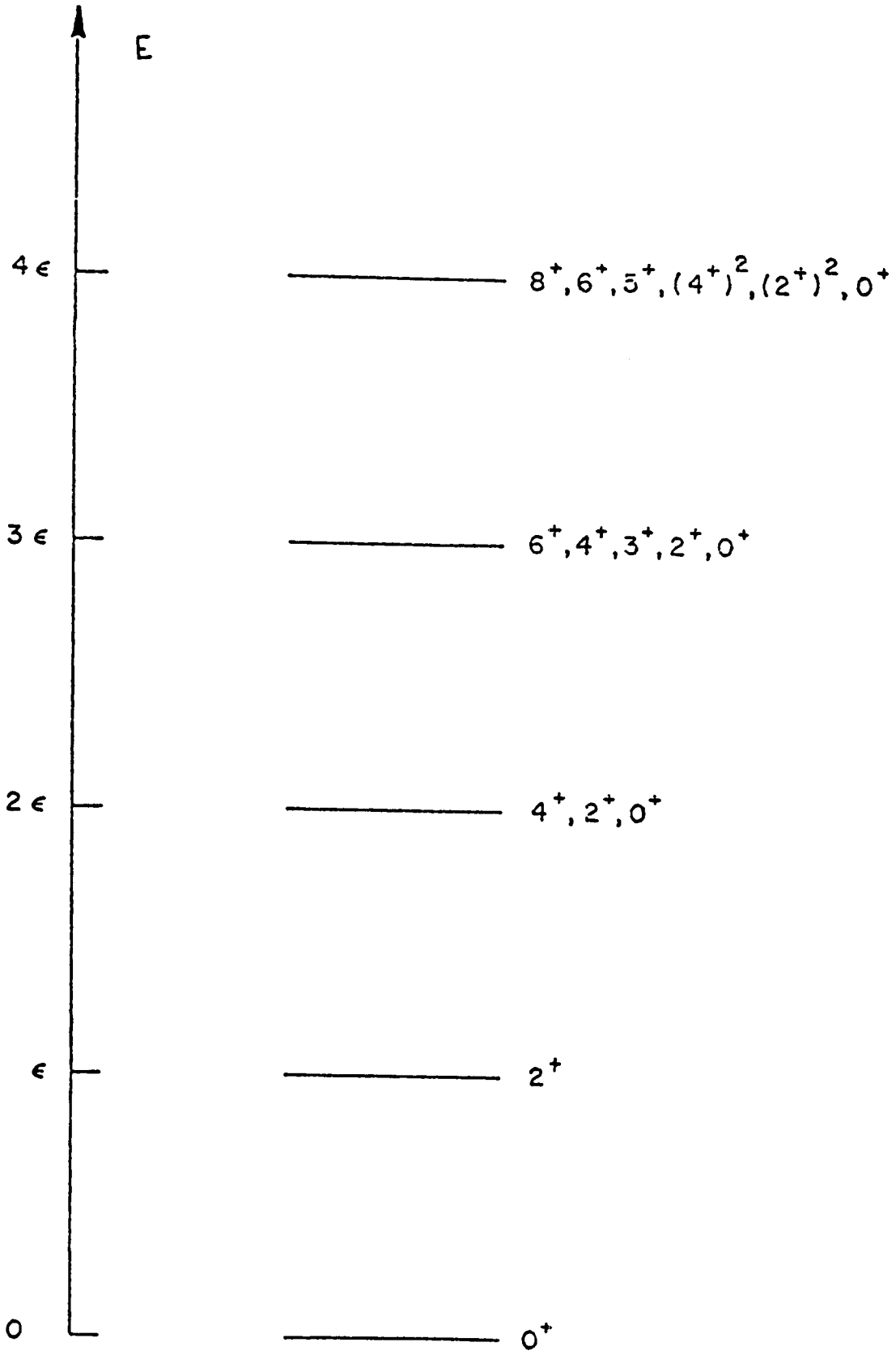

Figure II-3.

$$H = \varepsilon \sum_m d_m^\dagger d_m + \frac{1}{2} \sum_L (2L + 1)^{1/2} C_L [(d^\dagger d^\dagger)^{(L)} \ (dd)^{(L)}]^{(0)} . \tag{II-25}$$

A closed solution is still possible [Ar 76] with this added term. Rewriting the second term of Equation (II-25) in terms of the actual boson-boson forces (see Equation (II-23)), the result is

$$V = \sum_{i<j} V_{ij} = \sum_{i<j} (\alpha l_{ij} + \beta P_{ij} + \gamma L_{ij}) , \tag{II-26}$$

where l_{ij} is the unit operator and, as before, P_{ij} and L_{ij} are the pairing and $\vec{\ell}\cdot\vec{\ell}$ operators. The coefficients α, β, and γ are the new parameters in this limit replacing the C_L's. Table II-2 shows the relationship between these equivalent sets of parameters. The expectation values for these operators are

$$\begin{aligned} \langle l \rangle &= \frac{1}{2} n_d (n_d - 1) \\ \langle L \rangle &= L(L + 1) - 6n_d \\ \langle P \rangle &= (n_d - v)(n_d + v + 3) , \end{aligned} \tag{II-27}$$

where v is the seniority number for the bosons, $v = n_d - 2n_\beta$. This gives an eigenvalue expression for the complete SU(5) limit:

$$\begin{aligned} E(N, n_d, v, n_\Delta, L, M) = {} & \varepsilon n_d + \alpha \frac{1}{2} n_d (n_d - 1) \\ & + \beta (n_d - v)(n_d + v + 3) \\ & + \gamma [L(L + 1) - 6n_d] . \end{aligned} \tag{II-28}$$

Table II-2. The Relationship Between the Coefficients of Equation (II–26) and the C_L Coefficients of Equation (II–25). The factors for Equation (II–26) were obtained from [Ar 76].

Equation (II–26)	Equation (II–25)		
	C_0	C_2	C_4
α	---	$4/7\ C_2$	$3/7\ C_4$
β	$1/10\ C_0$	$-1/7\ C_2$	$3/70\ C_4$
γ	---	$-1/14\ C_2$	$1/14\ C_4$

These extra terms in the energy expression now lift the degeneracies shown in Figure II–3 and produce a spectrum similar to the one shown in Figure II–2 for the hydrodynamic vibrator. Figure II–4 shows how the energy levels can now be arranged into bands with the maximum spin determined by N. All three limits of the IBA display this "cutoff" aspect, evident in both the energy and decay properties. This results from the finite dimensionality built into the IBA, in contrast to the geometric models which have $N \to \infty$ for the liquid drop. The effect of finite dimensionality is most evident in the branching ratios within the "ground band" as shown for the SU(5) limit in Figure II–5. In all cases of a simple vibrator, the IBA predicts a ratio less than the geometrical predictions. This is in agreement with current experimental measurements.

As mentioned earlier, one of many properties which can be calculated within the IBA is the electromagnetic decay of a nucleus. The most general form of the IBA transition operator is given by

$$T_m^{(\ell)} = \alpha_\ell \, \delta_{\ell 2} (d^\dagger s + s^\dagger d)_m^{(2)} + \beta_\ell (d^\dagger d)_m^{(\ell)} + \gamma_{\ell 0} \delta_{\ell 0} \delta_{m 0} (s^\dagger s)_0^{(0)} \,, \qquad \text{(II-29)}$$

where ℓ is the multipolarity of the transition with projection m, and α, β, γ are the coefficients of the various terms. The exact form of the coefficients will depend on the

Figure II-4. Sample Energy Level Spectrum Calculated With the SU(5) Limit of the IBA With Interboson Forces. The states are labeled by the quantum numbers J^{π} (n_d, V, n_{Δ}). The energies are calculated from Equation (II-29). Taken from Reference [Ar 76].

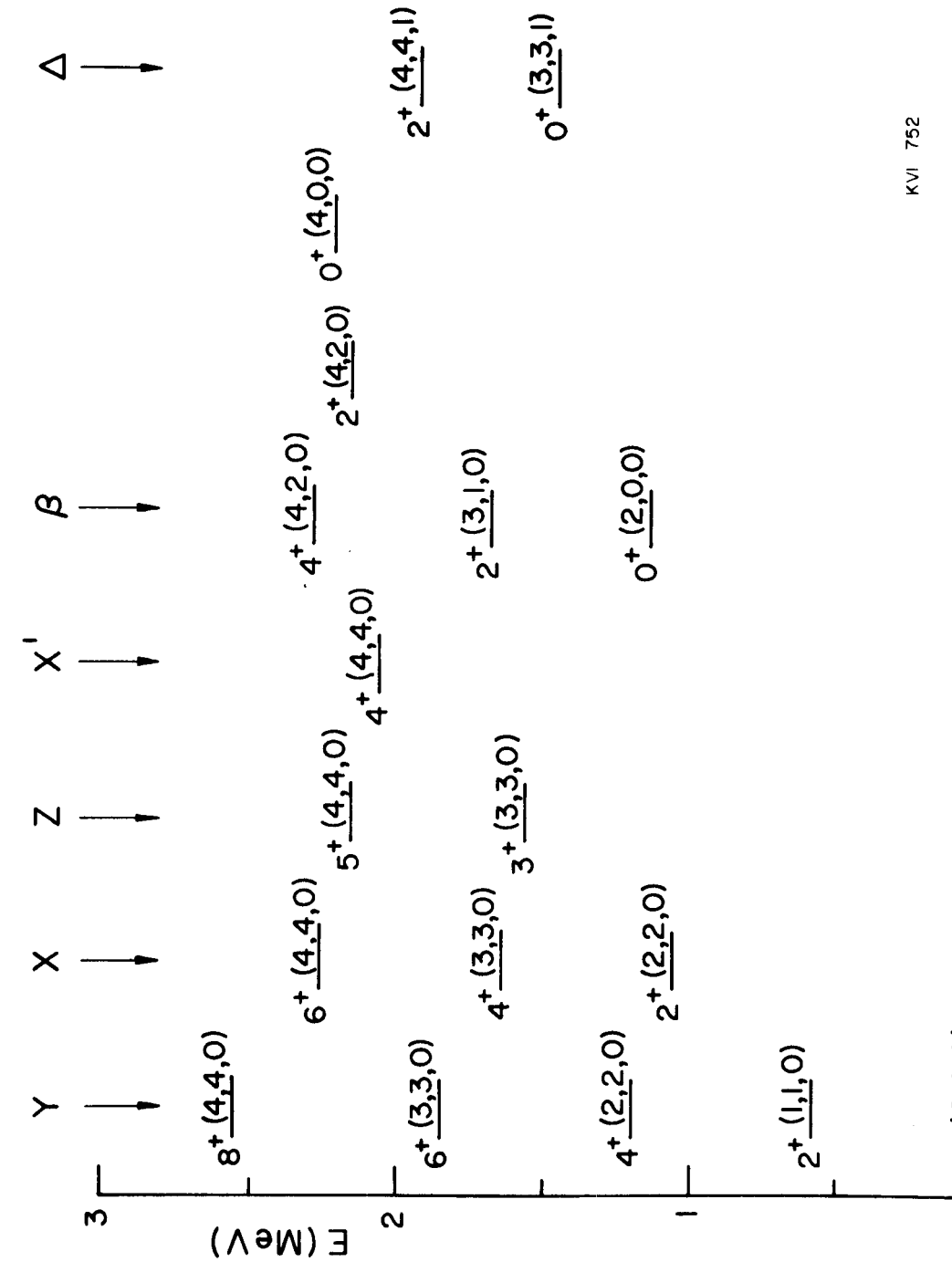
E (MeV)
3
2
1
0
Y
X
Z
X'
β
Δ
8+ (4,4,0)
6+ (4,4,0)
6+ (3,3,0)
5+ (4,4,0)
4+ (4,4,0)
4+ (4,3,0)
4+ (4,2,0)
3+ (3,3,0)
2+ (4,2,0)
2+ (4,4,1)
2+ (3,1,0)
2+ (2,2,0)
0+ (4,0,0)
0+ (3,3,1)
0+ (2,0,0)
4+ (2,2,0)
2+ (1,1,0)
0+ (0,0,0)
KVI 752

Figure II-4.

Figure II-5. The Effect of Finite Dimensionality on Relative B(E2) Values in the Ground Band of an SU(5) Nucleus. These values are plotted as a function of L' and n_d for an N = 6 and N = 12 nucleus. Taken from Reference [Ar 76].

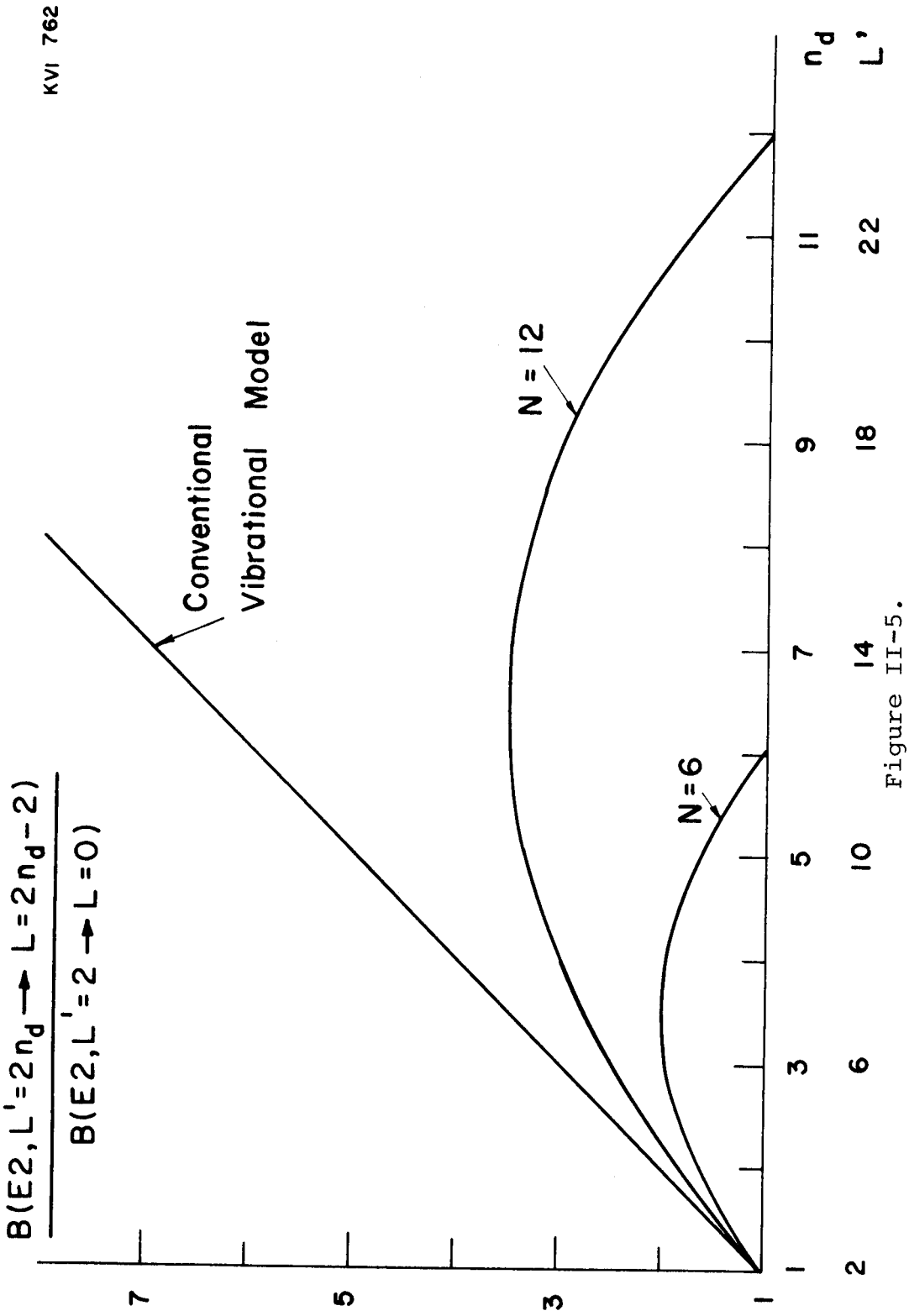
KVI 762
B(E2, L'=2n_d → L=2n_d-2) / B(E2, L'=2 → L=0)
Conventional
Vibrational Model
N = 12
N=6
7
5
3
1
2
6
10
14
18
22
n_d
L'

Figure II-5.

specific limit of the model, SU(3), O(6), and SU(5). The form of this operator must also be a generator of the particular subgroup, which simplifies Equation (II–29) and allows for an analytical solution. For E2 transitions in the SU(5) limit Equation (II–29) reduces to

$$T_m^{(E2)} = \alpha(d^\dagger s + s^\dagger d)_m^{(2)} \quad , \qquad \text{(II-30)}$$

where

$$\alpha = \langle d||\vec{Q}||s\rangle \frac{\sqrt{5}}{5} \quad ,$$

$\vec{Q}$ being the quadrupole operator. This operator leads to a selection rule of $\Delta n_d = \pm 1$, the same as in its geometrical counterpart. The trends of several branching ratios are given in References [Ar 76, Ar 78, Sc 78].

3. The SU(3) Limit - Rotational Nuclei

In situations where the Q·Q and L terms of Equation (II–23) dominate, the boson energy, ε, and the pairing force, P_{ij}, analytical solutions can be obtained from the simplified Hamiltonian by using the symmetry properties of the SU(3) group. Many of the results are similar to a special type of symmetric rotor.

A new set of basis states is used to solve the SU(3) eigenvalue equations

$$H|N,(\lambda,\mu)KLM\rangle = E|N,(\lambda,\mu)KLM\rangle \qquad \text{(II-31)}$$

and

$$H = -k \sum_{ij} \vec{Q}_i \cdot \vec{Q}_j - k' \sum_{ij} L_{ij} \quad , \qquad \text{(II-32)}$$

where (λ,μ) are quantum numbers that label the representations of SU(3), L, and M are the angular momentum and its Z-axis projection while K distinguishes states with identical (λ,μ), L. The solution of (II-31) is given by

$$E(N,(\lambda,\mu)KLM) = \alpha L(L+1) - \beta C(\lambda,\mu) \qquad \text{(II-33)}$$

Here $\alpha = \frac{3}{4}\kappa - \kappa'$, $\beta = \kappa$, and $C(\lambda,\mu)$ is the quadratic Casimir operator [Ar 78] of SU(3)

$$C(\lambda,\mu) = \lambda^2 + \mu^2 + \lambda\mu + 3(\lambda+\mu) \ . \qquad \text{(II-34)}$$

The (λ,μ) can assume values of $(2N,0)$, $(2N-4,2)$, $(2N-8,4)$ ...etc. Figure II-6 shows a typical energy spectrum obtained within the SU(3) limit with $\kappa' = 0$. Note that the level spacing is proportional to $L(L+1)$ and that a $K = 0$ "β-band" and $K = 2$ "γ-band" arise quite naturally from this limit along with higher lying bands of a $2\text{-}\beta$ or $2\text{-}\gamma$ nature. One notable exception in these bands compared to those of the symmetric rotor is that states of the same spin, L, belonging to the same (λ,μ) representation, are degenerate in the strict SU(3) limit.

The E2 operator in the SU(3) limit is given by

$$T^{(E2)}_m = \alpha_2[(d^\dagger s + s^\dagger d)^{(2)}_m - \frac{\sqrt{7}}{2}(d^\dagger d)^{(2)}_m] \ , \qquad \text{(II-35)}$$

where α_2 is the effective E2 charge and β_2 in (II-29) is now $-\frac{\sqrt{7}}{2}\alpha_2$. This expression predicts very strong transitions within a band but in the strict limit transitions are not

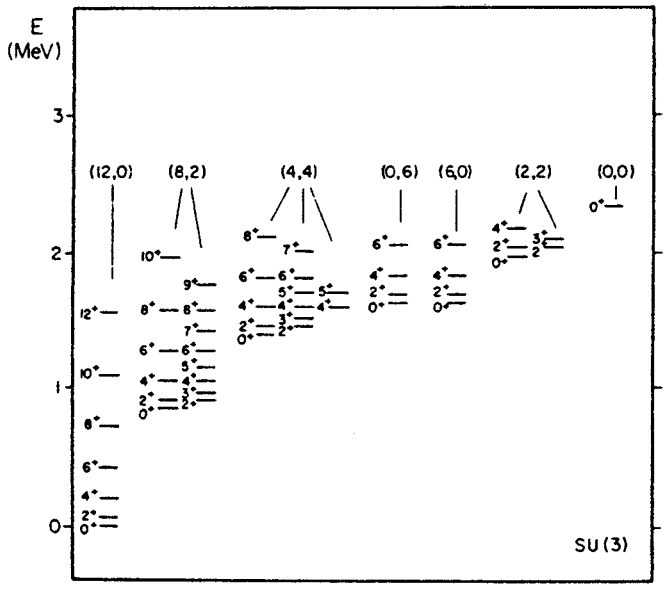

Figure II-6. Sample Energy Level Spectrum Calculated With the SU(3) Limit of the IBA. The states are separated into bands denoted by the quantum numbers (λ,μ) and further identified by K and J^{π}. The energies are calculated from Equation (II-34). Taken from Reference [Ia 78].

allowed between states with a different (λ,μ). Thus intraband transitions are allowed for the β- and γ-bands, but no transitions are predicted from either of these bands $(\lambda,\mu) = (2N - 4,2)$ to the ground band $(\lambda,\mu) = (2N,0)$. This is contrary to the predictions of the geometrical symmetric rotor model. Examples of other decay systematics are given in Reference [Ar 78]. Closed form expressions can also be obtained for certain types of transitions. Of particular interest is the expression for transitions within the ground band. For the SU(3) limit [Ar 78]

$$B_{IBA}(E2;\ L + 2 \rightarrow L) = \alpha_2^2 \frac{3}{4} \frac{(L + 2)(L + 1)}{(2L + 3)(2L + 5)} \times (2N - L)(2N + L + 3) \qquad \text{(II-36)}$$

for the E2 decays, and

$$Q_J = -\alpha_2 \left(\frac{16\pi}{40}\right)^{1/2} \frac{L}{2L + 3} (4N + 3) \qquad \text{(II-37)}$$

for the static moments. If these expressions are compared with those of the geometrical model [Bo 69] one obtains

$$\frac{B(E2;\ L + 2 \rightarrow L)}{B_{BM}(E2;\ L+ 2 \rightarrow L)} = \frac{(2N - L)(2N + L + 3)}{(2N + \frac{3}{2})^2} \cdot \qquad \text{(II-38)}$$

This ratio illustrates the finite dimensionality present in the IBA model. As $N \rightarrow \infty$, $B_{IBA} \rightarrow B_{BM}$. However, the "correction factor" differs from unity for finite N values and approaches zero as $L \rightarrow 2N$. This implies that the IBA model predicts decreasing values for the transition probabilities between states with higher L values compared to a

single value predicted by the geometrical model. This cutoff effect has been seen in ^{20}Ne decay [Ar 78].

4. The O(6) Limit - Transitional Nuclei

For this third limit of the IBA, the dominant interboson force is the pairing interaction. The analytical solution to the IBA Hamiltonian is achieved by requiring the terms of the Hamiltonian to be generators of the subgroup O(6). This produces a Hamiltonian of the form

$$H = \varepsilon \sum_m d_m^\dagger d_m + \sum_L \frac{1}{2} (2L+1)^{1/2} C_L [(d^\dagger d)^{(L)} (dd)^{(L)}]^{(0)}$$

$$+ \frac{1}{2} V_o [(d^\dagger d)^{(0)} (ss)^{(0)} + (s^\dagger s^\dagger)^{(0)} (dd)^{(0)}]^{(0)} \qquad \text{(II-39)}$$

$$+ \frac{1}{2} U_o [(s^\dagger s^\dagger)^{(0)} (ss)^{(0)}]^{(0)} \; .$$

Recall that the V_o (pairing) term results in a change in the number of d bosons by ± 2. This causes considerable mixing of the wave functions if the basis set shown in (II–22) is used. If the basis denoted as $|NJ\sigma\tau\nu_\Delta LM\rangle$ is used, the Hamiltonian can be expressed in terms of operators which are diagonal in this new basis. New quantum numbers are then obtained: 1) σ characterizes the totally symmetric irreducible representations of O(6), with σ = N, N − 2...0 or 1 for N even or odd; 2) τ characterizes the totally symmetric irreducible representations of O(5), where $\tau = \sigma, \sigma - 1 \ldots 0$; 3) ν_Δ is the number of zero-coupled boson triplets, with the relationship $\tau = 3\nu_\Delta + \lambda$, $\nu_\Delta = 0,1\ldots$, where L is allowed to

be $L = 2\lambda, \quad 2\lambda - 2, \ldots \lambda + 1, \lambda$. The Hamiltonian is conveniently expressed as

$$H = AP_6 + BC_5 + CC_3 \ , \qquad \text{(II-40)}$$

where P_6 is the pairing operator and C_5 and C_3 are the Casimir operators of O(5) and O(3) respectively. The presence of operators for several subgroups in this expression results from the group reduction

$$SU(6) \supset O(6) \supset O(5) \supset O(3) \ .$$

Table II–3 shows the correspondence between the new coefficients in (II–40), A, B, and C with the C_L, V_L, and U_L coefficients of (II–20,31). The eigenvalues resulting from (II–40) are [Ar 78a]

$$E(N, \sigma, \tau, \nu_\Delta LM) = \frac{A}{4}(N - \sigma)(N + \sigma + 4)$$

$$+ \frac{B}{6}\tau(\tau + 3) + C[L(L + 1)] \ . \qquad \text{(II-41)}$$

Figure II–7 displays a typical energy level spectrum for the O(6) limit with N = 6 and A, B, C > 0. The signs of the three terms can considerably alter the level pattern. In particular, a positive value for C drops the 2_2^+ state below the 4_1^+, a feature of the Pt nuclides. The grouping of energy levels in Figure II–7 is similar to those in Figure II–4 for the SU(5) limit with a few exceptions. The most notable of these are the "missing" 0^+ and 2^+ levels in the $\tau = 2$ and $\tau = 3$ groupings in $O(6)(\sigma = \sigma_{max})$ which correspond to the

Table II-3. The Relationships Between the Coefficients of Equation (II–40), (O(6) Limit) and Those of Equations (II–20, 39) (Full IBA Hamiltonian).

Equation (II–20)	Equation (II–40) O(6) Limit[a]		
Full IBA	A	B	C
ε	0	4B	6C
C_0	5/2 A	-8B	-12C
C_2	0	2B	-6C
C_4	0	2B	8C
V_0	$-(5/16)^{1/2}$A	0	0
V_2	0	0	0
U_0	1/2 A	0	0
U_2	0	0	0

[a]Values from [Ca 78a].

Figure II-7. Sample Energy Level Spectrum Calculated With the O(6) Limit of the IBA. The states are denoted by the quantum numbers (σ, τ, ν_Δ, J). The energies are given by Equation (II-42). Taken from Reference [Ar 78a].

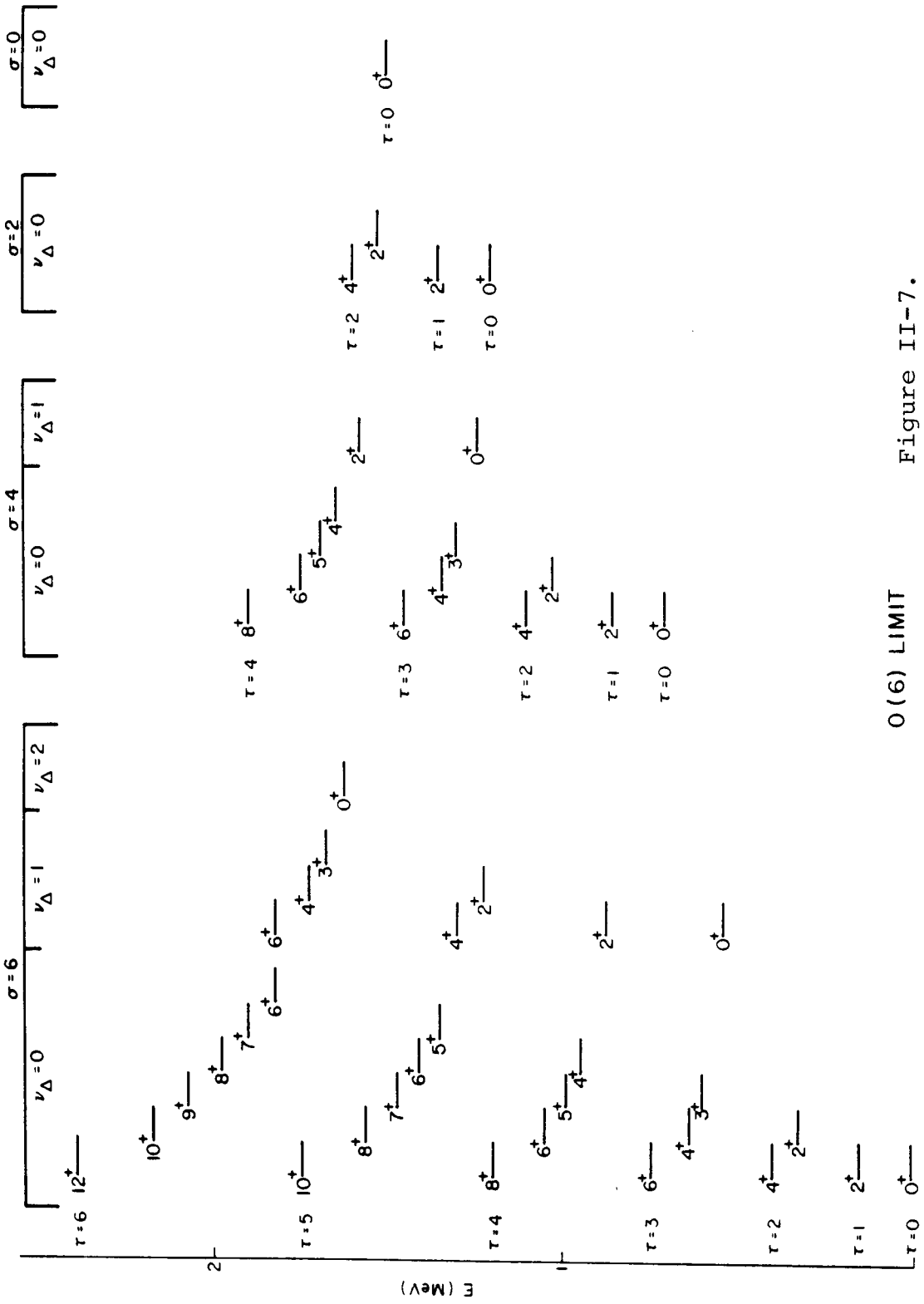

Figure II-7.

$n_d = 2$ and $n_d = 3$ states in SU(5). These states in the SU(5) limit effectively have been pushed higher in energy than their n_d neighbors due to their $n_\beta = 1$ character, while the other states in each group have $n_\beta = 0$. This should be expected since n_β is the number of boson pairs coupled to zero, and the difference between the SU(5) and O(6) limits is the introduction of a pairing interaction. An additional feature of this limit is the set of $0 - 2^+ - 2^+$ groupings with strong E2 cascades, and level spacings proportional to $\tau(\tau + 1)$.

Several closed expressions for E2 transition rates have been obtained, again by using a transition operator which is a generator of the limiting symmetry, in this case O(6). The operator satisfying this condition is

$$T_m^{(E2)} = \alpha_2 (d^\dagger s + s^\dagger d)^{(2)} , \qquad \text{(II-42)}$$

where α_2 is a strength factor. This operator requires selection rules of $\Delta\sigma = 0$ and $\Delta\tau = \pm 1$. The σ selection rule is a direct result of the operator being a generator of the O(6) group and thus cannot connect states with different representations. This is analogous to the $\Delta(\lambda,\mu) = 0$ selection rule for the SU(3) limit. The $\Delta\tau$ restrictions arise from the fact that the operator can create or destroy one d boson. Several examples of these closed expressions are given in Reference [Ar 78a]. Two informative branching ratios are

such that as ϵ increases from the heavy to light samariums, the boson energy term overshadows the Q·Q terms, thus providing a transition from the SU(3) to the SU(5) limit. This perturbation causes the wave functions to mix so that most of the transition rate selection rules are broken. Casten and Cizewski [Ca 78] have carried out a similar procedure to describe the O(6) → rotor transition for the Pt–Os region. This is accomplished by introducing a logarithmically increasing (with N) quadrupole-quadrupole boson interaction, while varying the O(6) parameters, A, B, and C, to account for the changes in mass. Because the Q·Q force is comprised of a one d boson operator, all wave functions become mixed and both the σ and τ selection rules are broken.

This study of the Pt nuclides with the (p,t) and (p,p') reactions has for the most part used wave functions similar to those of Casten and Cizewski [Ca 78], derived from the slightly perturbed O(6) limit. The intention of this study as well as [Ca 78] was not to find a set of "best fit" parameters for the O(6) limit, but rather to use a consistent set of parameters to adequately describe the Pt region. Another reason for not fine tuning the parameters is the absence of any explicit proton-neutron interaction between bosons [Ar 77]. Recall that when determining N, the total number of bosons in a system, the particular type of boson, p or n, was not a factor, only the sum of each type. The role

of this proton-neutron boson interaction appears to be most critical near the end of a shell – the region where the O(6) limit should be most effective [Ar 78a]. Preliminary results indicate that the energy predictions will improve, while the branching ratios remain unchanged [Ci 78].

CHAPTER III

THEORETICAL BACKGROUND - NUCLEAR REACTIONS

A. The Distorted-Wave Born Approximation (DWBA) for Transfer Reactions

1. Introduction

Current methods used to calculate cross sections for direct nuclear transfer reactions fall into three major categories, the DWBA, coupled channels Born approximation (CCBA), and the multi-step sequential transfer approximation. Although each method has a somewhat different domain of applicability, the DWBA is by far the least elaborate of the three methods and actually provides the basic framework for the latter two. The CCBA is usually used to describe reactions which involve very collective type nuclei, such as the rare earths. In these cases the levels in the rotational bands are so coupled that a one-step (one channel) analysis, like DWBA, cannot reproduce the data. The sequential transfer approximation is primarily used in multi-nucleon transfers, where several intermediate steps in the transfer process may be necessary to interpret the results. The degree of computational difficulty increases very dramatically from DWBA to the sequential transfer approximation

for even the simplest one-nucleon transfer reactions. For a two-nuclear transfer reaction, such as (p,t), these computational problems are magnified. For this reason, and the lack of collectivity in the Pt region, the theoretical interpretation of the (p,t) reactions was limited to the DWBA method.

The theory of direct two-nucleon transfer reactions has been developed by several authors [To 61, Gl 62, Sa 64 Au 70] utilizing plane-wave (PWBA) and distorted-wave Born approximations (DWBA). The basic idea underlying these studies is a one step mechanism involving an interaction between the projectile and the transferred nucleons. The transfer process itself is assumed to be weak so that it can be treated in a first order Born approximation. The following derivation is presented as an outline of the general DWBA theory primarily to show the basic assumptions and approximations used to calculate direct reaction cross sections.

The actual reaction process in DWBA can be broken down into three stages:

1) The projectile and target nucleus approach each other within their Coulomb and nuclear potentials.
2) The transfer is accomplished by a one-step mechanism – for a (p,t) reaction the two neutrons are transferred at the same time, not sequentially.

3) The outgoing particle and the residual nucleus move apart under the influence of their Coulomb and nuclear interactions.

Direct nuclear reactions are often divided into two types: stripping and pickup. In a stripping reaction, part of the projectile is transferred to the target nucleus (e.g. $^{24}Mg(^{3}He,d)^{25}Al$), while in a pickup reaction the projectile "picks up" particles from the target nucleus (e.g. $^{24}Mg(d,^{3}He)^{23}Na$). Although the theory is identical for these two categories of reactions, the conventions and notation differ slightly. For convenience the remaining discussion will use the conventions for pickup reactions since the results will be applied to (p,t) reactions.

2. The Transition Amplitude, $T_{a,b}$

For any nuclear reaction A + a → B + b, commonly denoted by A(a,b)B (A = B + x and b = x + a, where x is the transferred particle(s)), the Schrödinger equation can be written

$$(H-E)\Psi = 0 , \qquad \text{(III-1)}$$

where Ψ is the complete wave function which describes all possible results of the collision, direct reactions as well as elastic scattering, multistep and compound nuclear reactions. The Hamiltonian can be expressed as

$$H = K_a + V_a = K_b + V_b , \qquad \text{(III-2)}$$

where K_a (K_b) is the Hamiltonian outside the range of the interaction potential in the entrance channel, V_a (or exit channel, V_b). K_a includes the kinematics of the system as well as the internal motion of the various particles and nuclei involved. The eigenstates of K_a can be defined as

$$K_a \phi_a = E \phi_a \ . \qquad \text{(III-3)}$$

The transition amplitude or T-matrix for the reaction can now be represented by [To 61]

$$T_{a,b} \equiv \langle \Psi_b^{(-)} | V_a | \phi_a \rangle \ . \qquad \text{(III-4)}$$

This is the "prior" form of the T-matrix which is used for pickup reactions. The (-) superscript is used to indicate there are plane waves and incoming spherical waves in the b channel of the reaction. With this expression for the transition amplitude one can determine the reaction cross section

$$\frac{d\sigma}{d\Omega} = \frac{1}{(2J_i + 1)(2S_i + 1)} \frac{\mu_a \mu_b}{(2\pi\hbar^2)^2} \frac{k_b}{k_a} |T_{a,b}|^2 \ . \qquad \text{(III-5)}$$

Here μ_a and μ_b are the reduced masses in the entrance and exit channels and k_a and k_b are the wave numbers. In general, for a reaction, with non-polarized beam and target, one must average over the spins of the initial channel and sum over the spins in the final channel; thus, the additional factors in (III-5), where J_i and S_i are the spins of target and projectile, respectively.

The basic problem now is to solve for $\Psi^{(-)}$, the complete wave function, which is very complex in its own right, by using potentials which are not fully understood. In practice, to obtain solutions to Equation (III-4) one must truncate $\Psi^{(-)}$ by replacing the exact interaction potential with an effective, phenomenological interaction. The potential that is universally used is the optical model potential (U_a), whose exact form is determined empirically. More details of the optical model will be discussed in the coupled channels section of this Chapter. The two basic restrictions of U_a are that $U_a \to 0$ as $r_a \to \infty$ and that U_a be diagonal in the "a" channel. The eigenfunctions of this potential, usually called the "distorted waves," are determined from the expression

$$(K_a + U_a - E)\xi_a = 0 \ . \qquad \text{(III-6)}$$

Introducing this new potential using a Gell-Mann, Goldberger transformation for scattering from two potentials [To 61], Equation (III-4) becomes

$$T_{a,b} = \langle \Psi_b^{(-)} | V_a - U_a | \xi_a^{(+)} \rangle \ , \qquad \text{(III-7)}$$

where the (+) superscript indicates plane waves plus outgoing spherical waves in the "a" channel. Since the dominant process in most reactions is elastic scattering, it follows that the major component of the interaction V_a should reflect this. If U_a is taken to be the observed optical potential,

then $V_a - U_a \simeq V_{xa}$ becomes the perturbing residual interaction responsible for the reaction. Thus, in general form, Equation (III-7) becomes

$$T_{a,b} \simeq \langle \Psi_b^{(-)} | V_{xa} | \xi_a^{(+)} \rangle \ . \qquad \text{(III-8)}$$

Now with a small interaction potential, V_{xa}, perturbation techniques can be used, in this case the first-order Born approximation. In the Born approximation $\Psi_b^{(-)}$ can be expressed as

$$\Psi_b^{(-)} \simeq e^{i\vec{k}\cdot\vec{r}} + T_{a,b} \frac{e^{ikr}}{r} \ , \qquad \text{(III-9)}$$

where $e^{i\vec{k}\cdot\vec{r}}$ is the incident plane wave. A more physical expression contains the distorted waves rather than the plane waves, because of the presence of an interaction potential as the incident particle approaches the nucleus. The first-order Born approximation with distorted waves consists of truncating $\Psi_b^{(-)}$ to

$$\Psi_b^{(-)} \simeq \xi_b^{(-)} \ , \qquad \text{(III-10)}$$

so that the expression for $T_{a,b}$ becomes

$$T_{a,b}^{DWBA} \simeq \langle \xi_b^{(-)} | V_{xa} | \xi_a^{(+)} \rangle \ . \qquad \text{(III-11)}$$

From Equation (III-2) K_a can be defined as

$$K_a = H_a + H_A + T_a \ , \qquad \text{(III-12)}$$

with

H_a = internal Hamiltonian for the incident particle a ,

H_A = internal Hamiltonian for the target nucleus A, and

T_a = kinetic energy of relative motion.

The associated eigenfunctions for these Hamiltonians are derived from the following expressions

$$(H_A - E^A_{J_i})\Phi^{J_i}_A(\vec{A}) = 0 \qquad \text{(III-13a)}$$

$$(H_a - E^a_{S_i})\Phi^{S_i}_a(\vec{a}) = 0 \qquad \text{(III-13b)}$$

$$(T_a + V_a - E^a_i)\chi_{a_i} = 0 \ , \qquad \text{(III-13c)}$$

where $\vec{A}$ and $\vec{a}$ are the internal coordinates and

$$E = E^A_{J_i} + E^a_{S_i} + E^a_i \ . \qquad \text{(III-14)}$$

Since each Hamiltonian spans a different space, the distorted waves can be expressed as a product of target and projectile internal wave functions along with an expression for the relative motion involved. Thus

$$\xi^{(+)}_{a_i} = \Phi^{J_i}_A(\vec{A})\Phi^{S_i}_a(\vec{a})\chi^{(+)}_{a_i} \qquad \text{(III-15a)}$$

and

$$\xi^{(-)}_{b_f} = \Phi^{J_f}_B(\vec{B})\Phi^{S_f}_b(\vec{b})\chi^{(-)}_{b_f} \ . \qquad \text{(III-15b)}$$

In a typical pickup reaction the relative motion wave functions are a function of the relative momentum and a relative coordinate between the particles in each channel. Figure III–1 displays the coordinate system used in this

Figure III-1. Coordinate System Used for Pickup Reactions, Denoted by A(a,b)B, Where b = a + x and A = x + B.

COORDINATE SYSTEM FOR PICKUP REACTIONS

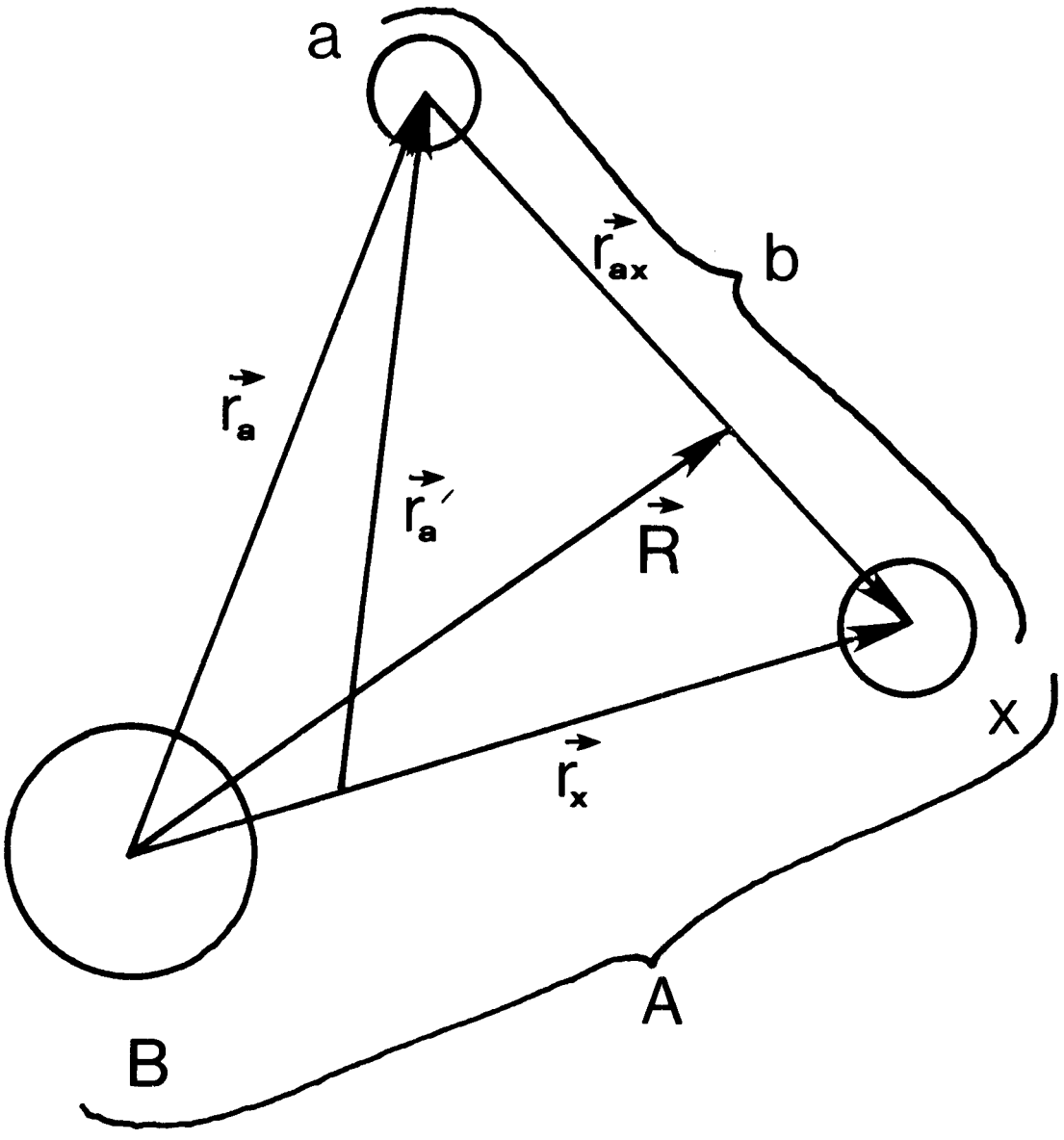

A(a,b)B

Figure III-1.

derivation for pickup reactions. The expressions for the relative coordinates of $\chi_{a,b}$ are

$$\vec{R} \equiv \frac{m_a \vec{r}_a + m_x \vec{r}_x}{m_a + m_x}$$

and (III-16)

$$\vec{r}_a' \equiv \vec{r}_a - \frac{m_x}{m_x + m_B} \vec{r}_x \ ,$$

where m_x, m_a, and m_B are the masses of x, a, and B, respectively. Thus, $\chi_a^{(+)}$ is a function of $\vec{k}_a$ and $\vec{r}_a'$, and $\chi_b^{(-)}$ depends on $\vec{k}_b$ and $\vec{R}$. Now, after substituting Equation (III-15) into (III-11)

$$\begin{aligned} T_{a,b}^{DWBA} &= \int d\vec{r}_a d\vec{r}_x \chi_b^{(-)*}(\vec{k}_b, \vec{R}) \\ &\quad \times \langle \Phi_B^{J_f} \Phi_b^{S_f} | V_{ax} | \Phi_a^{J_i} \Phi_a^{S_i} \rangle \\ &\quad \times \chi_a^{(+)}(\vec{k}_a, \vec{r}_a') \ . \end{aligned} \tag{III-17}$$

Next, a parentage expansion, relating A to B and b to a, can be defined for Φ_A and Φ_b

$$\Phi_A^{J_i}(\vec{A}) = \sum_{\ell\sigma JJ'} F_{\ell\sigma J}(r_x) [\Phi_B^{J'}(\vec{B}) [Y_\ell(\hat{r}_x) \Phi_x^\sigma(\vec{x})]_J]_{J_i}$$

(III-18a)

and

$$\Phi_b^{S_f}(\vec{b}) = \sum_{\lambda\sigma SS'} E_{\lambda\sigma S}(r_{ax}) [\Phi_a^{S'}(\vec{a}) [Y_\lambda(\hat{r}_{ax}) \Phi_x^\sigma(\vec{x})]_S]_{S_f} \ ,$$

(III-18b)

where the brackets represent angular momentum couplings:

$$[Y_\ell(\vec{r}_x) \Phi_x^\sigma(\vec{x})]_J^M \equiv \sum_{m_\ell m_\sigma} (\ell m_\ell \sigma m_\sigma | JM) \ Y_\ell^{m_\ell} \Phi_x^\sigma(\vec{x}) \ . \tag{III-19}$$

$F_{\ell\sigma J}(r_x)$ and $E_{\lambda\sigma s}(r_{ax})$ are called the nuclear and projectile form factors. These will be discussed in more detail later. The quantity in parentheses is a Clebsch-Gordan coupling coefficient, the $Y_\ell^{m\ell}$ are the spherical harmonics and $\Phi_x^\sigma(\vec{x})$ is the internal wave function for the transferred group, x, with angular momentum σ. The quantum numbers ℓ and λ, defined in Equation (III-18), denote the angular momentum of "x" within A and "b" respectively. By inserting Equation (III-18) into the expression for T^{DWBA} and integrating over $\vec{B}$, $\vec{a}$, and $\vec{x}$, one obtains

$$T^{DWBA}_{a_i b_f} = \sum_{LSJ} [(2L+1)(2S+1)]^{1/2} (J_f M_f JM | J_i M_i)$$

$$\times (S_i M_i SM | S_f M_f)(LM_L SM | JM) \Gamma^M_{LSJ} , \qquad \text{(III-20)}$$

where

$$\Gamma^M_{LSJ} = \int d\vec{r}_a d\vec{r}_x \chi^{(-)}_{b_f}(\vec{k}_b, \vec{R}) f_{LSJ}(\vec{r}_a, \vec{r}_x) \chi^{(+)}_{a_i}(\vec{k}_a, \vec{r}'_a) . \qquad \text{(III-21)}$$

The form factor, f_{LSJ}, contains all the nuclear structure information involved in the reaction,

$$f_{LSJ}(\vec{r}_a, \vec{r}_x) = \sum_{\ell\sigma\lambda} (-1)^{\lambda - m_\lambda} (\lambda m_\lambda \ell m_\ell | LM)$$

$$\times W(\lambda\sigma LJ; S\ell) F_{\ell\sigma J}(r_x) \qquad \text{(III-22)}$$

$$\times E_{\lambda\sigma S}(r_{ax}) V(\vec{r}_{ax}) Y^{m_\ell *}_\lambda(\hat{r}_{xa}) ,$$

where $W(\lambda\sigma LJ; S\ell)$ represents a Racah coefficient. In the

expressions above, J, L, and S are the transferred total, orbital, and spin angular momenta, respectively. The angular momenta and spins along with their couplings are defined by the following expressions:

$$\begin{aligned}
\vec{J}_i + \vec{J} &= \vec{J}_f \\
\vec{S}_i + \vec{S} &= \vec{S}_f \\
\vec{L} + \vec{S} &= \vec{J} \\
\vec{\lambda} + \vec{\ell} &= \vec{L} \\
\vec{\lambda} + \vec{\sigma} &= \vec{S} \\
\vec{\ell} + \vec{\sigma} &= \vec{J} \ .
\end{aligned} \tag{III-23}$$

These relations are used in the determination of the selection rules for a particular reaction.

Substituting (III–20) into Equation (III–5) one obtains the following expression for the DWBA cross section:

$$\frac{d\sigma^{DWBA}}{d\Omega} = \frac{\mu_i \mu_f}{(2\pi\hbar^2)^2} \frac{k_b}{k_a} \frac{1}{(2J_i + 1)(2S_i + 1)} \times \sum_{\substack{m_i m_f \\ M_i M_f}} |T^{DWBA}|^2 \ . \tag{III-24}$$

Now, by utilizing the orthogonality relations of the Clebsch-Gordan coefficients and Equations (III–20, 21, 22),

$$\frac{d\sigma^{DWBA}}{d\Omega} = \frac{\mu_i \mu_f}{(2\pi\hbar^2)^2} \frac{k_b}{k_a} \frac{(2S_f + 1)}{(2S_i + 1)} \sum_{JM} \left| \sum_{LS} \Gamma^M_{LSJ} \right|^2 \tag{III-25}$$

With this final expression of the DWBA cross section, the

remaining task is to evaluate the form factor, f_{LSJ} , which contains all the nuclear information.

3. The Nuclear Form Factor

From Equation (III–21) one sees that the expression containing the form factor contains a six-dimensional, nonseparable integral. This integral can be simplified by making a further assumption about the mechanism of the actual transfer of the particle group, x. It has been stated earlier that the process is assumed to take place in one step rather than by a sequential method. This is often referred to as the cluster transfer method. At this point, it is practical to assume that particle b is emitted at the same point at which particle a is absorbed. This is known as the zero-range approximation. Physically this implies that $\vec{r}_a = \vec{r}_x$, which effectively reduces the integral in (III–21) to a tractable, three dimensional integral. This approximation has been shown [Ba 71] to be especially suitable for 0s–shell projectiles (p, d, t, ^{3}He, α), which implies "a" and "x" are in a relative s–state or $\lambda = 0$ in (III–23). The primary effect of the use of this approximation is an overall renormalization of the strength of the calculated cross sections.

Equation (III–22) can now be reduced with the zero-range approximation using the relation

$$V_{ax}(\vec{r}_{ax}) E_{\lambda\sigma s}(r_{ax}) = D_o(\vec{r}) \delta(\vec{r}_{ax}) \ , \qquad \text{(III-26)}$$

where $D_o(\vec{r})$ is the zero-range function, and $\delta(\vec{r}_{ax})$ is the Kronecker delta function. Also, $\vec{r} = \vec{r}_2 - \vec{r}_1$, which is the distance between the two neutrons in the case of a (p,t) reaction. The zero-range function can be written as

$$D_o(\vec{r}) = D_o \phi_b(\vec{r}_x) \ , \qquad \text{(III-27)}$$

where, for (p,t), ϕ_b is the triton wave function.

So, substituting (III-26, 27) into the expression containing the form factor,

$$I^{ZR}_{LSJM} = \frac{D_o}{\sqrt{(2S+1)(2L+1)}} \int d\vec{r}_a \chi_b^{(-)}(\vec{k}_b, \vec{r}_a) F_{LSJ}(\vec{r}_a) \phi_b(\vec{r}_a)$$
$$\times Y_L^{M_L}(\hat{r}_a) \chi_a^{(+)}(\vec{k}_a, \frac{m_B}{m_B + m_x} \vec{r}_a) \ . \qquad \text{(III-28)}$$

D_o can be determined for a particular reaction by substituting the appropriate expressions for V_{ax} and $E_{\lambda\sigma s}$. In the case of (p,t) reactions the form of V_{ax} and $E_{\lambda\sigma s}$ is taken to be a gaussian shape [Ba 73]. Note that the variable of the distorted waves have also been simplified because of $\vec{r}_a = \vec{r}_x$ which implies

$$\vec{R} = \vec{r}_a ,$$

and

$$\vec{r}_a' = \frac{m_B}{m_B + m_x} \vec{r}_a \ .$$

The distorted-waves are usually described in terms of a partial wave expansion,

$$\chi_a^{(+)} = \frac{4\pi}{k_a r_a} \sum_{L_a M_a} (i)^{L_a} \exp(i\sigma_{L_a}) f_{L_a}(k_a, r_a) Y_{L_a}^{m_a}(\hat{r}_a) Y_{L_a}^{m_a *}(\hat{k}_a)$$

(III-29)

and similarly for $\chi_b^{(-)}$. Here $L_a(L_b)$ represents the angular momenta of the partial waves, the σ_{L_a} are the Coulomb phase-shifts, and f_{L_a}, f_{L_b} are the radial functions as determined from the solution of the optical model eigenvalue equation. The number of partial waves in a particular reaction at these energies (35 MeV) is primarily a function of the Z of the projectile and nucleus (or the range of their Coulomb interaction). Making these partial wave expansions for the distorted-wave gives

$$\begin{aligned} i^L \Gamma_{LSJ}^M = & \sum_{\substack{L_a L_b \\ M_a M_b}} (i)^{L_a - L_b - L} \exp(i\sigma_{L_a}) \\ & \times \exp(i\sigma_{L_b}) \left[\frac{4\pi(2L_b + 1)}{(2L_a + 1}\right]^{1/2} \\ & \times (L_b 0 L 0 | L_a 0)(L_b M_b L M | L_a M_a) \\ & \times Y_{L_b}^{M_b}(\hat{k}_b) Y_{L_a}^{M_a}(\hat{k}_a) I_{L_b L_a}^{LSJ} \end{aligned}$$

(III-30)

and

$$I_{L_b L_a}^{LSJ} = \int_0^\infty F_{LSJ}(r_a) f_{L_b}(k_b, r_a) f_{L_a}\left(k_a, \frac{m_B}{m_x + m_B} r_a\right) d\vec{r}_a \ .$$

(III-31)

Note that the Clebsch-Gordan coefficients require $L_b + L = L_a$

and that $(L_B 0 L 0 | L_a 0)$ vanishes unless $L + L_a + L_b$ is even. This result, along with the conservation of parity,

$$\pi_a \pi_A (-1)^{L_a} = \pi_b \pi_B (-1)^{L_b} , \qquad \text{(III-32)}$$

requires that for the parity change of the reaction

$$\Delta\pi = \pi_a \pi_A \pi_b \pi_B = (-1)^{L_a + L_b} = (-1)^L . \qquad \text{(III-33)}$$

This condition is often termed the natural parity selection rule. This is a direct result of the zero-range approximation and is not true for a full finite-range calculation.

Returning now to the explicit evaluation of the form factor for (p,t) reactions, $F_{LSJ}(r_x)$ can be expanded in terms of single-particle wave functions, U_{q_i}, where the q_i are the neutron shell-model quantum numbers, $n_i \ell_i j_i$, and

$$F_{LSJ}(r_x) = \sum_{q_1 q_2} S_J^{1/2} U_{q_1}(\vec{r}_1) U_{q_2}(\vec{r}_2), \qquad \text{(III-34)}$$

where $S_J^{1/2}$ is the spectroscopic factor defined by deShalit and Talmi [De 63] for (p,t) reactions:

$$S_J^{1/2} = \frac{\langle \psi^{J_i}(\vec{A}) || a^\dagger_{n_1}(r_1) a^\dagger_{n_2}(r_2) || \psi^{J_f}(\vec{A} - 2) \rangle}{(2J_i + 1)^{1/2}} \qquad \text{(III-35)}$$

Here, $a^\dagger_{n_1}$ and $a^\dagger_{n_2}$ are creation operators for the two neutrons being transferred, and ψ^{J_i} and ψ^{J_f} are the wave functions of the target and residual nuclei. The single particle wave functions are determined by solving the Schrödinger equation for a bound particle in a Woods-Saxon shaped potential, where

the well depth is adjusted to give each neutron one-half the two-neutron binding energy.

In general, determining the form factor for two-particle transfer reactions can be very difficult. Unlike the procedure for single nucleon transfer reactions, the form factor cannot be broken up into a radial part and a strength factor because of the coherent sum taken over many possible particle couplings (see (III-34)). In single nucleon transfer the summation in (III-34) disappears since the transfer usually involves only one particular orbital of a shell. A similar situation can be obtained in a two-particle transfer reaction by assuming a pure two-particle pickup configuration giving $S_J^{1/2} = 1$ and thus allowing the radial dependence of F_{LSJ} to be determined separately. This procedure is often used in (p,t) reactions when accurate shell model wave functions are not known [Ba 73, Br 73]. This simplification was used in this study and is discussed further in Chapter V.

Two interesting features of two-nucleon transfer reactions which have made them a widely used method of examining nuclei are the distinctive diffraction-like shape of the L = 0 transitions and the concentration of the total cross section in the ground state to ground state transition for even-even nuclei (except near closed shells). Most of the angular distributions are expected to have some diffractive-type shape, since they result from a superposition of

waves scattering from all parts of the nuclear surface. However, the L = 0 transitions display this feature much more so than higher L-transfers. This can be traced in part to the limited number of couplings that are allowed between the incoming and outgoing partial waves. Thus there are fewer terms in the superposition of the waves that can interfere and destroy the diffraction pattern. The explanation of the strong ground state to ground state transitions can be understood in terms of the pairing model of the nucleus [Br 73], where the ground states of even-even nuclei are considered to be "superconducting" states composed of many coherent pairs of nucleons. Thus, a two-nucleon transfer reaction is quite sensitive to these pairing correlations. The large cross sections result from the coherent sum taken over the many configurations that may be involved in the transfer (see Equation (III-34)).

B. The Coupled Channels (CC) Method For Inelastic Scattering

1. Introduction

In most inelastic scattering experiments the common starting point for analysis is usually with the DWBA [Ba 62], using a collective model form factor (see discussion in Section B.4). One of the major advantages of this method is its relative simplicity, as it deals with only one channel of the reaction and thus the numerical methods involve the

solving of uncoupled equations. The reason for the success of the DWBA method is a direct result of the comparatively weak interaction which causes the reaction and allows for the perturbation treatment. However, in some scattering reactions there are strong couplings between various levels of the target nucleus. When this occurs multi-step effects become significant in accounting for the varying strengths and shapes of the angular distributions. This feature is observed in scattering studies with the collective, well-deformed nuclei where the majority of the inelastic strength appears in the strongly coupled states of the ground band. Improvements in the DWBA method can be obtained by using second or higher order Born approximations. However, the computational difficulty is greatly increased. More improvement can be achieved by using the coupled channels method, where the interaction is treated to all orders and the number of levels that can be coupled is basically determined by computer size. Figure III–2 depicts the various excitation routes available in the CC and DWBA inelastic scattering methods. The DWBA method can only account for the "up" transitions of a, b, and c, the direct transitions. The CC method can calculate all transitions in Figure III–2 to all orders of the allowed angular momentum coupling (i.e. d has L = 2, 4, 6 components). For example, in the population of the 4^+ level, the CC method includes pathways such a + d, c + e, a + g + d (where g represents the

Figure III-2. Various Coupling Routes in the Coupled Channels Method of Inelastic Scattering. The "up" transition of a, b, and c can be calculated in the DWBA.

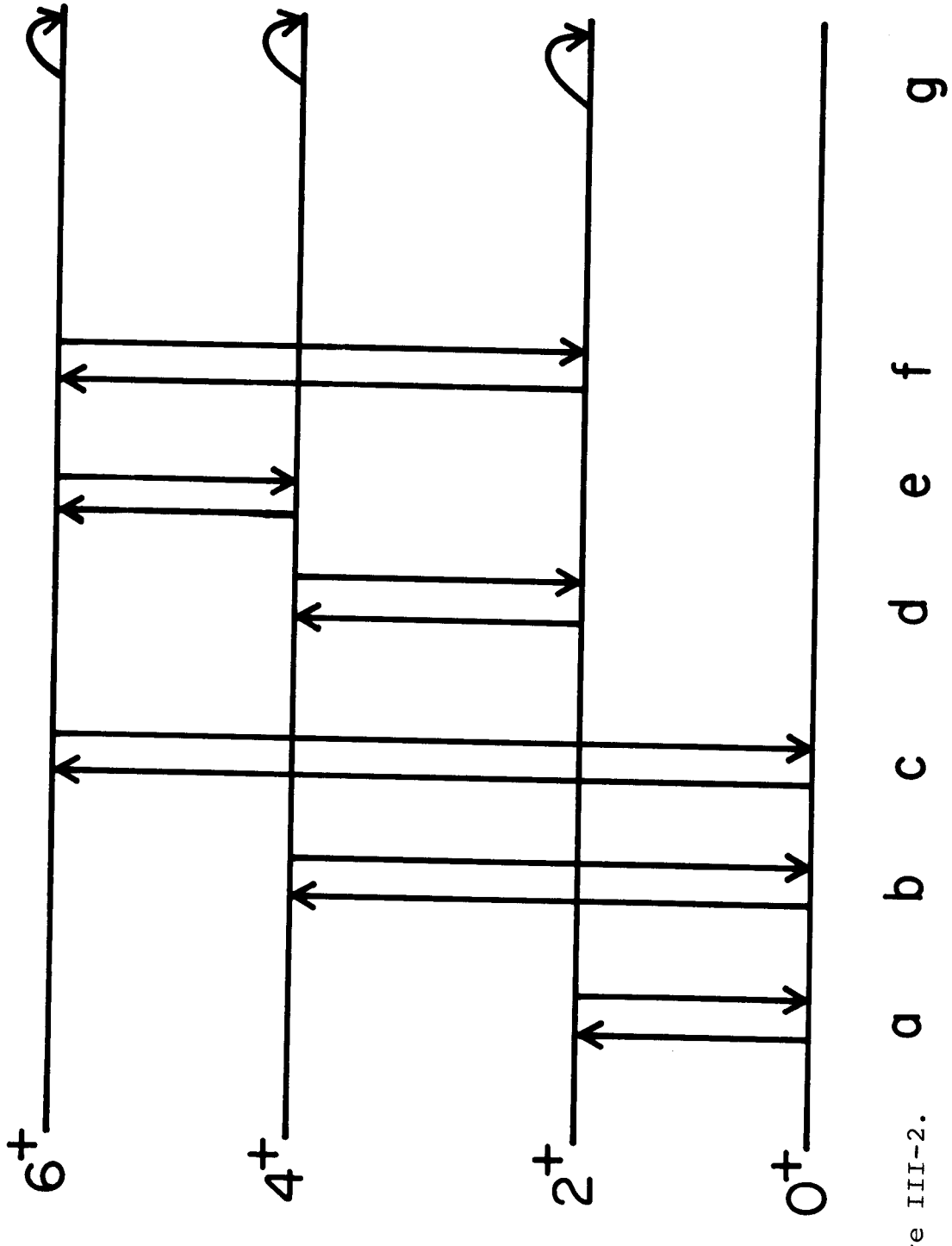

Figure III-2.

reorientation effect), and b, plus higher order multi-step paths, all of which can be included in one calculation. Although the computational problems encountered when solving many coupled equations are quite involved, their solutions result in a more complete treatment of the scattering problem.

2. The Coupled Equations

The basic scattering problem is identical to that shown in the previous section on the DWBA. Solutions of the full Schrödinger equation,

$$(H - E)\Psi(\vec{r}, \vec{A}) = 0, \qquad \text{(III-36)}$$

will be sought for the scattering system with appropriate boundary conditions and an expansion of $\Psi_{\alpha J}(A)$. Defining H_A as the Hamiltonian for the nucleus of mass A and with internal coordinates $\vec{A}$, the nuclear eigenfunctions are defined by

$$(H_A - E_{\alpha J})\Psi_{\alpha J}(\vec{A}) = 0 \ , \qquad \text{(III-37)}$$

where $E_{\alpha J}$ is the energy of state αJ and α represents all remaining quantum numbers needed to describe the state. For the system of the nucleus and scattered particle (in this derivation, a proton) the full Hamiltonian can be expressed as

$$H = H_A + T + V(\vec{r}, \vec{A}) \qquad \text{(III-38)}$$

where T is the kinetic energy of the proton, and V is the interaction of the proton with the nucleus. The spin-orbit functions of the proton are given by

$$Y^{m}_{\ell sj} = [Y_{\ell}(\hat{r})\chi(\sigma)]^{m}_{j} , \qquad \text{(III-39)}$$

or explicitly showing the couplings

$$Y^{m}_{\ell sj} = \sum_{m_\ell m_s} i^{\ell}(\ell m_\ell s m_s | j m_j) Y_{\ell}(\hat{r})\chi(\sigma) , \qquad \text{(III-40)}$$

where χ is the spin function for the proton. For clarity, all the quantum numbers which describe a particular state of the nucleus and proton and their relative angular momenta before the collision will be denoted by $C = \alpha J \ell s j$ and all other states formed as a result of the collision by c'. By combining the wave functions for the nucleus and proton, the functions of total angular momentum, I, and parity, π, are obtained

$$\phi^{M}_{C\pi I}(\hat{r}, \sigma, \vec{A}) = [Y_{\ell_{sj}} \Phi_{\alpha J}]^{M}_{I} , \qquad \text{(III-41)}$$

with

$$\vec{I} = \vec{j} + \vec{J}, \quad \pi = (-1)^{\ell}\pi_{\ell} . \qquad \text{(III-42)}$$

Now an expansion of $\Psi(\vec{r}, \vec{A})$ in (III-36) can be performed in terms of the total angular momentum and parity,

$$\Psi^{M}_{C\pi I}(\vec{r},\vec{A}) = \frac{1}{r} \sum_{C'} u^{C\pi I}_{C'}(r)\phi^{M}_{C'\pi I}(\hat{r}, \sigma, \vec{A}) \qquad \text{(III-43)}$$

Inserting this expansion into (III-36), multiplying from the left by the complex conjugate of (III-41), and making use of

the orthonormality of the ϕ functions, a set of coupled equations for the radial functions u(r) of the scattered proton is obtained for each I and π of the system. For each channel c', the coupled equations have the form

$$(T_{c'} + V^{I}_{c'c'}(r) - E_{c'})u_{c'}(r) = - \sum_{c''\neq c'} V^{I}_{c'c''}(r)u_{c''}(r), \qquad \text{(III-44)}$$

where

$$T_{c'} = \frac{\hbar^2}{2m}\left(\frac{d^2}{dr^2} + \frac{\ell(\ell+1)}{r^2}\right), \quad k^2_{c'} = \frac{2m}{\hbar^2}E_{c'},$$

$$E_{c'} = E - E_{\alpha j}, \qquad \text{(III-45)}$$

with E denoting the incident proton energy. Note that the potential, V, has been broken up into the diagonal terms, on the left side of (III-44), and the off-diagonal, coupling terms on the right. Also

$$V^{I}_{c'c''}(r) = \langle\phi_{c'\pi I}(\hat{r},\vec{A})\,|\,V(\vec{r},\vec{A})\,|\,\phi_{c''\pi I}(\hat{r},\vec{A}) \qquad \text{(III-46)}$$

where the integration is over all internal coordinates and the polar angles of $\vec{r}$.

As it stands (III-44) is a system of equations, infinite in number, which must be simplified to achieve any reasonable solutions. The approximation that is made is to limit the number of inelastic channels to those with a large cross section and/or other special states of interest. The problem is now finite and can be solved numerically. As in the DWBA, the interaction will need to be adjusted to account for

channels that were explicitly eliminated. In fact (III-44) can be essentially converted to DWBA by simplifying to one scattering channel. This eliminates the coupled terms on the right side of (III-44).

3. The Effective Interaction: The Optical Model Potential

The introduction of a nuclear model at this point allows for a parameterization of the potential and provides the necessary wave functions, $\phi_{\alpha J}$, for computing the matrix elements in the form factor. Also at this point it is assumed that the orientation of the nucleus does not change significantly during the time the proton is within the range of the interaction. This is referred to as the adiabatic approximation [Gl 67].

The standard form of the interaction potential that is used in most reaction problems is the complex-valued optical model, developed in 1953 by Feshbach, Porter, and Weisskopf [Fe 53]. The shape of the potential is usually that of a diffuse Woods-Saxon, which has the form

$$f(x) = (1 + e^{x})^{-1}, \qquad x = \frac{r - R}{a_R}, \tag{III-47}$$

where $R(= r_R A^{1/3})$ and a_R are the radius and diffuseness parameters. The actual form of the optical potential used in proton scattering is given by

$$V(r) = -(V + iW) f(x) - 4iW_D a_I f'(x_I)$$
$$- V_{SO}(\vec{\sigma}\cdot\vec{\ell})\hbar^2 \frac{1}{r} f'(x_{SO}) \tag{III-48}$$

Here, V, W, W_D, and V_{SO} are the real volume, imaginary volume, imaginary surface, and spin-orbit well depths, x_I and x_{SO} are similar in form to (III-47) except with different values for the radius and diffuseness parameters. Also, $\lambda\!\!\!^{-}$ is the π-meson compton wavelength, and $f'(x) = \frac{df(x)}{dr}$. The real part of the potential represents an average interaction between the projectile and the nucleons of the target, while the imaginary part represents absorption of particles from the incident beam. Thus the imaginary part also fulfills the need to account for the channels not explicitly included in Ψ after truncation.

The scattering from a deformed nucleus is assumed to result from the interaction of the projectile with the part of the nuclear field arising from the deformation. To account explicitly for this, the nuclear shape is parameterized by the usual expression

$$R = R_o[1 + \sum_{\lambda\mu} \beta_{\lambda\mu} Y_{\lambda\mu}(\theta',\phi')] = R + \delta R \ , \qquad \text{(III-49)}$$

with the sums over even values of λ and μ. The parameters θ' and ϕ' refer to the body-fixed (symmetry) axis of the nucleus, and the $\beta_{\lambda\mu}$ are the deformation parameters. Substituting this expression into (III-48), which along with the Coulomb potential, V_{Coul}, has been taken as the effective interaction in (III-46), and expanding V about the spherical shape, one obtains for the nuclear part of V

$$V_{nuc}(r - R) = V_{nuc}(r - R_o) + \sum_{n=1}^{\infty} \frac{(-\delta R)^n}{n!} \frac{\partial^n V}{\partial r^n} \ . \qquad \text{(III-50)}$$

This new form of the optical potential is often called the deformed optical model potential (DOMP). Since

$$\frac{\delta R}{R_o} = \sum_{\lambda \mu} \beta_{\lambda\mu} Y'_{\lambda\mu} \ , \qquad \text{(III-51)}$$

an expression in terms of the generalized deformation parameters, δ, can be obtained by using the addition theorem for spherical harmonics [Ro 57],

$$\left(\frac{\delta R}{R_o}\right)^n = \sum_{LK} \delta^n_{LK} Y'_{LK}$$

$$\delta^n_{LK} = \sum_{\lambda k \mu \Lambda} \left(\frac{\hat{\lambda}\hat{\Lambda}\hat{L}}{4\pi}\right)^{1/2} (\Lambda \mu k | L, -K)(\Lambda 0 \lambda 0 | L0) \qquad \text{(III-52)}$$

$$\times \delta^{n-1}_{\Lambda\mu} \beta_{\lambda k} \quad (\text{for } n > 1),$$

where

$\delta'_{\Lambda\mu} = \beta_{\lambda k}$ and $\hat{L} = 2L + 1$. Now

$$V_{nuc}(r - R) = V_{nuc}(r - R_o) + \sum_{L\mu} N_{L\mu}(r) Y_{L\mu}(\theta', \phi') \ , \qquad \text{(III-53)}$$

where

$$N_{L\mu}(r) = \sum_{n=1}^{\infty} \frac{(-R_o)^n}{n!} \delta^n_{L\mu} \frac{\partial^n V(r)}{\partial r^n} \ . \qquad \text{(III-54)}$$

Likewise, a similar expression can be obtained in terms of the generalized Coulomb deformation parameters, δ^C, for the Coulomb part of the potential (see Reference [Gl 67])

$$V_{Coul}(r') = ZZ'e^2 \int \frac{\rho(r'')}{|\vec{r}' - \vec{r}''|} dr'' \ ,$$

where a variety of charge distributions can be used for $\rho(r'')$. Using the D-functions [Ro 57] to express the

potential in the laboratory frame and combining the nuclear and Coulomb parts of V, one obtains

$$V[r - R(\theta,\phi)] = V(r - R_o) + \sum_{LM} Y_{LM}(\theta,\phi) \sum_{K\geq 0} V_{LK}(r) \times \frac{D^L_{MK} + D^L_{M,-K}}{1 + \delta_{KO}} , \qquad \text{(III-55)}$$

where

$$V_{LK} = N_{LK} + C_{LK} ,$$

the nuclear and Coulomb parts. The first term of (III-55) is just the spherical optical model potential of (III-48) plus the Coulomb potential. This term has only diagonal matrix elements, the $V_{c'c'}$ of (III-44), while the second part of (III-55) is responsible for the excitations of the nucleus from one rotational state to another.

4. The CC Form Factor

The coupling potential can also be written in a general form as

$$V^{I\pi}_{c'c''}(r) = \sum_{\lambda} V_{LK}(r)\,(Q_\lambda \cdot Y_\lambda) \qquad \text{(III-56)}$$

where Q_λ is an operator which operates only on the coordinates of the target nucleus. Comparing the second part of (III-55) with (III-56) yields

$$V^{I\pi}_{c'c''} = \sum_{LSJ} C_{SLJ} F^{\alpha_1 J_1 \alpha_2 J_2}_{LSJ} , \qquad \text{(III-57)}$$

where C_{LSJ} is a geometric factor, defined in Reference [Gl 67], and F_{LSJ} is the form factor

$$F_{LSJ}^{\alpha_1 J_1 \alpha_2 J_2} = V_{LK} \langle J_1 K_1 || Q_L || J_2 K_2 \rangle \ , \qquad \text{(III-58)}$$

where Q_L is the multipole operator of the form

$$\frac{D^L_{MK} + D^L_{M,-K}}{1 + \delta_{K0}} \ ,$$

for the symmetric rotor model. The problem has now been reduced to the evaluation of a series of form factors, which involves determining a set of optical model parameters as well as computing a group of matrix elements.

As an illustration of the coupling nature of this problem, in particular the role of the deformations, β_λ, the form factor for an L = 2 transition in the ground band (K = 0) of a symmetric rotor will be derived. For clarity only the nuclear part of V_{LK} will be used and the δ values of (III-52) will be taken to second order. Starting with (III-58) and substituting the simple expression for the matrix element [Pr 75]

$$F_{L0L}(r) = V_{L0} (\hat{J}_1)^{1/2} (-1)^{J_1 - L} (J_1 0 L 0 | J_2 0) \ . \qquad \text{(III-59)}$$

Taking the expansion of δ to second order

$$\delta^2_{L0} = \sum_{\lambda\lambda'} \left[\frac{\hat{\lambda}\hat{\lambda}'}{4\pi \hat{L}}\right]^{1/2} (\lambda 0 \lambda' 0 | L0) \beta_\lambda \beta_{\lambda'} \ , \qquad \text{(III-60)}$$

where λ and λ' are cut off at 4 and again $\hat{L} = 2L + 1$. Thus explicitly

$$\delta^2 = [\frac{\hat{2}\ \hat{2}}{4\pi\hat{L}}]^{1/2}(2020|L0)^2\beta_2^2 + 2[\frac{\hat{2}\ \hat{4}}{4\pi\hat{L}}]^{1/2}(2040|L0)^2\beta_2\beta_4 + [\frac{\hat{4}\ \hat{4}}{4\pi L}]^{1/2}(4040|L0)^2\beta_4^2 \ . \qquad \text{(III-61)}$$

Now consider a $0^+ \rightarrow 2^+$ transition with $J_1 = 0$, $J_2 = 2$, and $L = 2$. Inserting (III-61) into (III-54) (with no Coulomb part, $V_{L0} = N_{L0}$) and combining with (III-59) one obtains

$$F_{L=2}^{J_1=0,J_2=2} = R_o(\frac{1}{20\pi})^{1/2}[-\beta_2 \frac{\partial V}{\partial r} + \frac{R_o}{2}\frac{\partial^2 V}{\partial r^2}[5(2020|20)^2\beta_2^2 + 2(45)^{1/2}(2040|20)^2\beta_2\beta_4 + 9(4040|20)^2\beta_4^2] \ . \qquad \text{(III-62)}$$

The L = 2 collective model form factor mentioned earlier in the DWBA section is actually the first term of (III-62)

$$F_2 \propto \beta_2 \frac{\partial V}{\partial r} \ . \qquad \text{(III-63)}$$

5. Solving the Coupled Equations

It should be noted that there are considerably more coupled equations than there are nuclear states being considered. This is because "c" labels the nuclear state αJ and the angular momentum of the scattered particle. So for each value of I,π, the total angular momentum and parity of the system, and for each nuclear state αJ, there will be

scattered particles with angular momenta ℓ, j, that satisfy the conditions of Equation (III–42). For spin 1/2 particles there are 2J + 1 such couplings and thus for each I,π value there are

$$N = \Sigma\ (2J + 1) \qquad \text{(III-64)}$$

coupled channels, where the summation is over all states under consideration. For a spin zero projectile, $N = \Sigma\ (J + 1)$. In a calculation of proton scattering on a nucleus where a 0–2–4–6 level sequence is used, there would be a maximum of 28 coupled equations for each I,π and for alpha scattering, N = 16. With the angular momentum of the incident partial waves ranging in value from $\ell = 1$ to $\ell_{max} = 2kR$, where R is the radius beyond which the interactions are effectively zero, and 2j states for each ℓ (for protons), the total number of differential equations that need to be solved is about $4kRN^2$.

The usual method of solving coupled channel problems is to impose boundary conditions on the radial wave functions $u_{c'}$ of Equation (III–44); at the origin, where the functions must go to zero, and in the region where the nuclear potential is negligible, the equations become uncoupled and the u_c's asymptotically become

$$u_{c'} \rightarrow \delta_{c'c} I_c(k_c r) - \left(\frac{k_c}{k_{c'}}\right)^{1/2} S^I_{cc'} O_{c'}(k_{c'} r)\ . \qquad \text{(III-65)}$$

Here the I and O functions are incoming and outgoing waves respectively, which are represented as a linear

combination of the regular and irregular Coulomb functions, F and G. The $S^I_{cc'}$ are the elements of the S-matrix. Two sets of linear algebraic equations can be set up and solved for the matrix elements of $S^I_{cc'}$. The S-matrix is related to the transition matrix, $T_{cc'}$, by

$$S_{cc'} = \delta_{cc'} - 2\pi i T_{cc'} \delta(E_c - E_{c'}), \qquad \text{(III-66)}$$

from which the cross section can be obtained (see Equation (III-5)).

Recently, a new method has been derived for solving equations using a sequential iteration process [Ra 72]. The program which incorporates this method is called ECIS (equations couplees en iteration sequentielle) [Ra 73]. The use of this method is increasing rapidly because of the drastic reduction in computational time in most cases, however, the storage requirement for this method is larger than for the usual methods for coupled equations. The ECIS method actually gives better results than DWBA codes after the first iteration, while the second iteration often gives the same results as the standard coupled channel method. The last iteration, defined by a convergence test on the phase shifts, is required to give the same result as the standard method. The details of both the integral and differential methods used in ECIS are given in Reference [Ra 72].

C. Charge, Mass, and Potential Moments

One of the most fundamental quantities that can be learned from inelastic scattering experiments is the shape of the nucleus. There are basically two methods used to study this property of nuclei with each sensitive to a different aspect of the nucleus. The first method involves low energy hadronic particles for Coulomb excitation, and electron scattering, where both serve as a probe of the charge (proton) distribution in the nucleus. The other group of measurements are made with higher energy hadronic particles that sample the mass distribution of both the neutrons and protons. With these two methods available, one may be able to detect differences in the charge and mass distributions within a nucleus, if they exist. This might be obtained by a comparison of the results from these two methods, however, this in itself is not a straightforward task.

Because the Coulomb interaction is well understood, the measured charge moments can be related to the charge distribution with only a few model dependent assumptions. The L–th moment of a charge distribution can be defined as

$$q_\lambda \equiv M(E\lambda;\mu) = \int r^\lambda Y_{\lambda\mu}(\theta,\phi)\,\rho_c(\vec{r})\,d\vec{r} \ , \qquad \text{(III-67)}$$

where ρ is the nuclear charge density. This is also the same form for the electric multipole operator and can be related to the reduced matrix elements for γ–decay in a collective nucleus

$$\langle JMK|M(E_\lambda)|JMK\rangle = (2J_f + 1)^{-1/2}(J_i M_i \lambda\mu | J_f M_f)$$

$$\times \langle J_f||M(E_\lambda)||J_i\rangle \ , \qquad \text{(III-68)}$$

By specifically introducing the reduced transition probability, B(Eλ), for quadrupole transitions on obtains

$$B(E2, J_i \to J_f) = (2J_i + 1)^{-1}|\langle J_f||M(E2)||J_i\rangle|^2 \ . \qquad \text{(III-69)}$$

Thus, the charge moment, q_λ, is equal to the matrix element in special cases

$$q_\lambda^2 = B(E\lambda, 0 \to J_f) = M(E\lambda, 0 \to J_f)^2 \ . \qquad \text{(III-70)}$$

In summary the measured experimental quantities are the q_λ's which can be related to the charge distribution by (III–67), where ρ_c is the only model dependent term.

This rather direct approach of relating the measured quantity to the underlying density is not available for the high-energy scattering measurements because the nuclear force is not well understood. This mandates the use of an effective interaction for the analysis of the data. One method is to use a deformed optical model potential (DOMP), which introduces additional uncertainties in any attempt to relate the deformation parameters of the DOMP to the more physically relevant mass distribution. This study will follow the suggestion of Mackintosh [Ma 76] and discuss the results in terms of normalized potential moments. These are equivalent to the mass moments of the nuclear if the

underlying nucleon-nucleon interaction is assumed to be independent of the local density [Sa 72, Ma 76]. There is also evidence [Ma 74a] that this method is less model dependent and thus more fundamental than the usual deformation parameter, β_λ, or the deformation lengths, $\beta_\lambda R$ ($R = r_o A^{1/3}$). The L-th multipole of the DOMP is defined as

$$q_\lambda \equiv \frac{K\int V(r - R(\theta)) r^\lambda Y_{\lambda o}(\theta) d\vec{r}}{\int V(r - R(\theta)) d\vec{r}} \quad , \qquad \text{(III-71)}$$

where $V(r - R(\theta))$ is the real part of the optical potential and K is chosen to be Z, the atomic number. This gives a charge component of the potential for comparison with the charge moments measured in electron scattering, or Coulomb excitation from low energy hadron scattering.

With the results of the two types of measurements cast in a form to facilitate their comparison, one now must judge whether any difference between the charge and potential moments actually reflects a difference between the charge and mass distributions of the nucleus, or whether it is the result of ignoring the density-dependence of the nucleon-nucleon interaction, or one of the other assumptions used in this method. Calculations [Ha 77] for ^{154}Sm indicate a 20–30% difference may exist between the potential and mass moments. This implies an even more detailed approach may be needed to extend these methods to measure differences in charge and mass distributions of deformed nuclei.

CHAPTER IV

EXPERIMENTAL PROCEDURES AND DATA ANALYSIS

A. Introduction

An important consideration in undertaking this reaction study was the quality of proton beams available from the MSU cyclotron. The MSU cyclotron is a variable energy, sector-focused machine with single-turn extraction capabilities. The single-turn extraction results in a very small spread in energy of extracted beam, typically ≈ 0.1% of the beam energy. This property, when combined with proper spatial correlations of the beam, allows one to operate the cyclotron-spectrograph system in the dispersion matching [Co 59, Bl 71] or energy-loss mode, which will typically result in 5–10 keV full width half maximum (FWHM) resolution for inelastic scattering of 35 MeV protons, and 1.5 keV under ideal conditions [No 75]. Although the level density in the even-even Pt nuclides studied is not very great below 1.5 MeV, nevertheless, resolution and low background are very important in a reaction where the population of weak states is of prime concern, as was the case in the (p,t) reactions.

B. Proton Beam and Transport System

The 35 MeV proton beam was used in both reactions studied, primarily for two reasons. In the (p,t) reactions, the maximum energy tritons that the Enge-split pole spectrometer can bend is approximately 30 MeV, so with the Q-values for these reactions near -5.0 MeV, a 35 MeV beam will produce the maximum energy tritons for the spectrometer. The highest energy tritons are desirable because a more oscillatory diffraction pattern will result. The 35 MeV proton beam is also one of the most reliable beams available on the MSU cyclotron, with highly reproducible set-up conditions for the cyclotron and beam lines. Beam currents are typically 1 to 2 μA on target.

Figure IV-1 shows the relationship of the cyclotron, the beam transport system, and vault 3 where the spectrograph is located. The transport system includes three bending magnets (M3, M4, and M5), two intermediate focus points (box 3 and box 5), and several sets of quadrupole doublet focusing magnets.

These quadrupole doublets are primarily used to achieve the dispersion matching conditions discussed below. The beam energies are determined by proton NMR readings in M3 and M4. Figure IV-2 shows the scattering chamber and the Enge split-pole spectrograph. The targets are located in the center of the scattering chamber, housed in a remotely controlled "ladder" capable of holding three targets and a scintillator,

Figure IV-1. Experimental Vault Area at the MSU Cyclotron Laboratory. The experiments in this study were conducted in Vault 3 with the Enge spectrograph and associated beam optics.

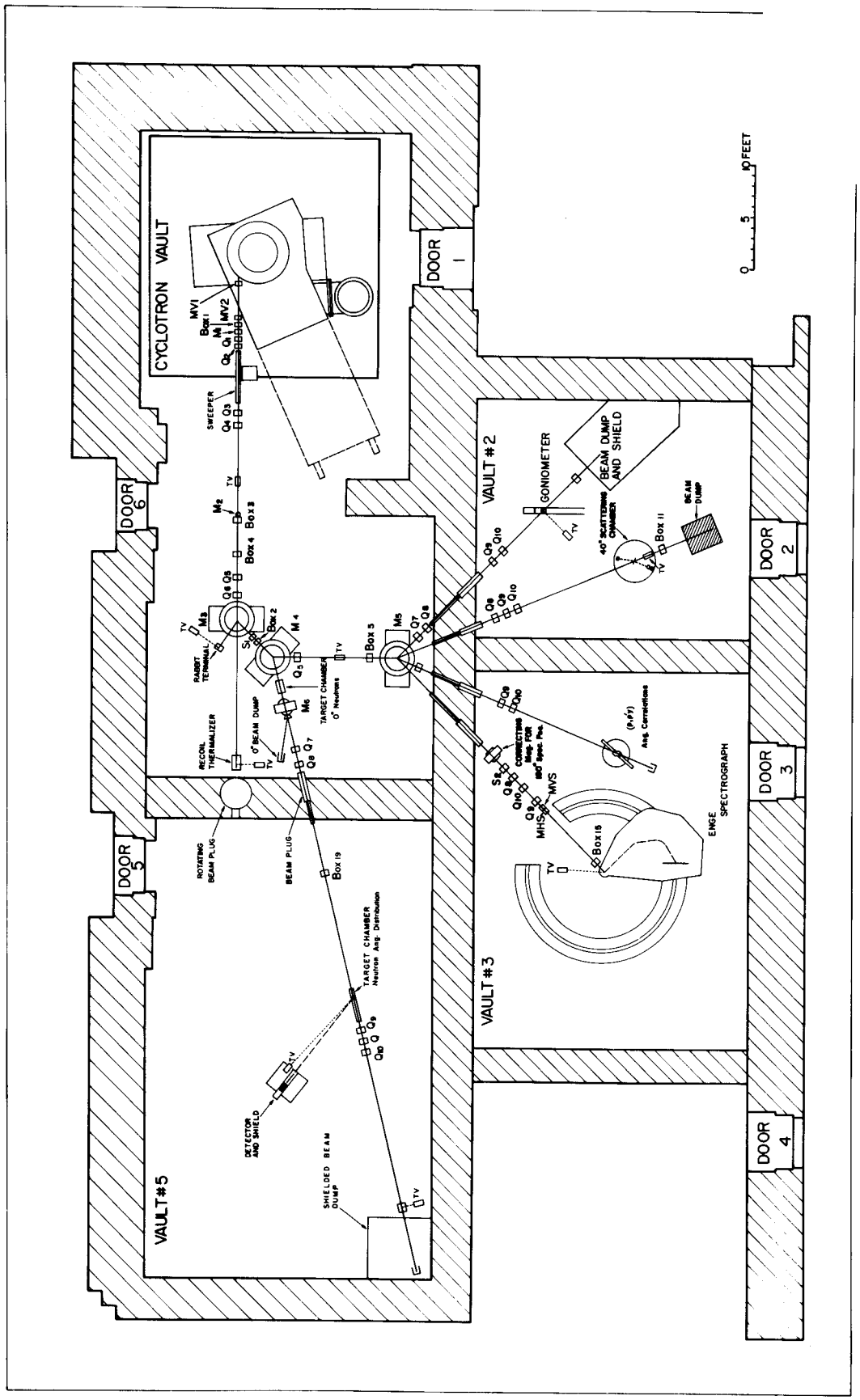
CYCLOTRON VAULT
VAULT #2
VAULT #3
VAULT #5
DOOR 1
DOOR 2
DOOR 3
DOOR 4
DOOR 5
DOOR 6
GONIOMETER
BEAM DUMP AND SHIELD
ENGE SPECTROGRAPH
TARGET CHAMBER
Neutron Ang. Distribution
SHIELDED BEAM DUMP
DETECTOR AND SHIELD
ROTATING BEAM PLUG
BEAM PLUG
RECOIL THERMALIZER
RABBIT TERMINAL
SWEEPER
0 5 10 FEET

Figure IV-1.

Figure IV-2. Schematic Drawing of Scattering Chamber and Enge Split-Pole Spectrograph. The detectors and plates are placed inside the camera box in the focal plane of the spectrograph.

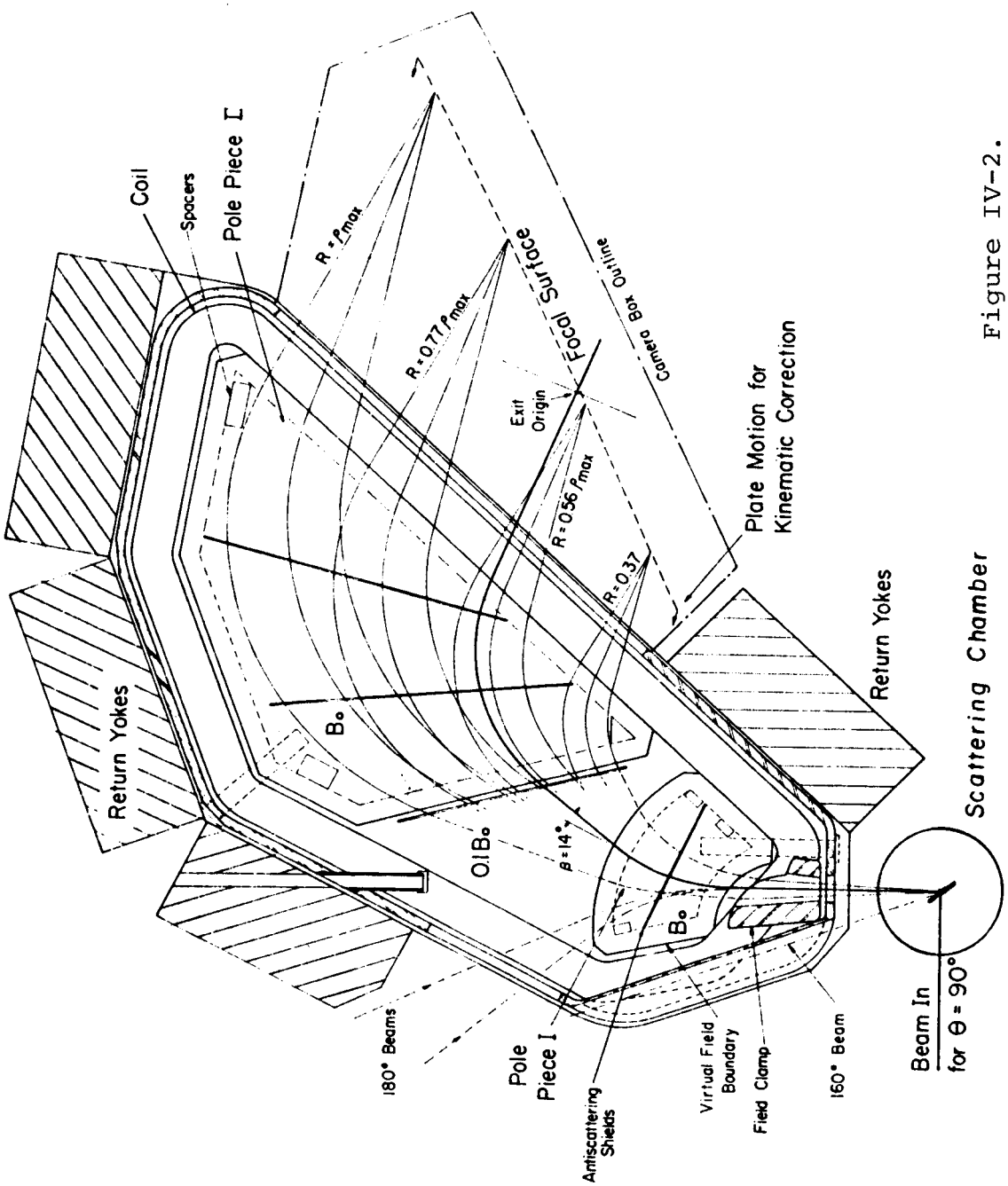
Coil
Spacers
Pole Piece II
R = fmax
R = 0.77 fmax
Focal Surface
Exit Origin
R = 0.56 fmax
R = 0.37
Camera Box Outline
Plate Motion for Kinematic Correction
Return Yokes
Return Yokes
Bo
0.1Bo
β = 14°
Bo
180° Beams
Pole Piece I
Antiscattering Shields
Virtual Field Boundary
Field Clamp
160° Beam
Beam In
for θ = 90°
Scattering Chamber

Figure IV-2.

which is used for visually adjusting the focusing and shape of the beam spot in the target plane. The amount of beam on the target was monitored with a 0^{o} Faraday cup with a current integrator. The beam and target conditions were monitored with a well shielded NaI (Tℓ) detector placed at 90^{o} to record elastically scattered protons. Two aperture sizes were used in the reactions: for the (p,t) study a 2^{o} x 2^{o} aperture corresponding to a solid angle of 1.15 millisteradians, and for (p,p') the 2^{o} x 2^{o} as well as a 1^{o} wide by 2^{o} high aperture or 0.60 msr.

The reaction products were analyzed with the Enge split pole spectrograph with particle groups of the same momentum focused at the detector plane. The use of a magnetic device in particle reactions allows one to select preferentially particles of given types and energies to be incident on the counter. Since different particles with varying energies have different magnetic rigidities (particle momentum divided by its charge), the magnetic field can be adjusted to study only particular groups of one particle type. This technique worked very well for the (p,t) reactions because of the large negative Q-value. However, in the (p,p') reactions, there is a small background due to a virtual continuum of high energy deuterons and γ-rays entering the counter and even a discrete state from the $^{12}C(p,d)^{11}C$ (g.s.) reaction which appears near the ground state. But the majority of deuterons and tritons (from Pt(p,d) and (p,t) reactions) appear at another position in the focal plane.

C. Dispersion Matching

The high-resolution data are obtained by using dispersion matching and kinematic compensation at the focal plane. The dispersion matching is achieved by adjusting the dispersion of energies in the beam to match the dispersion properties of the spectrograph. The energy spread must be coherent so that particles of energy $E + \Delta E$ go to one side on the target, and particles with energy $E - \Delta E$ go to the other side of the center, with intermediate energy particles in between these extremes. The dispersion of the spectrograph then focuses particle groups with the energy spread $\pm \Delta E$ at the detector. The kinematic compensation corrects for the differing energies of particles across the aperture due to recoil of the target nucleus. This is done by moving the detector within the reaction plane.

Experimentally this condition is achieved via a "tuning" procedure involving the beam transport elements, a small tuning counter in the focal plane, and a computer feedback sytem controlling the spectrograph magnetic field. The tuning is accomplished by adjusting the transport elements and focal plane positions to minimize the line width of elastically scattered protons from a thin target (usually 50 $\mu g/cm^2$ Au foil). A 1 cm delay-line counter [RCMe], backed by a solid state counter, was employed. The computer feedback system is necessary to keep the elastic line on the detector. With the particles incident on the counter at 90°

(versus the normal running mode of 45^{o}), line widths of 70 μm have been obtained.

D. Particle Detection

Two types of particle detection were used in these experiments. The highest resolution data were taken with Kodak NTB 25 μ nuclear emulsion plates. For the (p,p') data, a 15 mil stainless steel absorber was placed in front of the plates to lower the energy and thus increase the ionization of the protons. The resolution achieved for the plate data ranged from 5 to 10 keV FWHM. Figures IV–3 and IV–4 show sample spectra for both types of reactions. Although plates do provide the maximum resolution and do not require an elaborate electronics setup, there are still drawbacks in measuring a complete angular distribution for a series of reactions. The data from plates are obtained by visually scanning the plates for individual tracks with an off-line microscope. This is a very time-consuming process, which, for high track density plates, may require several months to complete a scan for one angular distribution. For the six reactions in this study, the plates were used primarily for calibration purposes by taking a spectrum at two or three angles to insure that no peaks in the spectrum were obscured by impurity lines. However, in the (p,t) reactions, plate data were taken at the first and second maxima and the first minimum of an L = 0 transition as an aid in searching for weaker or unknown L = 0 transitions.

Figure IV-3. Triton Spectra Recorded at 7^{o} for the $^{194,196,198}Pt(p,t)^{192,194,196}Pt$ Reactions. The data were obtained with nuclear emulsion plates in the focal plane of an Enge split-pole spectrograph. Peaks with an "*" above them indicate peak height has been cut off at the maximum value on the vertical axis.

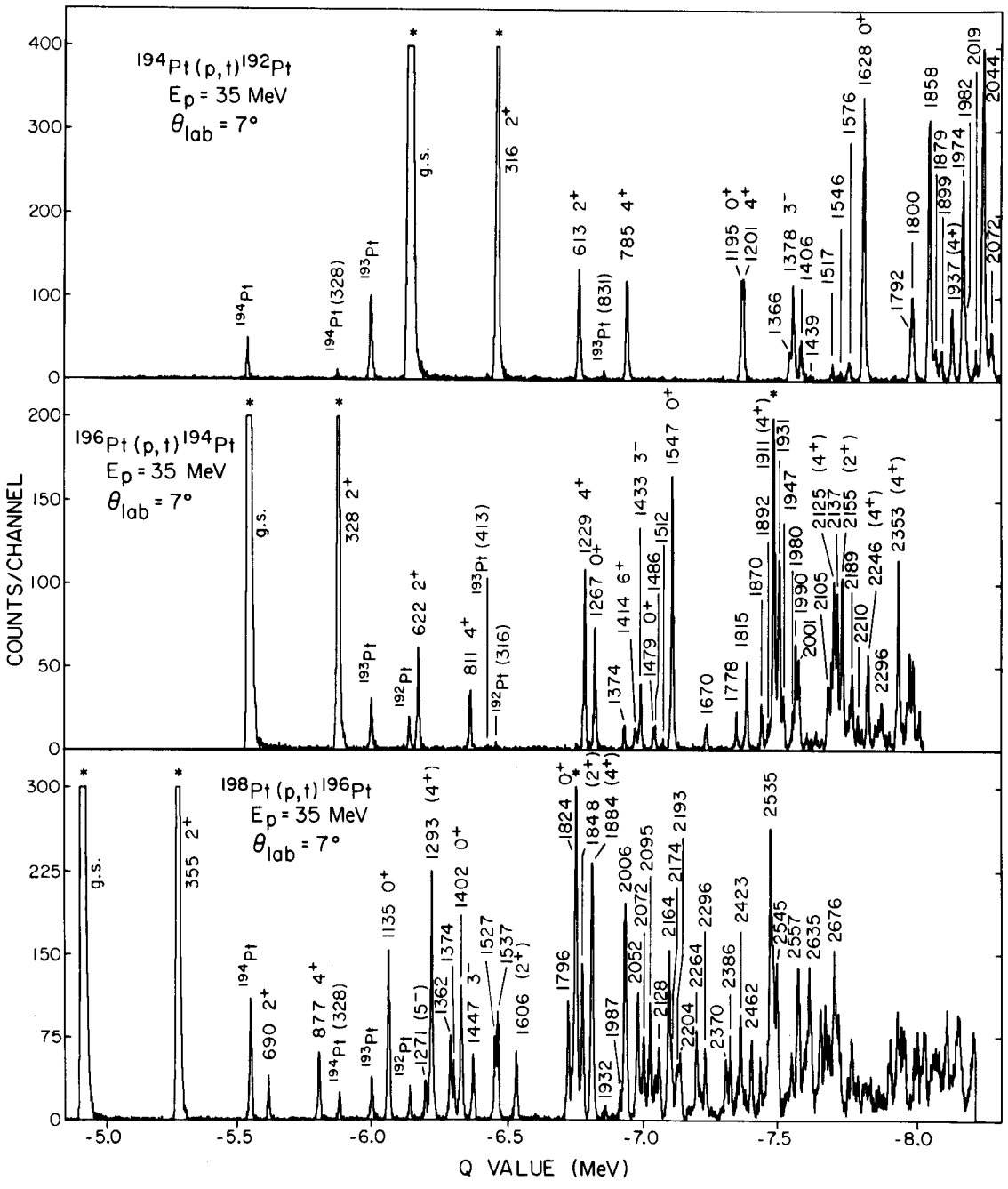
194Pt (p,t)192Pt
Ep = 35 MeV
θlab = 7°
196Pt (p,t)194Pt
Ep = 35 MeV
θlab = 7°
198Pt (p,t)196Pt
Ep = 35 MeV
θlab = 7°
COUNTS/CHANNEL
Q VALUE (MeV)
-5.0
-5.5
-6.0
-6.5
-7.0
-7.5
-8.0
g.s.
316 2+
613 2+
785 4+
1195 0+
1201 4+
1628 0+
328 2+
622 2+
811 4+
1229 0+
1267 0+
1414 6+
1433 3-
1547 0+
355 2+
690 2+
877 4+
1135 0+
1293 (4+)
1402 0+
1824 0+
1848 (2+)
1884 (4+)
2353 (4+)

Figure IV-3.

Figure IV-4. Inelastic Proton Spectra for the ^{194,196,198}Pt(p,p') Reactions at E_p = 35 MeV. The data were obtained with nuclear emulsion plates in the focal plane of an Enge split-pole spectrograph. The elastic scattering peaks are not shown because they were too intense to scan. Peaks with an "*" above them indicate peak height has been cut off at the maximum value on the vertical axis or were unscannable.

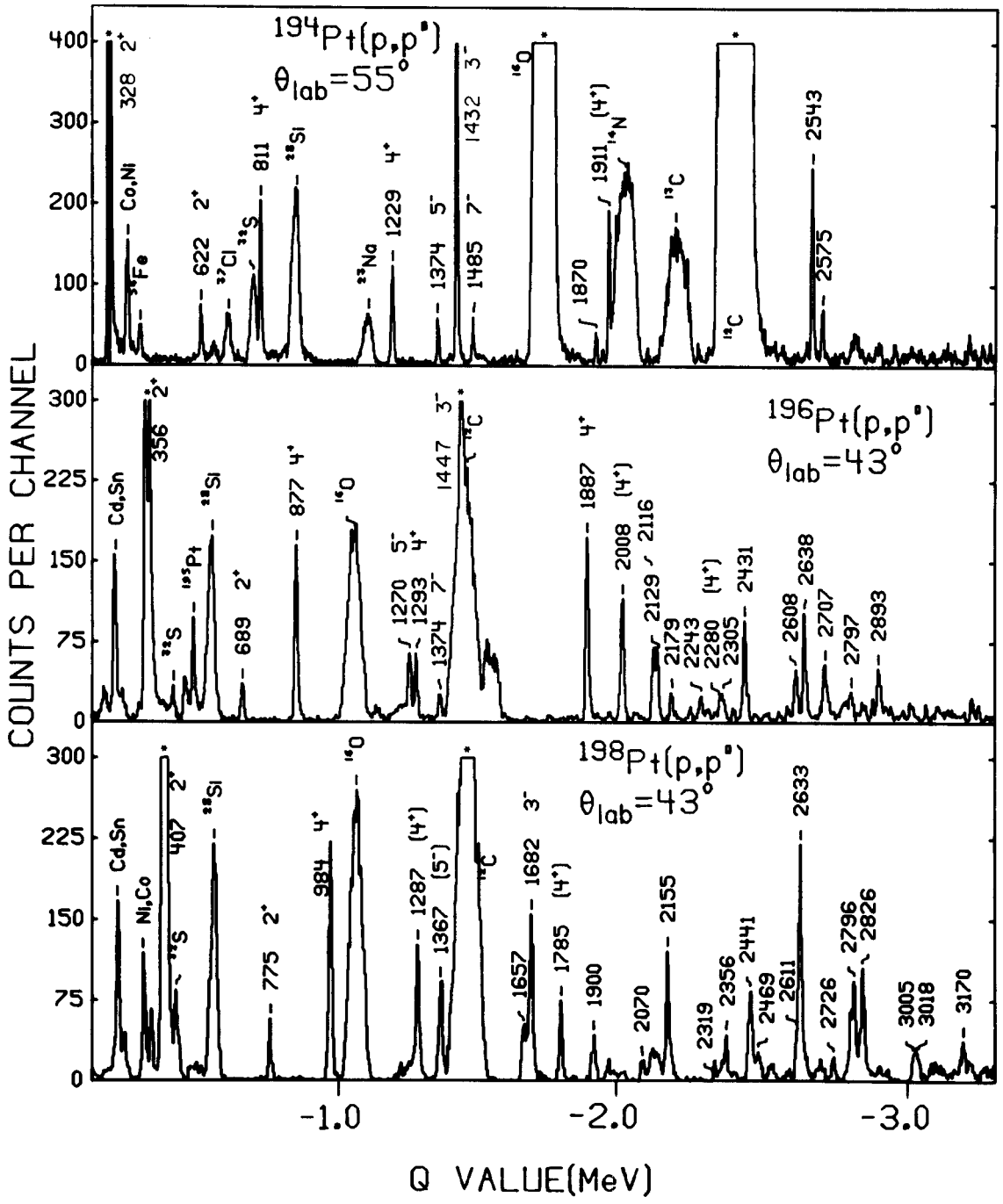
194Pt(p,p')
θlab=55°
196Pt(p,p')
θlab=43°
198Pt(p,p')
θlab=43°
COUNTS PER CHANNEL
Q VALUE(MeV)
-1.0
-2.0
-3.0
Cd,Sn
Co,Ni
Ni,Co
328 2+
622 2+
811 4+
1229 4+
1374 5-
1485 7-
1432 3-
1870
1911 (4+)
2543
2575
356 2+
689 2+
877 4+
1270 5-
1293 4+
1374 7-
1447 3-
1887 4+
2008 (4+)
2116
2129
2179
2243
2280 (4+)
2305
2431
2608
2638
2707
2797
2893
407 2+
775 2+
984 4+
1287 (4+)
1367 (5-)
1657
1682 3-
1785 (4+)
1900
2070
2155
2319
2356
2441
2469
2611
2633
2726
2796
2826
3005
3018
3170

Figure IV-4.

Most of the data for each of the six reactions were taken with a high-resolution, slanted cathode, position-sensitive delay line counter [Ma 75]. Figures IV–5 and IV–6 show a cross sectional view of the entire counter and a top view of the forward chamber (delay-line). A block diagram of the electronics used in processing all the signals in the wire counter experiments is shown in Figure IV–7. As particles enter the counter, the ionizations they produce are multiplied by the anode wires in the front counter. Only the center five anode wires are biased for amplification, while the two outer wires on each side are for field shaping. Thus, ionizations originating anywhere in the active region produce multiplication only on the wire directly above or below. The reason for effectively dividing the counter into five thin counters is to define the path of the particle more precisely. A charge is then induced on the slanted cathode, pickup board below the wires by the ionization. This induced charge is passed through a delay line, in which the signal from one end is used to start a time-to-amplitude converter (TAC), while the other end is delayed and used to stop the TAC. The height of the resulting output pulse is proportional to the position along the counter. Immediately behind the position counter is a single wire proportional counter. This is operated in an energy-loss (ΔE) mode which is used to identify different particles, since energy-loss through a medium is proportional to the charge (Z), mass (m), and energy (E) of the particle, $\Delta E \propto \frac{mZ^2}{E}$.

Figure IV-5. Schematic Cross Section of Delay-Line Counter. The labeled parts are: (A) window frames, (B) anode support, (C) separator foil frame, (D) anode wires, (E) ΔE anode wire, (F) pickup board, (G) frame for the delay line and board, and (H) delay-line. Taken from Reference [Ma 75].

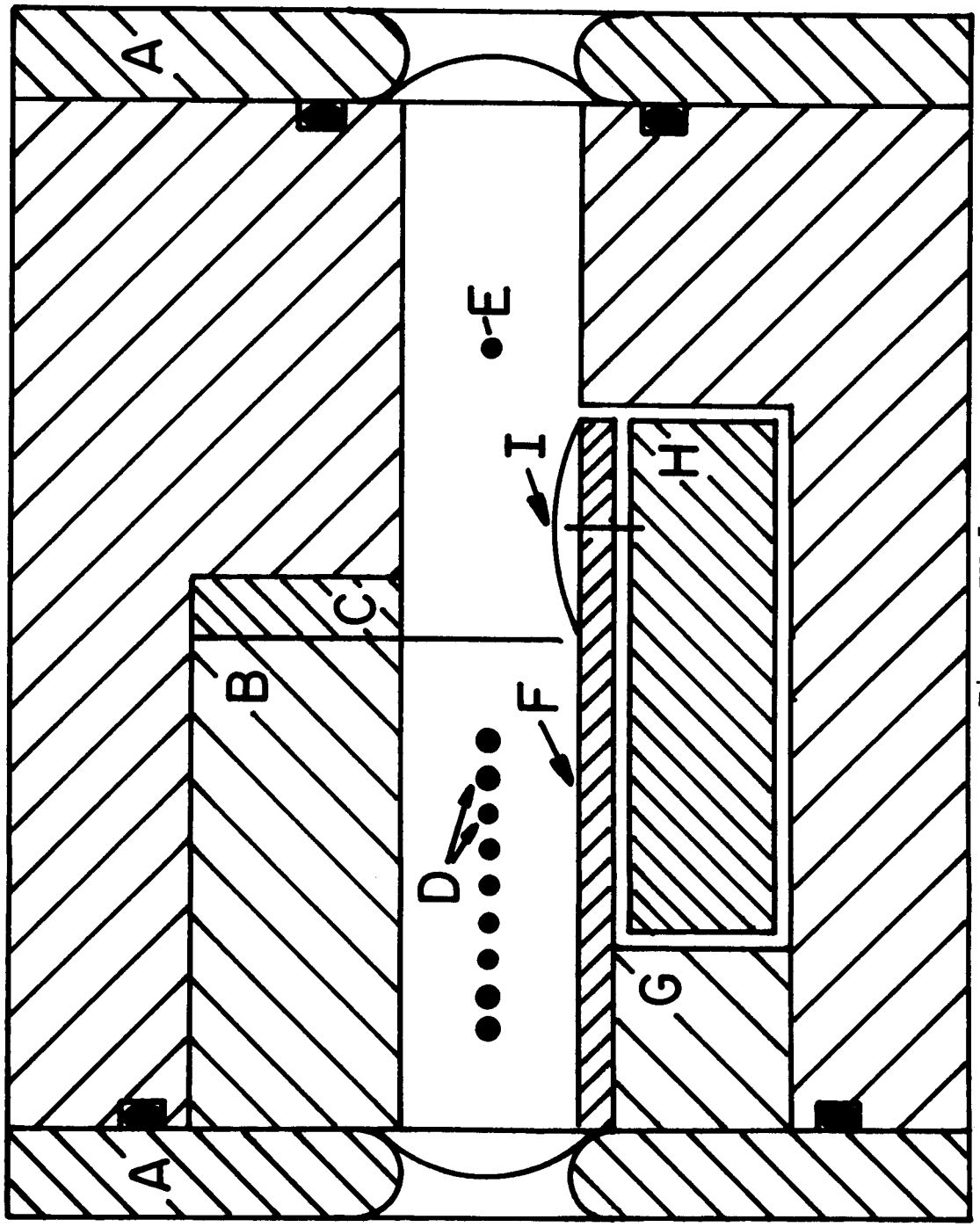

Figure IV-5.

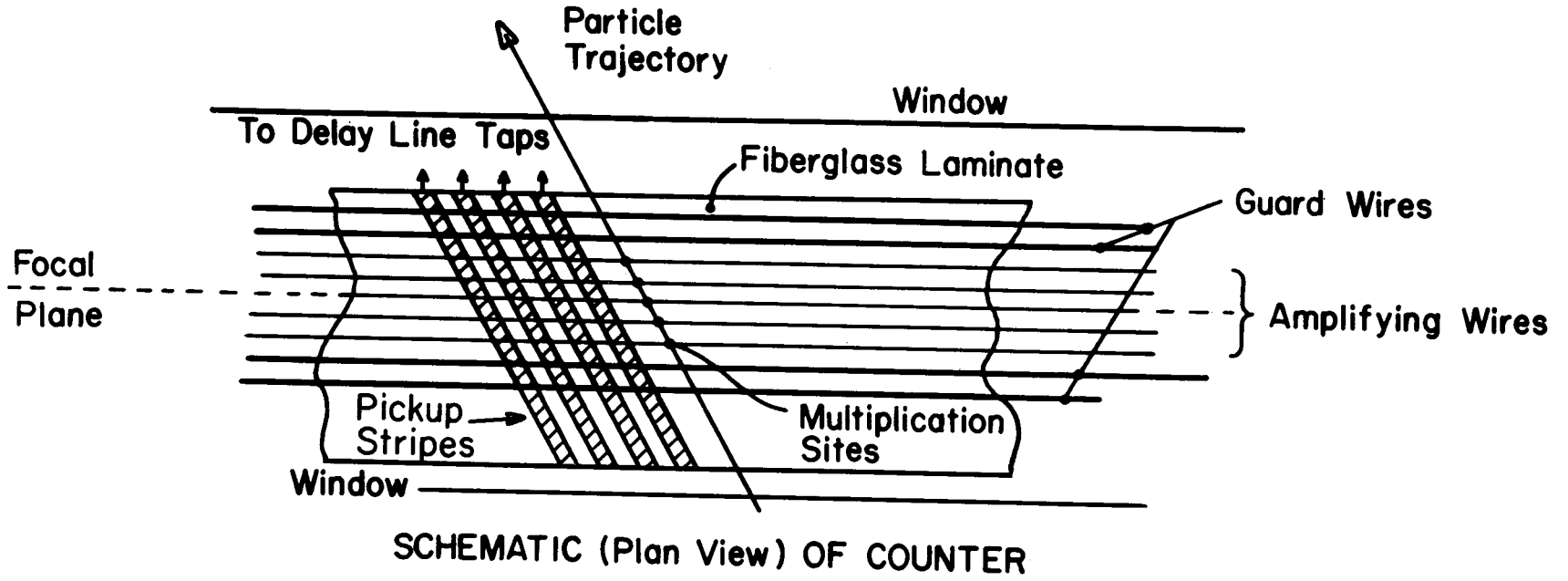

Figure IV-6. Schematic Top View of Delay-Line Counter. Taken from Reference [Ma 75].

Figure IV-7. Schematic Diagram of Electronics for Wire Counter Experiments.

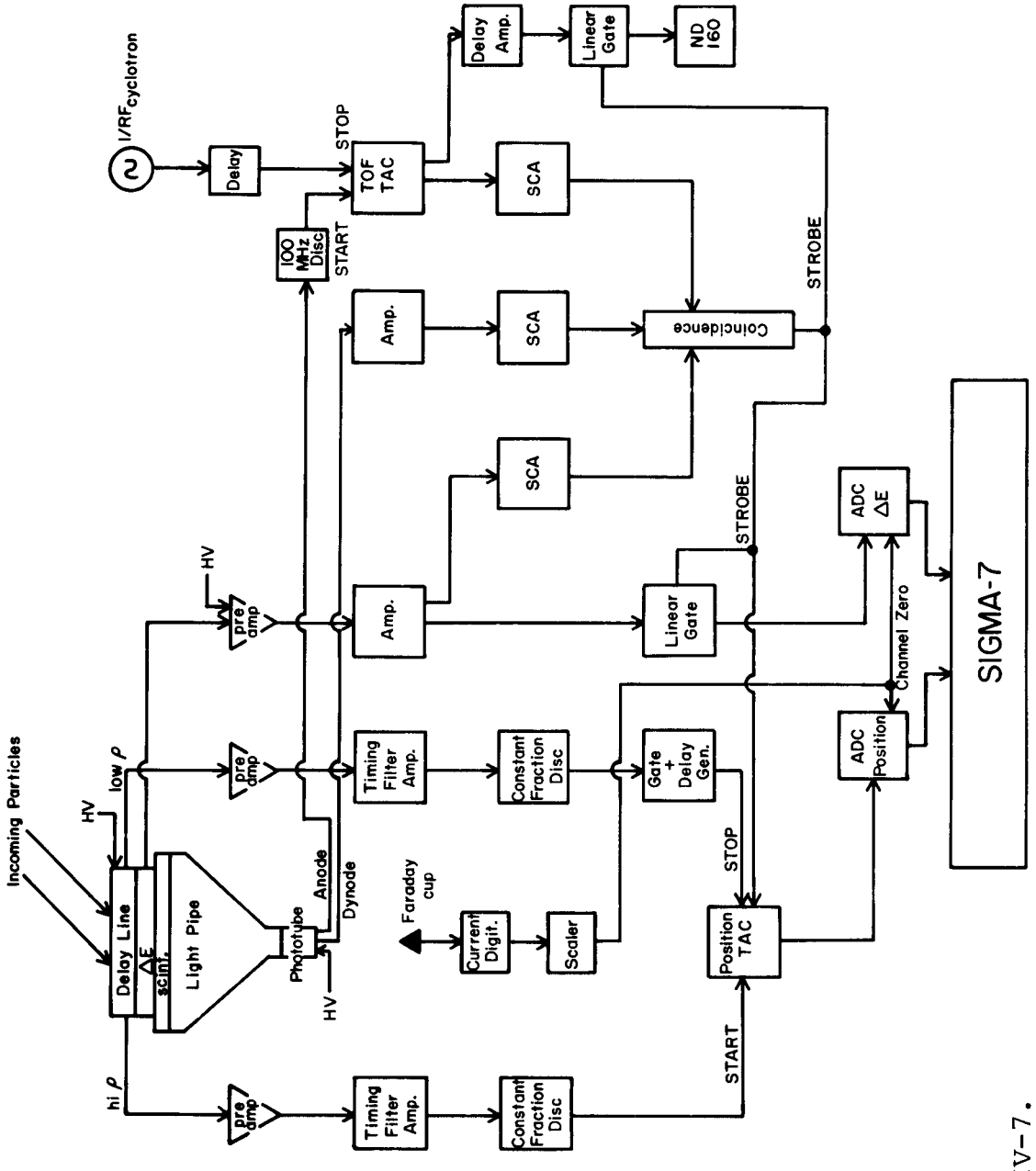
1/RF cyclotron
Delay
STOP
TOF TAC
Delay Amp.
Linear Gate
ND 160
SCA
100 MHz Disc.
START
Amp.
SCA
Coincidence
STROBE
SCA
HV
pre amp
Amp.
Linear Gate
STROBE
ADC ΔE
Channel Zero
SIGMA-7
Incoming Particles
low ρ
HV
pre amp
Timing Filter Amp.
Constant Fraction Disc
Gate + Delay Gen.
ADC Position
Delay Line
ΔE scint.
Light Pipe
Anode
Dynode
Phototube
HV
Faraday cup
Current Digit.
Scaler
STOP
Position TAC
hi ρ
pre amp
Timing Filter Amp.
Constant Fraction Disc
START

Figure IV-7.

This system is then backed by a plastic scintillator with a light pipe and photomultiplier. The anode signal from the scintillator is used to start another TAC which is stopped by the cyclotron rf. This gives redundant particle information via the time-of-flight (TOF) of the particles. The dynode signal is also used to identify the energy of the particle. Note in Figure IV–7 that the only signals sent to the computer for processing are the ΔE signal and the position information. The energy, TOF, and ΔE are used to provide a coincidence requirement and provide a strobe to the position TAC and ΔE linear gate. Thus, unnecessary signals from unwanted particle groups have been electronically gated and are not processed by the computer. Figures IV–8 and IV–9 show sample spectra taken with the wire counter setup for each reaction studied. The resolution for the triton spectra was typically ≃ 15–20 keV FWHM and for the proton spectra was 18–25 keV FWHM.

E. Targets

Two types of targets (for properties see Table IV–1) were used for this study. In the wire counter experiments rolled-foil Pt targets with a thickness of approximately 625 $\mu g/cm^2$ were used [FKar]. For the data taken with photographic plates, thinner targets were needed to minimize resolution degradation due to straggling and energy loss in the targets. For the 600 $\mu g/cm^2$ targets the energy loss and

Figure IV-8. Triton Spectra for the ^{194,196,198}Pt(p,t) Reactions at E_p = 35 MeV. The data were obtained with a delay-line proportional wire counter in the focal plane of an Enge split-pole spectrograph.

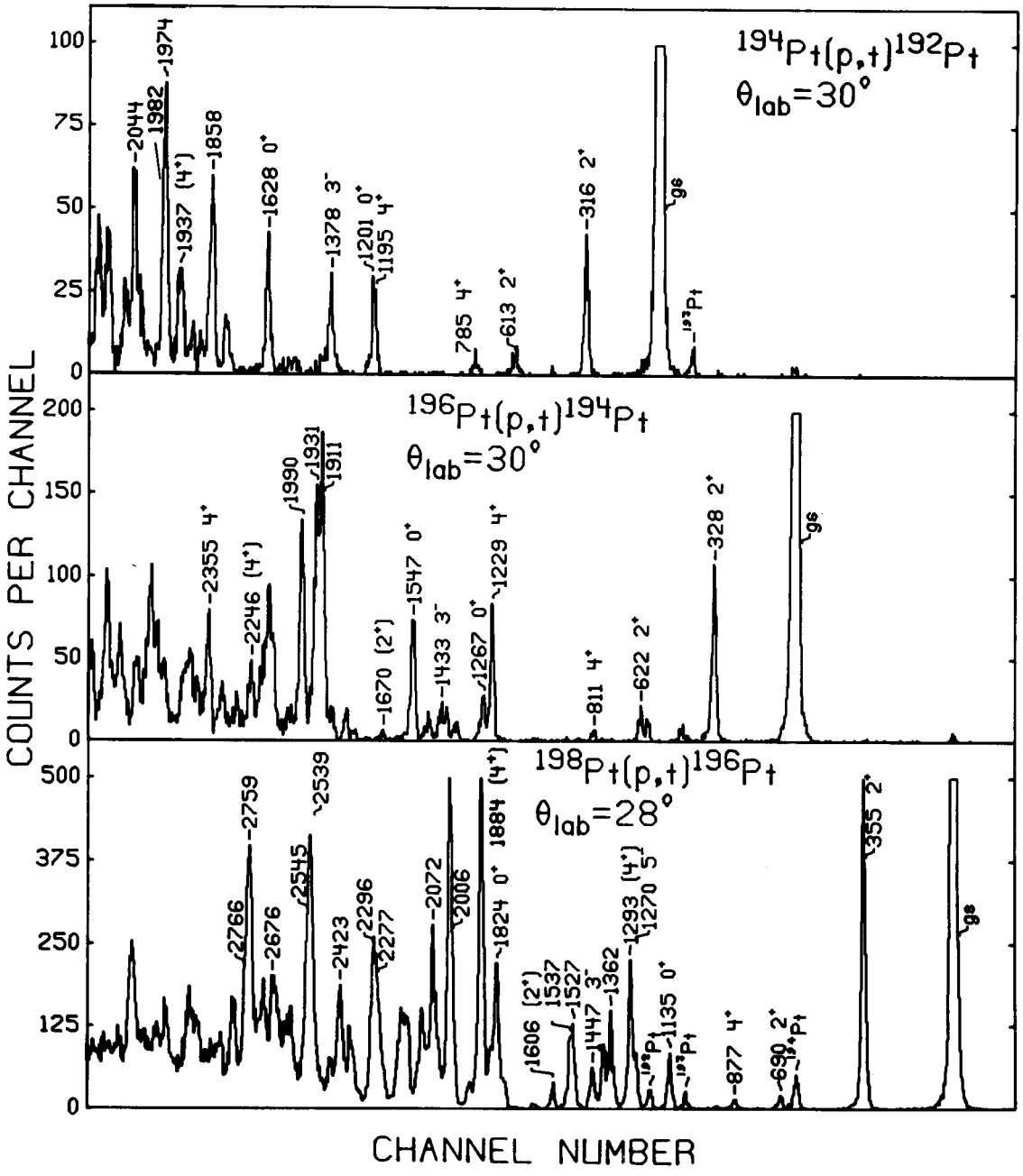
^{194}Pt(p,t)^{192}Pt
θ_{lab}=30°
^{196}Pt(p,t)^{194}Pt
θ_{lab}=30°
^{198}Pt(p,t)^{196}Pt
θ_{lab}=28°
COUNTS PER CHANNEL
CHANNEL NUMBER

Figure IV-8.

Figure IV-9. Sample Spectra for the ^{194,196,198}Pt(p,p') Reactions at 85°. The data were obtained with a delay-line proportional wire counter in the focal plane of an Enge split-pole spectrograph.

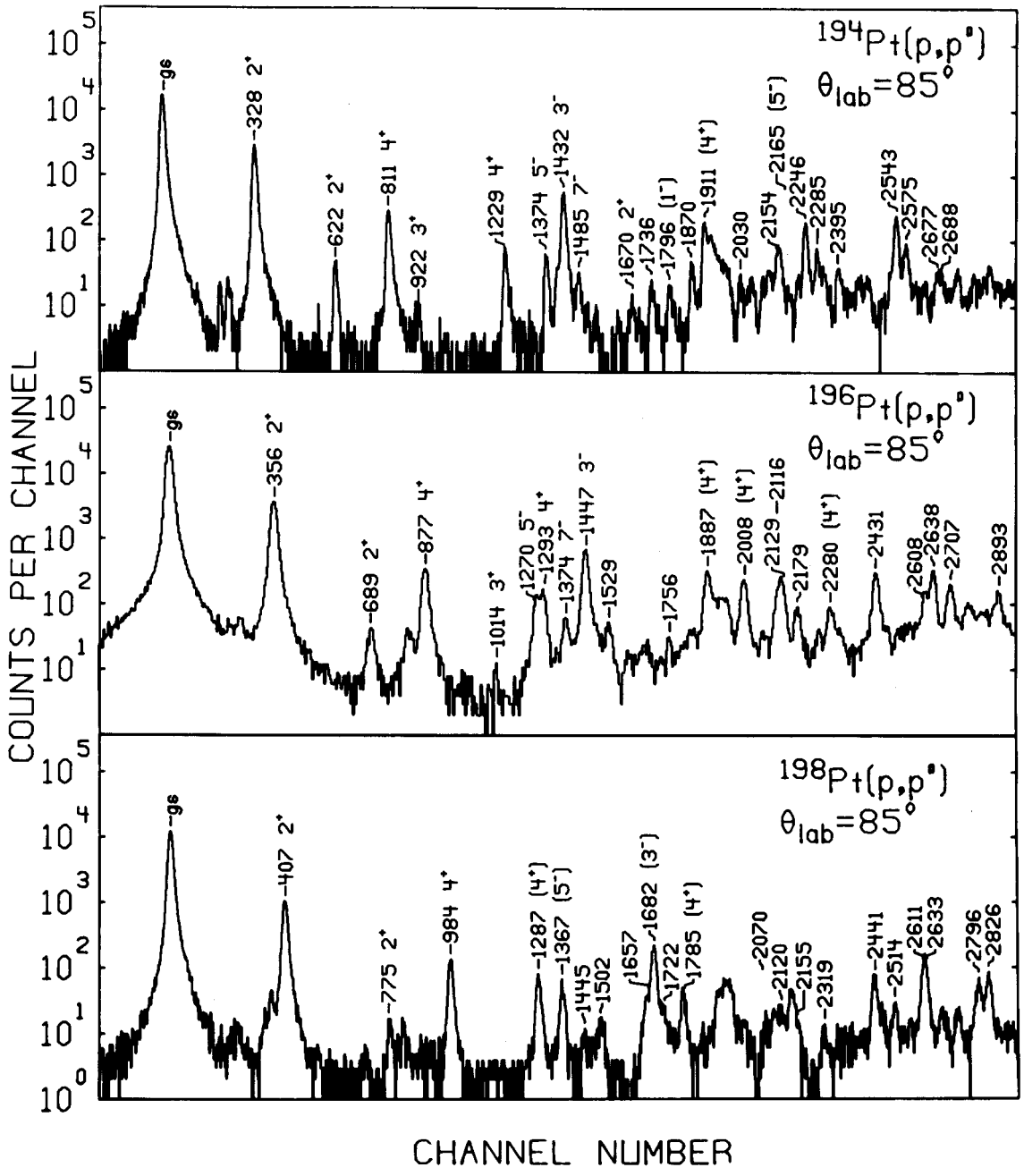
194Pt(p,p')
θlab=85°
gs
328 2+
622 2+
811 4+
922 3+
1229 4+
1374 5-
1432 3-
1485 7-
1670 2+
1736
1796 (1-)
1870
1911 (4+)
2030
2154
2165 (5-)
2246
2285
2395
2543
2575
2677
2688
196Pt(p,p')
θlab=85°
gs
356 2+
689 2+
877 4+
1014 3-
1270 5-
1293 4+
1374 7-
1447 3-
1529
1756
1887 (4+)
2008 (4+)
2129
2116
2179
2280 (4+)
2431
2608
2638
2707
2893
198Pt(p,p')
θlab=85°
gs
407 2+
775 2+
984 4+
1287 (4+)
1367 (5-)
1445
1502
1657
1682 (3-)
1722
1785 (4+)
2070
2120
2155
2319
2441
2514
2611
2633
2796
2826
COUNTS PER CHANNEL
CHANNEL NUMBER

Figure IV-9.

Table IV-1. Target Composition.

Target	Q-Value[a] (MeV)	Isotopic Abundance[b] (%)						Target Thickness ($\mu g/cm^2$)	
		^{190}Pt	^{192}Pt	^{194}Pt	^{195}Pt	^{196}Pt	^{198}Pt	Foils	Sputtered[c]
^{194}Pt	-6.23	0.01	0.015	97.41	1.99	0.52	0.06	630	110
^{196}Pt	-5.57	0.01	0.01	0.63	1.57	97.51	0.29	650	190
^{198}Pt	-4.85	0.01	0.01	0.79	1.18	2.18	95.83	675	175

[a] Reference [Ga 69].
[b] Analysis furnished by Oak Ridge National Laboratory.
[c] A 20 $\mu g/cm^2$ carbon foil was used as a backing.

straggling particles contribute about 4–5 keV to the resolution, while the thinner, sputtered targets cause a 1–2 keV contribution. So for the wire counter the thick targets sufficed, but for plates, thinner targets were necessary. Targets [No 78] were made for this purpose by sputtering Pt metal onto a backing resulting in thicknesses of $\simeq$ 200 $\mu g/cm^2$. The platinum used in each target was isotopically enriched to near 97%. This provided very clean targets for the foils but the sputtering process introduced several impurities (Sn, Ni, Fe, Cl, Na, Si) which limited the usefulness of the plate data for the (p,p') reactions. For the (p,t) plate data, however, the large negative Q–values allowed for very clean spectra.

F. Data Analysis

Peak areas and centroids were determined with two computer codes, AUTOFIT [JRCo] and SCOPEFIT [HDav]. Each program uses an empirical reference peak shape (usually derived from the ground state), with a user-supplied background to unfold the peaks of interest. The energy calibration was performed for each reaction by two methods, both using six or seven known excitation energies for platinum levels as given in Nuclear Data Sheets. The first method involved fitting a second-order polynomial to the levels and the second method used a kinematic routine to map out momentum versus distance along the focal plane for the

MSU spectrograph. Both methods generally agreed within 0.2% in the energies up to 3.0 MeV in excitation. Since only one excited level is known with any accuracy in ^{198}Pt, a separate calibration experiment was performed to obtain energy information in this case. Plate data were taken at 75^{o} and 43^{o} for the ^{196,198}Pt(p,p') and ^{206}Pb(p,p') reactions. Spectra from all three reactions were recorded on one plate at each angle. Only the height of the plates was adjusted for each reaction, not their positions, thus assuring an accurate relative calibration. These two angles were chosen for minimum interference from the silicon, carbon, and oxygen impurity peaks. ^{196}Pt was used because of the well-known low-lying levels, while ^{206}Pb was chosen because of the strongly excited 3^{-} level at 2.648 MeV. The known levels in ^{196}Pt and Pb then provided the necessary calibration lines to bracket the ^{198}Pt levels of interest. Due to energy losses from the different target thicknesses, the absolute energies of ^{196}Pt and ^{206}Pb cannot be used for calibration, so a value for the gain (keV per channel) was obtained for each spectrum, which was then used to calibrate the ^{198}Pt(p,p') data. The gain should be the same for each reaction since these were recorded consecutively on the same plate. The uncertainty in the excitation energies is approximately 1 keV below 1.5 MeV and 0.1% above 1.5 MeV.

Cross sections were calculated from the equation

$$d\sigma/d\Omega_{lab} \text{ (mb/sr)} = \frac{2.67\ A\ Y_{o} Z}{t\Omega Q} ,$$

with

Z = charge of projectile

A = mass number of target

Y_o = number of counts in peak (area)

t = target thickness (in $\mu g/cm^2$)

Ω = solid angle (in 10^{-4} steradians)

Q = collected charge (in μ Coulombs).

A conversion to center of mass angle and cross section was also performed. The experimental data were normalized to the integrated beam current measured in a Faraday cup and compared to elastically scattered protons monitored at 90^o to the beam. Disagreement between charge and monitor counter normalization was generally less than 5% for the rolled foil targets. Absolute cross sections for all targets were obtained in a separate set of experiments by normalizing the angular distribution of elastically scattered 35 MeV protons to optical model predictions between 25^o and 50^o. The normalizations for the (p,p') reactions were determined in a similar manner with the code ECIS [Ra 73], to be discussed in Section VII. The absolute uncertainties are on the order of 15–20% due to target thickness and aperture size uncertainties. The optical model calculations were performed with the Becchetti-Greenlees [Be 69] proton parameters given in Table III–1.

A correction to the peak areas was necessary for the ^{194,198}Pt(p,p') data due to a different configuration of the

electronics. In this mode the position information was taken versus the front counter ΔE signal, taken from the high ρ end of the delay line rather than the ΔE signal from the back counter. The ΔE signal from the back counter was still used in the coincidence requirement part of the electronics. This was done to control the long tails seen on the intense elastic peak, which may obscure weakly excited states nearby. These tails are caused partially by slit scattering in the beam transport system, but mainly by the production of delta rays (high energy electrons) along the wires of the delay line. By displaying position versus the ΔE of the front wires (where the delta rays are produced), one may set a gate with the computer and collect two spectra, a "wing" band and a "data" band. An example is shown in Figure IV-10. The bands were set such that less than 10% of the total yield was placed in the wing band. The correction factor for total peak area was obtained from the ratio of total counts in the wing band plus total counts in data band divided by counts in the data band. In ^{198}Pt data was taken in both modes at three angles and the cross sections differed by only 2 to 4%, well within experimental uncertainties.

Figure IV-10. Comparison of Wing Band and Data Band Spectra Taken With the Delay-Line Proportional Wire Counter. The ratio of counts in the wing band to counts in the data band is 1:10.

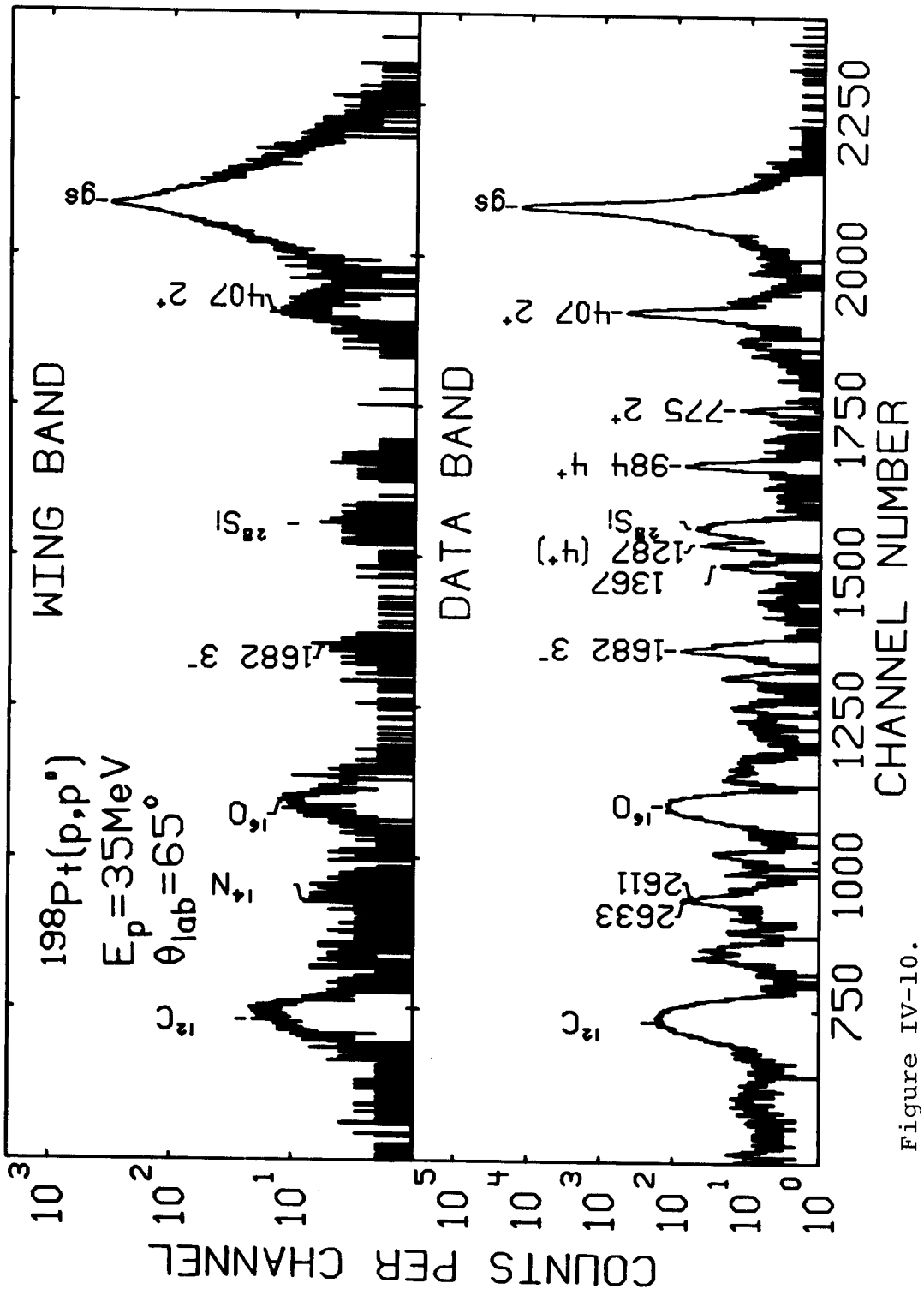
198Pt(p,p')
Ep=35MeV
θlab=65°
WING BAND
DATA BAND
12C
14N
16O
1682 3-
28Si
1407 2+
gs
1367
1287 (4+)
984 4+
775 2+
2633
2611
COUNTS PER CHANNEL
CHANNEL NUMBER
750
1000
1250
1500
1750
2000
2250

Figure IV-10.

CHAPTER V

RESULTS FOR THE ^{194,196,198}Pt(p,t) REACTIONS

A. General Analysis

Tables V–1, V–2, and V–3 contain the excitation energies, cross sections, and assignments of J^{π} for the three (p,t) reactions studied, ^{194,196,198}Pt(p,t), in addition to results from previous works. Tables V–2 and V–3 also include the results of the (p,p') study of ^{194,196}Pt. The cross sections reported are for the (p,t) data taken at 7^{o} using nuclear emulsions, as the resolution ($\simeq$ 7 keV FWHM) and low background allowed the observation for weakly excited and close lying states. The energies and cross sections are obtained for approximately 50 levels in the ^{196,198}Pt(p,t)^{194,196}Pt reactions and 64 in the ^{194}Pt(p,t)^{192}Pt reaction, with about one-half of the levels in each case being seen for the first time. Values for the enhancements factors, ε, (defined in Section V–2) are listed for those states where relatively complete angular distributions were obtained. Because simplified reaction couplings were used in analyzing the (p,t) data, unambiguous spin and parity assignments can be made when an experimental angular

Table V-1. States Populated in the $^{194}Pt(p,t)^{192}$ Reaction.

Present Experiment $^{194}Pt(p,t)^{192}Pt$				Previous Results[a]	
E_x (MeV)	J^π	$\sigma(7^o)$ (μb/sr)	ϵ[b]	E_x[c] (MeV)	J^π
0.0	0^+	971	5.1	0.0	0^+
0.316[d]	2^+	126	0.84	0.3165	2^+
0.613[d]	2^+	16	0.16	0.6124	2^+
0.785[d]	4^+	15	0.21	0.7845	4^+
1.195[d]	0^+	10	0.07	1.1951	0^+
1.201[d]	4^+	16		1.2010	4^+
1.366		4		1.3653	6^+
1.378[d]	3^-	16		1.3779	3^-
1.406		7		1.4062	
1.439		1		1.4391	$(1^+,2^+)$
1.517		2		1.5182	7^-
1.546		1			
1.576		4		1.5766	(2^+)
1.628	0^+	49	0.26		
1.792		6			
1.800		23 (10^o)			
1.858		43			
1.879		5		1.8804	
1.899		4			
1.937	(4^+)	11	0.32		
1.974		28			
1.982		9			
2.019 (3)		3			8^+
2.044	(doublet)	70		2.0479	
2.072		7		2.0741	

Table V-1 (cont'd.).

Present Experiment $^{194}Pt(p,t)^{192}Pt$				Previous Results[a]	
E_x (MeV)	J^π	$\sigma(7^o)$ (μb/sr)	ε[b]	E_x[c] (MeV)	J^π
2.132		7		2.1301	
2.140		13			
2.153		8		2.1494	
2.166		19			
2.188		7			
2.204		17			
2.271		18			
2.308		25			
2.330	(3)	1		2.3356	
2.352		4			
2.358		7			
2.375		2		2.3755	
2.389		2			
2.411		6		2.4085	
2.428		15			
2.444		11			
2.450		9		2.4533	
2.467		13		2.4722	
2.486		6			
2.492		8			
2.506		1			
2.526		6			
2.549		21			
2.556		11			
2.575		4			

Table V-1 (cont'd.).

Present Experiment $^{194}Pt(p,t)^{192}Pt$				Previous Results[a]	
E_x (MeV)	J^π	$\sigma(7^o)$ (μb/sr)	ε[b]	E_x[c] (MeV)	J^π
2.588		6		2.5853	
2.605		7			
2.624		6			
2.646		18			
2.662		5			
2.671		3			
2.695		4			
2.704		6			
2.720		7			
2.729		10			
2.743		6			
2.754		6			
2.778		5			
2.786		4			

[a] References [Ny 66, Be 70, Ya 74, Hj 76, Ro 77, Sa 77, Ba 78].

[b] The enhancement factors were calculated with pickup configurations $(0p_{3/2})$ for L = 0, $(2p_{3/2} \otimes 1f_{7/2})$ for L = 2, and $(1f_{5/2} \otimes 2p_{3/2})$ for L = 4.

[c] The states above 2 MeV seen in this work and previous results are associated only because of similar energies.

[d] Used as calibration point with energy taken from Nuclear Data Sheets B9, 195 (1973). Uncertainties in excitation energy are approximately 1 keV below 1.4 MeV and 0.1% above 1.4 MeV, except as indicated.

Table V-2. States Populated in the $^{196}Pt(p,t)^{194}Pt$ and $^{194}Pt(p,p')$ Reactions.

Present Experiments							Previous Results[a]	
$^{196}Pt(p,t)^{194}Pt$				$^{194}Pt(p,p')$				
E_x (MeV)	J^π	$\sigma(7^o)$ (μb/sr)	ε[b]	E_x (MeV)	J^π	$\sigma(30^o)$ (μb/sr)	E_x[c] (MeV)	J^π
0.0	0^+	801	3.6	0.0	0^+	5.00×10^5	0.0	0^+
0.328[d]	2^+	159	1.3	0.328	2^+	5.03×10^3	0.3285	2^+
0.622[d]	2^+	18	0.16	0.622[e]	2^+	167	0.6221	2^+
0.811[d]	4^+	9	0.10	0.811[e]	4^+	328(40^o)	0.8112	4^+
				0.922(2)	(3^+)	26.6	0.9228	3^+
1.229[d]	4^+	30	0.63	1.229[e]	4^+	158	1.2295	4^+
1.267[d]	0^+	20	0.08				1.2671	0^+
1.374	$(4^+,5^-)$	4	0.26	1.374[e]	5^-	77.5	1.3734	(5^-)
1.414(2)	6^+	5	0.10	1.412	6^+	36.1	1.4116	6^+
1.433[d]	3^-	12	1.3	1.432[e]	3^-	1.34×10^3	1.4325	3^-
1.479(2)	0^+	3	0.03				1.4792	0^+
1.486(2)		3		1.485[e]	7^-	66.5	1.4853	7^-
1.512(3)		2		1.511(3)			1.5119	2^+
				1.529(2)				

Table V-2 (cont'd.).

Present Experiments							Previous Results[a]	
$^{196}Pt(p,t)^{194}Pt$				$^{194}Pt(p,p')$				
E_x (MeV)	J^π	$\sigma(7^o)$ (μb/sr)	ε[b]	E_x (MeV)	J^π	$\sigma(30^o)$ (μb/sr)	E_x[c] (MeV)	J^π
1.547[d]	0^+	46	0.26	1.547			1.5472	0^+
1.670		5		1.670	(2^+)	11.0(40^o)	1.6706	2^+
				1.736		28.3		
1.778		6					1.7787	$(1,2,3)^+$
				1.796		38.6	1.7974	1^-
1.815		14		1.815		14.8	1.817	(3^-)
				1.870		123		
1.892		5		1.892			1.8936	0^+
1.911	(4^+)	71	1.9	1.911[e]	(4^+)	457		
1.931		42		1.932	(5^-)	141	1.9302	$(1,2,3)^+$
1.947		10		1.948(3)		37.6	1.9485	
				1.974				
				1.981		22.1		
1.990	$(6^+,7^-)$	9	(0.91,3.6)				1.9917	
2.001		17					1.9999	(8^-)

Table V-2 (cont'd.).

Present Experiments							Previous Results[a]	
$^{196}Pt(p,t)^{194}Pt$				$^{194}Pt(p,p')$				
E_x (MeV)	J^π	$\sigma(7^o)$ (μb/sr)	ε[b]	E_x (MeV)	J^π	$\sigma(30^o)$ (μb/sr)	E_x[c] (MeV)	J^π
2.031		3		2.030		33.5	2.03	
2.062		4					2.0638	(2^+)
				2.072		120		
2.105		16		2.104		37.0		
2.125	(4^+)	37	0.57	2.126	(4^+)	105	2.13	
2.137		30						
2.155	(2^+)	38	0.27	2.154		145	2.158	$(1,2)^+$
				2.165	(5^-)	90.5		
2.189		18		2.192(4)		16.0		
2.210		6						
2.224		4		2.222		41.0	2.22	
2.246	(4^+)	18	0.43	2.246		485		
2.277		6						
2.284		6		2.285		168	2.287	$(1,2)^+$
2.296	$(7^-,8^+)$	10					2.2961	1^+
				2.309		30.7	2.3098	

Table V-2 (cont'd.).

Present Experiments							Previous Results[a]	
$^{196}Pt(p,t)^{194}Pt$				$^{194}Pt(p,p')$				
E_x (MeV)	J^π	$\sigma(7^\circ)$ (μb/sr)	ε^b	E_x (MeV)	J^π	$\sigma(30^\circ)$ (μb/sr)	E_x^c (MeV)	J^π
				2.323(4)				
2.353	(4^+)	37	0.87	2.354		93.6		
				2.370(4)		29.1		
				2.395		15.2	2.3975	
				2.404		19.6(40°)		
				2.418(4)		12.2		
				2.526		90.8		
2.532	(2^+)	28	0.33					
				2.543		609		
2.566	(6^+)	11(10°)	0.56			}	2.56	
2.580		27		2.575		154		
				2.586(5)				
2.595		16						
2.638	(4^+)	29	0.61					
				2.677				
				2.688(5)				

Table V-2 (cont'd.).

Present Experiments							Previous Results[a]	
$^{196}Pt(p,t)^{194}Pt$				$^{194}Pt(p,p')$				
E_x (MeV)	J^π	$\sigma(7^o)$ (μb/sr)	ϵ[b]	E_x (MeV)	J^π	$\sigma(30^o)$ (μb/sr)	E_x[c] (MeV)	J^π
2.700	(6^+)	18	0.61	2.698			2.7003	(11^-)
2.757		30						
2.815		12						
2.840		7						
2.871		13						
2.895		7						

[a] References [Be 64, Ma 65, Su 68, Be 70, Ma 72, Ya 74, Ba 76, Cl 76, Hj 76, Le 77, Ro 77].

[b] The enhancement factors were calculated with pickup configurations $(0p_{3/2})^2$ for L = 0, $(2p_{3/2} \otimes 1f_{7/2})$ for L = 2, $(0i_{13/2} \otimes 1f_{7/2})$ for L = 3, $(1f_{5/2} \otimes 2p_{3/2})$ for L = 4, $(2p_{3/2} \otimes 0i_{13/2})$ for L = 5, $(1f_{5/2} \otimes 1f_{7/2})$ for L = 6, and $(2p_{1/2} \otimes 0i_{13/2})$ for L = 7.

[c] The states above 2 MeV seen in this work and previous results are associated only because of similar energies.

[d] Used as calibration point with energy taken from Nuclear Data Sheets B7, 95 (1972). Uncertainties in excitation energy are approximately 1 keV below 1.5 MeV and 0.1% above 1.5 MeV, except as indicated.

[e] Used as calibration point with energy taken from Nuclear Data Sheets B7, 95 (1972). Uncertainties in excitation energy are approximately 1 keV below 1.9 MeV and 0.1% above 1.9 MeV, except as indicated.

Table V-3. States Populated in the $^{198}Pt(p,t)^{196}Pt$ and $^{196}Pt(p,p')$ Reactions.

Present Experiments							Previous Results[a]	
$^{198}Pt(p,t)^{196}Pt$				$^{196}Pt(p,p')$				
E_x (MeV)	J^π	$\sigma(7^o)$ (μb/sr)	ε[b]	E_x (MeV)	J^π	$\sigma(30^o)$ (μb/sr)	E_x[c] (MeV)	J^π
0.0	0^+	852	3.7	0.0	0^+	5.69×10^5	0.0	0^+
0.356[d]	2^+	272	2.2	0.356	2^+	4.55×10^3	0.3557	2^+
0.689[d]	2^+	10	0.12	0.689[e]	2^+	$48.7(40^o)$	0.6889	2^+
0.877[d]	4^+	13	0.12	0.877[e]	4^+	258	0.8770	4^+
				1.014(2)	3^+	$9.88(45^o)$	1.0152	3^+
1.135[d]	0^+	29	0.11				1.1352	0^+
1.271[d]	5^-	7		1.270[e]	(5^-)	180	1.2705	$(4,5)^-$
1.293	(4^+)	43	0.77	1.293[e]	(4^+)	269		
1.362		8					1.3617	$(1^+,2^+)$
1.374	$(6^+,7^-)$	15	0.94	1.374[e]	7^-	104	1.374	$(6,7)^-$
1.402	0^+	22	0.15				1.4027	$0^+,1^+,2^+$
1.447[d]	3^-	13	0.81	1.447	3^-	1.08×10^3	1.4471	3^-
1.527		11		1.529		77.0		
1.537		17						
1.606	(2^+)	10	0.09	1.603(3)	2^+	29.8	1.6045	$0^+,1,2^+$

Table V-3 (cont'd.).

Present Experiments							Previous Results[a]	
$^{198}Pt(p,t)^{196}Pt$				$^{196}Pt(p,p')$				
E_x (MeV)	J^π	$\sigma(7^o)$ (μb/sr)	ε[b]	E_x (MeV)	J^π	$\sigma(30^o)$ (μb/sr)	E_x[c] (MeV)	J^π
1.675(3)		1		1.679(3)		32.9	1.677	2^+
				1.756(3)		37.7	1.7546	$3,4^\pm,5^-$
1.796		22						
1.824[d]	0^+	71	0.32	1.826(3)		67.8	1.8234	0^+
1.848	(2^+)	21	0.22				1.8471	$0^+,1,2$
1.884	(4^+)	116	2.1	1.887	4^+	536	1.88	
1.932		2						
				1.964(3)				
1.987		5						
2.006		45		2.008	(4^+)	295		
2.052		19		2.055(3)				
2.072		17						
2.095		20						
2.114		7		2.116		179		
2.128		12		2.129		291	2.1289	$1^-,2^+$

Table V-3 (cont'd.).

Present Experiments							Previous Results[a]	
$^{198}Pt(p,t)^{196}Pt$				$^{196}Pt(p,p')$				
E_x (MeV)	J^π	$\sigma(7^o)$ (μb/sr)	ε[b]	E_x (MeV)	J^π	$\sigma(30^o)$ (μb/sr)	E_x[c] (MeV)	J^π
2.164		28					2.1627	$0^+,1,2$
2.174		9		2.179			2.1744	2^+
2.193		9					2.1908	$0^+,1,2$
2.204		11					2.2044	2^+
				2.243		48.6	2.2455	$(1,2)^+$
2.264		16					2.2641	$1,2^+$
2.277		5		2.280	(4^+)	65.0		
2.296	$(7^-,8^+)$	12						
				2.305		50.0	2.3092	$(1,2)^+$
				2.331(4)				
				2.349			2.3453	$1^+,2^+$
				2.360				
2.370		10						
2.386		11						
				2.393			2.39	

Table V-3 (cont'd.).

Present Experiments							Previous Results[a]	
$^{198}Pt(p,t)^{196}Pt$				$^{196}Pt(p,p')$				
E_x (MeV)	J^π	$\sigma(7^o)$ (μb/sr)	ε^b	E_x (MeV)	J^π	$\sigma(30^o)$ (μb/sr)	$E_x{}^c$ (MeV)	J^π
2.423		21						
				2.431		541		
2.440		4					2.442	$0^+,2^+$
2.462		14					2.468	1^+
				2.469			2.4699	$(1,2)^+$
				2.505			2.5051	$2^+(1^-)$
2.521		12						
2.533		50						
2.545		26		2.550			2.548	$0^+,2^+$
2.557		28					2.57	
				2.582				
2.609		13		2.608		230	2.60	
2.627		10						
2.635		27		2.638		499	2.64	
2.655		12						

Table V-3 (cont'd.).

Present Experiments							Previous Results[a]	
$^{198}Pt(p,t)^{196}Pt$				$^{196}Pt(p,p')$				
E_x (MeV)	J^π	$\sigma(7^o)$ (μb/sr)	ε[b]	E_x (MeV)	J^π	$\sigma(30^o)$ (μb/sr)	E_x[c] (MeV)	J^π
2.666		11					2.662	$0^+,2^+$
2.676		20					2.67	
				2.707		298		
2.759		13						
2.766		23						
2.779		20		2.774(5)		90.5		
				2.797		62.3(35^o)		

[a]References [Mu 65, Gr 68, Ja 68, Sa 68, Ba 76, Ci 79].

[b]See footnote b in Table V-2.

[c]The states above 2 MeV seen in this work and previous results are associated only because of similar energies.

[d]Used as calibration point with energy taken from Nuclear Data Sheets B7, 395 (1972). Uncertainties in excitation energy are approximately 1 keV below 1.8 MeV and 0.1% above 1.8 MeV, except as indicated.

[e]Used as calibration point along with the 0.80310, 1.68408, 2.20023, and 2.64790 MeV levels from ^{206}Pb.

distribution has a characteristic shape of a particular L-transfer. In this study experimental shapes were compared to DWBA calculations and to shapes of angular distributions with well-known L-transfers. This study at 35 MeV is the first one in this mass region where L-transfers higher than L = 0 have been assigned (with the exception of Pb(p,t) [La 73, La 77]). The results of these shape comparisons are discussed further in the following sections for various L-transfers.

B. DWBA Analysis

The experimental angular distributions have been compared with standard, zero-range distorted waves calculations using the code DWUCK [PDKu]. Table V-4 is a list of the optical model parameters used in analyzing the (p,t) reactions. Becchetti-Greenlees [Be 69] proton parameters were used in the entrance channel, and the triton parameters were taken from Flynn et al. [Fl 69]. The wave functions were calculated for a Woods-Saxon potential with the usual prescription for the binding energy of each neutron, $0.5\ (S_{2n} + E_x)$. Here S_{2n} is the two-neutron separation energy and E_x is the excitation energy of the residual nucleus.

In order to test the effect of small changes in the optical model parameters, calculations were carried out using the Becchetti-Greenlees proton parameters for ^{208}Pb along

Table V-4. Optical Model Parameters Used in DWBA (p,t) Calculations.[a]

Parameter Set	Channel	V	r_R	a_R	W	W_D	r_I	a_I	V_{SO}	r_{SO}	a_{SO}	r_C
1	p+ ^{194}Pt	52.9	1.17	0.75	5.0	5.4	1.32	0.647	6.2	1.01	0.75	1.17
	t+ ^{192}Pt	167.0	1.16	0.752	13.61	---	1.498	0.817	---	---	---	1.16
2	p+ ^{196}Pt	53.1	1.17	0.75	5.0	5.5	1.32	0.653	6.2	1.01	0.75	1.17
	t+ ^{194}Pt	167.0	1.16	0.752	12.55	---	1.498	0.817	---	---	---	1.16
3	p+ ^{198}Pt	53.2	1.17	0.75	5.0	5.6	1.32	0.658	6.2	1.01	0.75	1.17
	t+ ^{196}Pt	167.0	1.16	0.752	11.5	---	1.498	0.817	---	---	---	1.16
Bound State		V_n[b]	1.25	0.75	---	---	---	---	λ=25	1.25	0.75	---

[a] Definition of parameters: $V(r) = -(V + iW)f(x) - 4iW_D a_I f'(\bar{x}) - V_{SO}(\vec{\sigma}\cdot\vec{\ell})\lambda^2 \frac{1}{r_{SO}} f'(x')$ where $f(x) = (1 + e^x)^{-1}$ and $x = \frac{r-R_R}{a_R}$, $\bar{x} = \frac{r-R_I}{a_I}$, and $x' = \frac{r-R_{SO}}{a_{SO}}$. r_c is the Coulomb radius.

[b] The neutron well depths were adjusted to give each orbit one-half the sum of the two neutron separation energy and the excitation energy of the residual nucleus.

with the ^{206}Pb triton parameters of Flynn et al. The results showed no major changes in the strength or shape for any of the transitions calculated for the ^{196}(p,t) reaction.

Since the platinum nuclides display low-lying collective excitations, one might expect that second-order or multistep effects would affect the strength and shape of the angular distributions in (p,t) reactions. This has been found to be true for reactions on well deformed nuclei [As 72, Ki 72]. Such effects are not accounted for in simple DWBA calculations. But, there is an absence of such strong effects in the platinum nuclides, possibly because of relatively smaller values of the quadrupole deformation parameter ($\beta_2 \simeq 0.15$ for the Pt nuclides, whereas $\beta_2 \simeq 0.3$ for well-deformed rare earths). Since the strength of multistep couplings depends on terms involving various powers of β_2, the smaller value of β_2 may be responsible for the reduction of many of the second-order reaction steps. Further evidence for the predominance of the one-step mechanism is the absence, in all three reactions studied, of any strength (> 1μb) populating the unnatural parity states, in particular the 3^+ level known to exist at ≃ 950 keV in ^{194,194,196}Pt. Such transitions are forbidden to first-order in a one-step process. Previous work [As 70, Ud 74] comparing DWBA with two-step coupled channels calculations for ^{62}Ni(p,t) and Cd(p,t), nuclei with collectivity similar to Pt, has shown that there are very small differences between the two reaction models in

predicting shapes of angular distributions. The main effect of the two-step mechanisms was seen in the transition strengths.

One method for obtaining spectroscopic information from two-nucleon transfer cross sections with DWBA calculations is to use an empirical normalization (D_o^2) to define an enhancement factor, ε, for the configuration which produces the strongest calculation for a given L transfer [Ba 73, Br 73]. The relationship between the experimental and calculated cross sections can be expressed as:

$$\left(\frac{d\sigma}{d\Omega}\right)_{exp} = 9.72\ D_o^2\ \varepsilon\ C^2 (2J + 1)^{-1}\ \sigma_{DW}^{LSJ}(\theta)\ . \qquad \text{(V-1)}$$

The factor D_o^2 is the normalization constant which results from making the zero-range approximation. A value of 2.2×10^5 MeV^2F^3 was used in these calculations [Ba 73]. The constant 9.72 is derived from the choice of the size of the outgoing triton used in DWUCK and the range parameters of the two-body interaction. The isospin coupling coefficient, C^2, is unity for all transitions. The quantity J is the total angular momentum of the transferred neutron pair and $\sigma_{DW}^{LSJ}(\theta)$ is the differential cross section calculated in DWUCK. The factor ε is a measure of the adequacy of the wave functions used in calculating the form factor. A value of $\varepsilon = 1$ would indicate an ideal wave function description if all other assumptions were valid. In the present case ε represents the relative strength for a particular L-transfer expressed in

arbitrary units (σ_{DW}^{LSJ} calculated from the dominant 2-neutron configuration). This allows for the unfolding of kinematic factors which may favor a particular L-transfer. The configurations used for each L-transfer are in the footnotes for Tables V-1, V-2, and V-3. As mentioned above, these configurations produced the greatest calculated strengths for their respective L-transfer in <u>each</u> of the three reactions, ^{194,196,198}Pt(p,t). No attempt was made to study the interference effects of using more than one term in the configuration. This could be an important factor as far as the strengths of the calculations are concerned since a coherent sum over these terms is involved. However, the enormous number of configurations precluded any meaningful approach to the problem.

C. L = 0 Transitions

As expected, the L = 0 transitions were observed with the very characteristic diffraction pattern seen in most two-nucleon transfer reactions, allowing for reliable assignments of 0^+ levels in the final nucleus. Eleven L = 0 transitions were observed in the three reactions, including the three ground state transitions and one transfer to a newly identified excited 0^+ level at 1.628 MeV in ^{192}Pt. The L = 0 transitions are shown in Figure V-1, along with the DWBA calculations. There are few differences from nucleus to nucleus, either in the phase of the distributions or in the

Figure V-1. L = 0 Angular Distributions for the ^{194,196,198}Pt(p,t) Reactions. The curves are the results of DWBA calculations. Energies are given in keV.

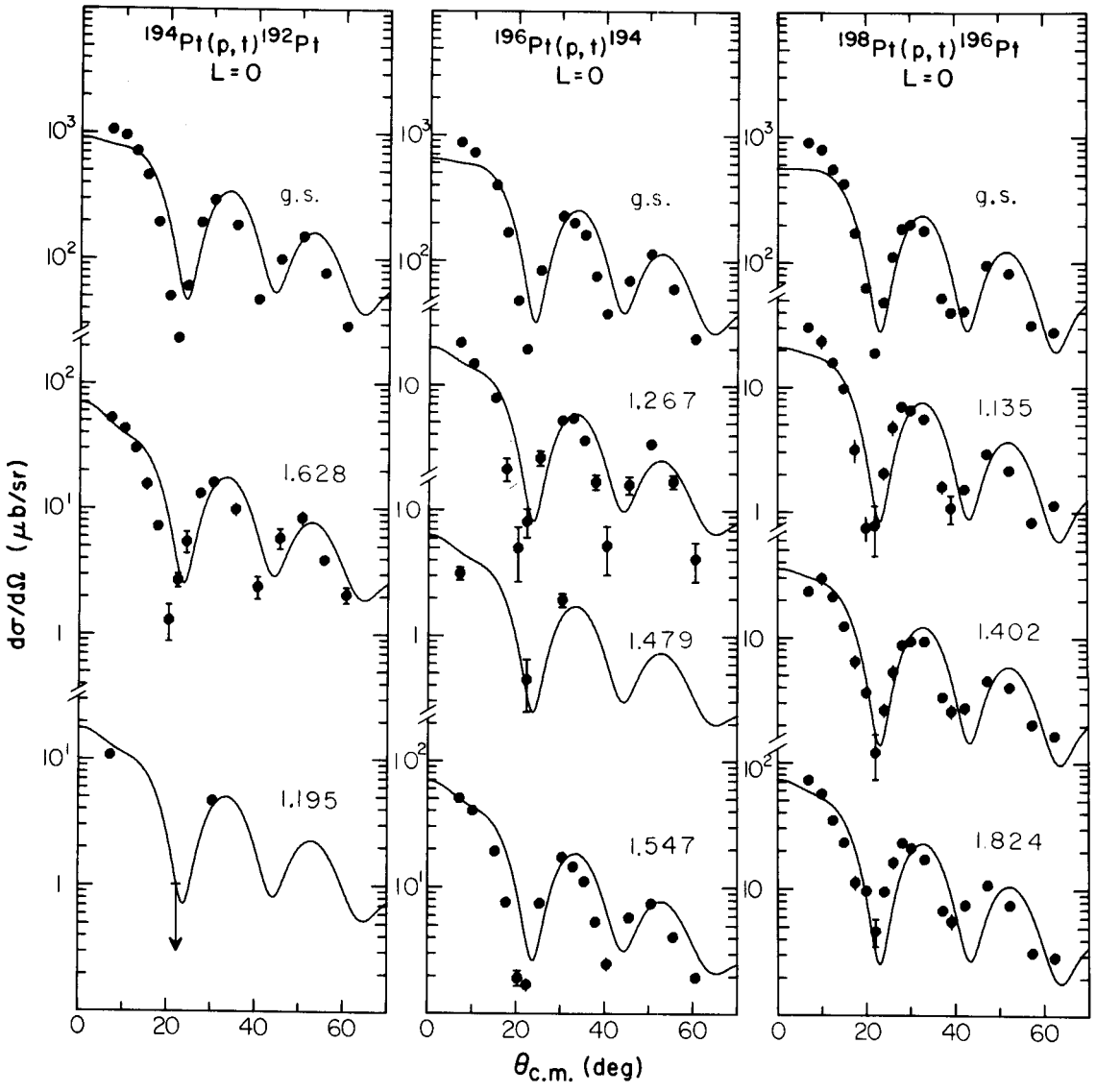
194Pt(p,t)192Pt
L=0
196Pt(p,t)194
L=0
198Pt(p,t)196Pt
L=0
g.s.
1.628
1.195
1.267
1.479
1.547
1.135
1.402
1.824
dσ/dΩ (μb/sr)
θc.m. (deg)

Figure V-1.

peak-to-valley ratios. The same is true for the calculations, which show only slight deviations at forward angles. In general, the calculated shapes are independent of Q-value or choice of the simple 2-neutron configuration used in computing the form factor.

The ground state transitions are by far the most intense transitions observed in each reaction. The strongest excited 0^+ state in Pt is populated with only 8% of the strength of the ground state at 7^o.

The 0^+ state at 1.195 MeV in ^{192}Pt, previously seen [Be 70, Fi 72] in the decay of ^{192}Au, was unresolved from the 4^+ level at 1.201 MeV in the proportional counter data used for angular distributions. The spin of this level was confirmed using the three point angular distributions taken with nuclear emulsions. The new 0^+ level seen in ^{192}Pt at 1.628 MeV was populated with 5% of the strength of the ground state at 7^o.

Three excited 0^+ states were populated in the ^{196}Pt(p,t)^{194}Pt reaction. All three states were previously seen [Be 64, Be 70, Cl 76] in the decay of ^{194}Au. The level at 1.479 MeV is very weakly excited (< 0.5% of the ground state at 7^o) and was resolved only in the plate data. The L = 0 nature of the transition populating this state was also confirmed by the three point angular distribution. The levels at 1.267 and 1.547 MeV were excited with considerably more strength, 3% and 6% respectively of the ground state

strength at 7^{o}, and the 1.547 MeV level was the only excited 0^{+} state seen in the earlier (p,t) study of Maher et al. [Ma 72]. There are two higher energy 0^{+} levels known [Be 70, Cl 76] in ^{194}Pt at 1.8936 MeV and 2.086 MeV. We observe a level weakly populated at 7^{o} in the plate data with an energy of 1.892 MeV, but an angular distribution was not obtained. We populate no state within 20 keV of the 2.086 MeV level.

Three excited 0^{+} states at energies of 1.135, 1.402, and 1.824 MeV were observed in the ^{198}Pt(p,t)^{196}Pt reaction. All levels have been previously reported, although the spin of the state at 1.402 MeV was assigned as (0, 1) in the decay of ^{196}Ir [Ja 68] and as $(0^{+},2^{+})$ in the neutron capture experiment by Samour et al. [Sa 68]. A recent (n,γ) study of ^{196}Pt by Cizewski et al. [Ci 78] also assigns a spin and parity of 0^{+} for the 1.402 MeV level.

It is significant that there is no 0^{+} experimental evidence for levels below 1 MeV in any of the three Pt isotopes studied.

D. L = 2 Transitions

In contrast to the situation for (p,t) reactions measured at lower energies in this mass region [Ma 72, Sh 76], the L = 2 transitions observed in the present study appear to be sufficiently characteristic to allow spin assignments to be made. Transitions to the known first and second 2^{+} levels have quite similar experimental angular

distributions. The major difference appears near 18° where the angular distribution for the second 2^+ has a more pronounced oscillation than for the first 2^+, as seen in Figure V–2. The angular distributions for the remainder of the excited 2^+ levels have approximately the same shape as the second 2^+ distribution. This small deviation in shapes, seen in all three reactions, may be indicative of some weak multistep effects. The sensitivity of the calculated angular distributions to changes in the two-neutron configurations is shown in Figure V–2. This could also account for the variation in 2^+ shapes.

In the ^{194}Pt(p,t)^{192}Pt reaction, only two 2^+ levels were populated with enough intensity to extract a complete angular distribution from the data. These were the well-known first and second 2^+ states at 0.316 and 0.613 MeV. Two levels at 1.439 and 1.576 MeV which have been previously assigned [Fi 62, Ya 74] as $(1^+,2^+)$ and 2^+ respectively, were weakly excited at forward angles.

Four 2^+ levels were populated in the ^{196}Pt(p,t)^{194}Pt reaction, with energies of 0.328, 0.622, 2.155, and 2.532 MeV. The two lowest energy levels have been seen in earlier studies, while the state at 2.155 MeV may be the same state seen at 2.158 MeV and assigned $(1,2)^+$ by Cleveland and Zganjar [Cl 77], and is tentatively assigned at 2^+ in the present study. The new level at 2.532 MeV is also tentatively assigned 2^+. This level may be part of a broad peak

Figure V-2. L = 2 and L = 3 Angular Distributions for the ^{194,196,198}Pt(p,t) Reactions. The curves are the results of DWBA calculations. Energies are given in keV.

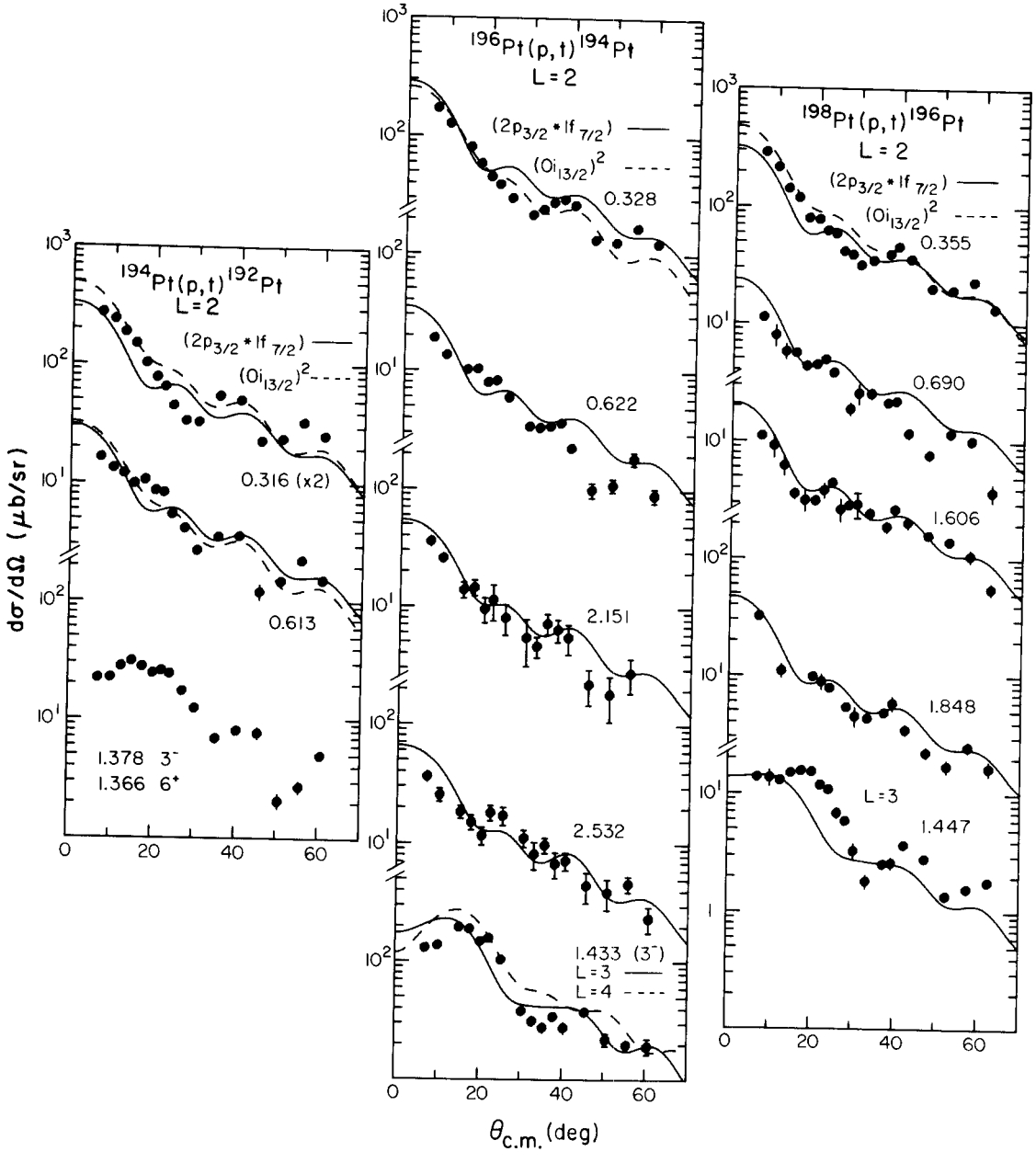
194Pt(p,t)192Pt
L=2
(2p3/2 * 1f7/2)
(0i13/2)2
0.316 (x2)
0.613
1.378 3-
1.366 6+
196Pt(p,t)194Pt
L=2
(2p3/2 * 1f7/2)
(0i13/2)2
0.328
0.622
2.151
2.532
1.433 (3-)
L=3
L=4
198Pt(p,t)196Pt
L = 2
(2p3/2 * 1f7/2)
(0i13/2)2
0.355
0.690
1.606
1.848
L=3
1.447
dσ/dΩ (μb/sr)
θc.m. (deg)

Figure V-2.

seen at 2.55 MeV in the ^{195}Pt(d,t) data and 2.56 MeV in the ^{194}Pt(d,d') study [Mu 65]. As in the ^{194}Pt(p,t) reaction, several known 2^+ levels were only weakly populated and angular distributions were not obtained for these.

In addition to the first (0.355 MeV) and second (0.690 MeV) 2^+ levels, two higher lying levels were populated in the ^{198}Pt(p,t)^{196}Pt reaction. These levels are at 1.606 and 1.848 MeV and have been assigned as 2^+. They have been confirmed in a recent (n,γ) experiment [Ci 78].

E. L = 3 Transitions

The 3^- octupole vibrational state was populated in each of the three (p,t) reactions, as shown in Figure V–2. In ^{192}Pt the 3^- state at 1.378 MeV and the 6^+ state at 1.366 MeV were not completely resolved, although the contribution to the cross section from the L = 6 transfer is thought to be small. As shown in Figure V–2, the L = 3 DWBA fits are quite poor, missing the first maxima by as much as 10°. This may be the result of multistep effects, because the 3^- state is strongly populated in scattering studies [Mu 65, Ro 77]. In fact, this rather strong population of the 3^- levels is somewhat unexpected. Such states are very weak in the Pb(p,t) reactions [La 73], which is understood because the 3^- state is basically particle-hole in nature, while (p,t) excites 2–particle, 2–hole states.

F. L = 4 Transitions

The spin assignments from L = 4 transitions required special attention in this study, due to the seemingly uncharacteristic shape of the angular distribution populating the well-known first 4^+ level in all three reactions. This shape differs from the shape seen in both the simple two-neutron DWBA calculations of L = 4 transfers, and the Pt(p,t) data of Lanford [La 73, La 77]. As shown in Figure V-3, the angular distributions for the first 4^+ levels have no distinct maximum at 15^o, but continue to rise toward forward angles and also show a pronounced minimum at 30^o. The angular distribution for the other known 4^+ levels (1.229 MeV in ^{194}Pt and 1.201 MeV in ^{192}Pt) is characterized by a distinct maximum near 15^o, more closely resembling that calculated in DWBA and in the Pb(p,t) reactions. It was the latter shape that was used to make spin assignments for possible high-lying 4^+ levels.

In addition to the first 4^+ state, at least two more excited 4^+ states were seen in each reaction, and in the ^{196}Pt(p,t) reaction six more 4^+ states have been tentatively identified. The 1.201 MeV level in ^{192}Pt, a known 4^+ state, was not resolved from the weakly populated 1.195 MeV 0^+ level, although the 4^+ angular distribution should be only slightly affected by the 0^+ level. The plate data, in which the 4^+ and 0^+ are nearly resolved, support this. A possible third 4^+ level in ^{192}Pt was seen at 1.937 MeV, although its

Figure V-3. $L \geq 4$ Angular Distributions for the $^{194,196,198}Pt(p,t)$ Reactions. The curves are the results of DWBA calculations. Energies are given in keV.

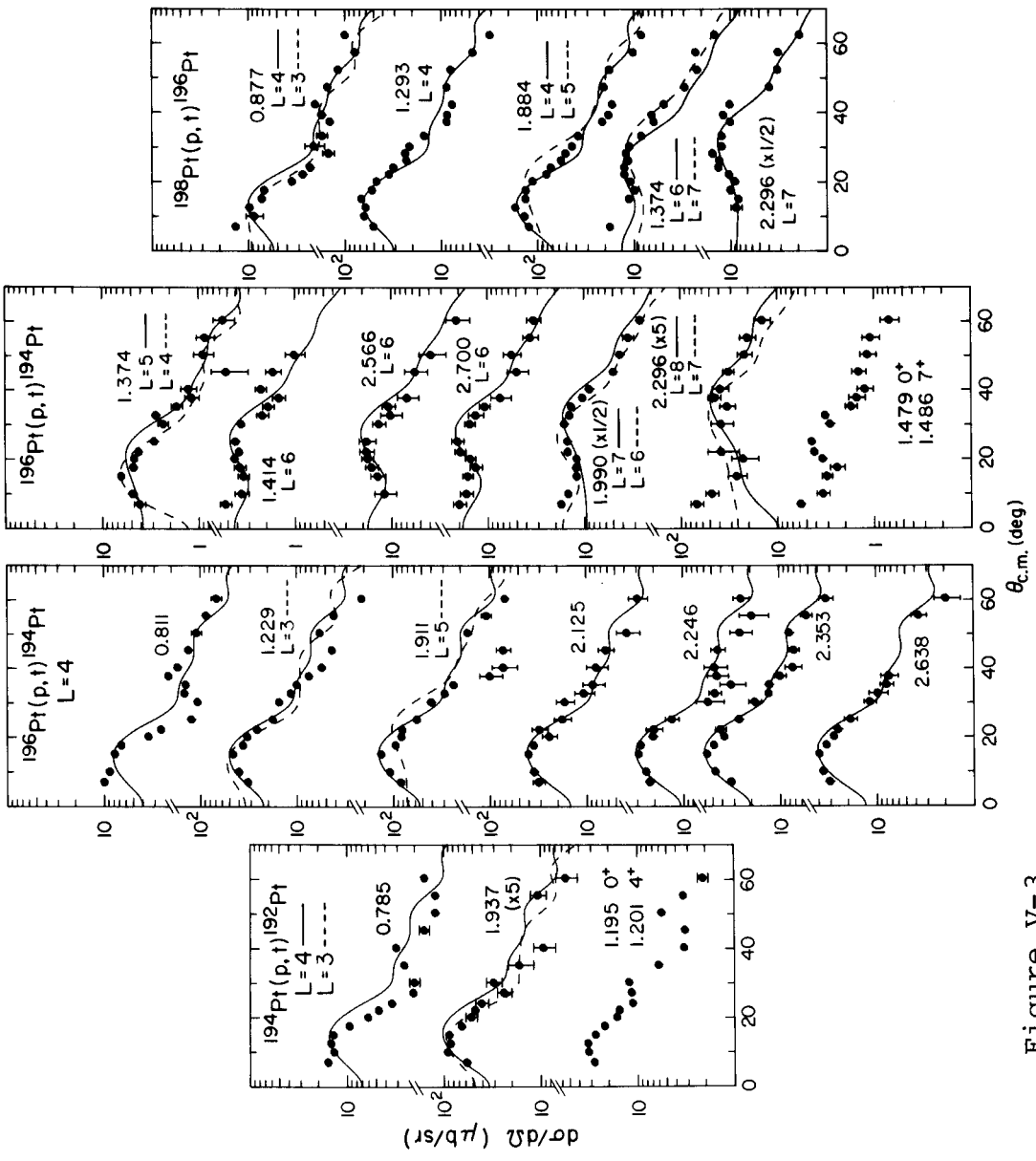
^{194}Pt(p,t)^{192}Pt
L=4
L=3
0.785
1.937 (x5)
1.195 0+
1.201 4+
^{196}Pt(p,t)^{194}Pt
L=4
0.811
1.229 L=3
1.911 L=5
2.125
2.246
2.353
2.638
^{196}Pt(p,t)^{194}Pt
1.374 L=5 L=4
1.414 L=6
2.566 L=6
2.700 L=6
1.990 (x1/2) L=7 L=6
2.296 (x5) L=8 L=7
1.479 0+
1.486 7+
^{198}Pt(p,t)^{196}Pt
0.877 L=4 L=3
1.293 L=4
1.884 L=4 L=5
1.374 L=6 L=7
2.296 (x1/2) L=7
dσ/dΩ (μb/sr)
θc.m. (deg)

Figure V-3.

interpretation as a 3^- state cannot be ruled out, as the DWBA calculations for L = 4 and L = 3 are quite similar. The assignment is tentatively made as 4^+ because of the appearance of possible 4^+ levels near this energy in ^{194}Pt and ^{196}Pt. Also, the empirical shape of the L = 3 angular distributions for the three known 3^- levels is considerably flatter at forward angles (see Figure V–2).

In addition to the known 4^+ levels at 0.811 and 1.229 MeV, five new levels were populated in ^{194}Pt with L = 4 shapes, at energies of 1.911, 2.125, 2.246, 2.353, and 2.638 MeV, and thus have been tentatively assigned as 4^+ levels.

In ^{196}Pt two levels were populated by transitions whose angular distribution shape is that of an L = 4 transfer. The level at 1.293 MeV may have been observed in inelastic alpha scattering (1.290 MeV) [Ba 76], but was not assigned a spin or parity. An L = 4 fit is not very good, but this deficiency is partially due to unfolding the contribution of the nearby 5^- level at 1.271 MeV. The trend in the other two Pt nuclei studied would suggest this is the second 4^+ level. The level at 1.884 MeV in ^{196}Pt was populated very strongly with the shape of an L = 4 transfer, and completes a series of new, strongly populated 4^+ levels seen at $\simeq$ 1.9 MeV in all three (p,t) reactions. This level may be the same one seen in the (d,d') study [Mu 65] at 1.88 MeV.

G. $L \geq 5$ Transitions

Only limited success was achieved with assigning J^{π} values to states populated by L transfers greater than 4. Although the DWBA calculations showed the first maximum shifting approximately 5^{o}–10^{o} towards backward angles as the transferred angular momentum increased by one unit, there was only one known higher spin state populated with a complete angular distribution for comparison. This was the 6^{+} level in ^{194}Pt at 1.414 MeV. The other known levels with spins greater than 4 were either unresolved from other levels (1.486 MeV 7^{-} in ^{194}Pt and 1.271 MeV 5^{-} in ^{196}Pt), or too weakly populated for a complete angular distribution (1.517 MeV 7^{-} and 2.019 MeV 8^{+} in ^{192}Pt). Nevertheless, several spin assignments have been proposed for levels in ^{194}Pt and ^{196}Pt as shown in Figure V–3.

In ^{194}Pt a level at 1.374 MeV was populated, which has been assigned as a 5^{-} level in (α,xn) reactions [Ya 74, Hj 76] and as (6^{+}) or $(4,5^{-})$ in ^{194}Au decay [Be 70] and triple neutron capture [Su 68]. From the present (p,t) results a clear distinction cannot be made between L = 4 and L = 5 transfer. As a result, the state has been assigned $(4^{+},5^{-})$ from the natural parity selection rule.

The level at 1.414 MeV, a known 6^{+} state, is reproduced by the L = 6 calculation, particularly in the angular region about the maximum. This leads us to propose two additional levels to be assigned at 6^{+}, at 2.566 and 2.700 MeV, as shown

in Figure V–3. Levels at 1.990 and 2.296 MeV have been assigned J^{π} values $(6^+,7^-)$ and $7^-,8^+)$, respectively. A unique assignment was not possible because of the similarity of the shapes for the calculated L–transfers involved in each case.

In the ^{198}Pt(p,t) reaction, two high-spin levels have been identified, at energies of 1.374 and 2.296 MeV. The first level was assigned as $(6,7)^-$ in the decay [Ja 68] of ^{196}Ir, and the (p,t) angular distribution data show it to be either a 6^+ or 7^- state. Thus, from the (p,t) natural-parity selection rule, this is therefore most likely a 7^- state and may be related to the 7^- state observed at 1.518 MeV in ^{192}Pt andl.485 MeV in ^{194}Pt. The second level, at 2.296 MeV, is assigned as $(7^-,8^+)$.

H. Relative Reaction Strengths

The triton spectra shown in Figure IV–3 for the three rections show many of the same overall features. The most notable are: strong population of the ground state and first 2^+ level in the residual nucleus; several excited L = 0 transitions; and an increasing population of the 4_2^+ and 4_3^+ levels as the mass of the target increases. Table V–5 displays for each reaction the integrated differential cross section from 7^o to 60^o for the more strongly populated levels below 2 MeV. The values for the enhancement factors, ε, are listed in Tables V–1, V–2, and V–3. Since these calculations

Table V-5. Integrated Cross Sections[a] for Transitions in ^{194,196,198}Pt(p,t) and Cross Section Ratios Relative to the Ground State of ^{192}Pt. Calculations in the O(6) limit of the IBA model[b] for the L = 0 and L = 2 transitions, normalized to the ^{192}Pt g.s. and the ^{192}Pt 2_1^+ transitions respectively, are also shown.

J^π	^{194}Pt(p,t)^{192}Pt				^{196}Pt(p,t)^{194}Pt				^{198}Pt(p,t)^{196}Pt			
	E (keV)	σ_{exp} (mb)	σ/σ_{192} (exp)	σ/σ_{192} O(6)	E (keV)	σ_{exp} (mb)	σ/σ_{192} (exp)	σ/σ_{192} O(6)	E (keV)	σ_{exp} (mb)	σ/σ_{192} (exp)	σ/σ_{192} O(6)
0_1^+	0.0	73.8	1.0	1.0	0.0	61.0	0.83	0.90	0.0	57.8	0.78	0.76
0_2^+	1195	1.36	0.02	0.0004	1267	1.42	0.02	0.0003	1135	1.72	0.02	0.0002
0_3^+	1628	3.77	0.05	0.040	1479	0.23	0.003	---	1402	2.56	0.03	0.067
0_4^+	---	---	---	0.008	1547	4.00	0.05	0.039	1824	5.50	0.07	0.032
0_5^+	---	---	---		1892[c]	0.39	0.005	0.016	---	---	---	---
2_1^+	316	11.0	0.15	0.15	328	13.6	0.18	0.14	355	20.1	0.27	0.14
2_2^+	613	1.67	0.02	0.029	622	1.72	0.02	0.013	689	0.97	0.01	0.001
2_3^+	1439[c]	0.1	0.001	0.018	1512[c]	0.1	0.001	0.021	1362[c]	0.25	0.003	0.048
3^-	1378	3.03	0.04		1433	2.58	0.03		1447	2.10		0.03

Table V-5 (cont'd.).

J^π	$^{194}Pt(p,t)^{192}Pt$				$^{196}Pt(p,t)^{194}Pt$				$^{198}Pt(p,t)^{196}Pt$			
	E (keV)	σ_{exp} (mb)	σ/σ_{192} (exp)	σ/σ_{192} 0(6)	E (keV)	σ_{exp} (mb)	σ/σ_{192} (exp)	σ/σ_{192} 0(6)	E (keV)	σ_{exp} (mb)	σ/σ_{192} (exp)	σ/σ_{192} 0(6)
4_1^+	785	1.42	0.02		811	0.95	0.01		877	1.03		0.01
4_2^+	1201	2.35	0.03		1229	5.63	0.08		1293	6.72		0.09
4_3^+	1937	1.79	0.02		1911	14.8	0.20		1884	18.4		0.25

[a]Integration performed between 7^o and 60^o. Uncertainties are 10-15%.

[b]Reference [OSch].

[c]These states were not identified in this experiment as 0^+ or 2^+ levels. However, their 7^o cross sections have been used to scale their total cross section with that of the ground state or 2_1^+ for comparison with the calculations for the 0(6) limit of the IBA.

used only a simple 2-neutron wave function, values of ε differing from unity suggest the absence of correlations in the wave function. As expected, the ground state transitions are the most enhanced with an ε of 5.1 in ^{194}Pt(p,t) and 3.7 in ^{198}Pt(p,t). While the ground state population is decreasing with increasing A, the enhancement of the first 2^+ level and third 4^+ is increasing with A from 0.84 to 2.2, and 0.32 to 2.1 respectively. Although ε was not calculated for the 4_2^+ level in ^{192}Pt, Table V-5 shows the total cross section of this state also increases with A. In addition, the enhancement of the 4_1^+, 2_2^+, 3^-, and the excited 0^+ levels remains relatively constant in all three reactions.

These same general trends, decreasing ground state population and a general increase in population of excited states with increasing A, were seen in the (p,t) reactions on the Pb nuclides [La 73]. This was interpreted as an indication of an increase in the two-particle coherence of the wave functions as one moves away from the closed shell. The decreasing ground state population from ^{192}Pt to ^{196}Pt is not as dramatic as that seen in the Pb data, but this is understandable from a simple pairing-vibration model [Br 73]. If the creation and annihilation operators for the two-neutron pickup are treated as boson operators, then the strength of the transitions is related to the number of pairs of neutrons (phonons) or holes, in the final state, relative to the nearest closed shell. For ^{202,204,206}Pb, the strengths of

the ground state transitions should be in the ratio 3:2:1, while for ^{194,196,198}Pt the ratio would be 6:5:4. This is consistent with the experimental Pt ratio of 6.1:5.0:4.7, with 15-20% uncertainties on these numbers. Arima and Iachello [Ar 77a] have noted that both finite dimensionality effects and an increase in collectivity as one proceeds into a shell are important and give quantitative predictions for these effects with the IBA; however, the uncertainties on our measured ground-state strengths are too large for us to observe such an effect.

I. General Discussion of (p,t) Results

1. L = 0 Transitions

One of the primary reasons for the current reaction study was to search for any low-lying 0^+ states that could be interpreted as the "missing" 0^+ state of the 2-phonon triplet in a vibrational model interpretation. Although (p,t) transitions to 2-phonon states are forbidden in first-order, these states have been seen [Co 72, Kr 77] in (p,t) reactions on Cd and Pd, probably due to two-step transfers and/or anharmonic terms in the vibrational potential. No evidence for low energy, L = 0 transitions populating a 0^+ level is seen in any of the three (p,t) reactions. In fact, no new levels were populated below $\approx$ 1.5 MeV with a cross section $\gtrsim$ 1 μb/sr at forward angles, about 0.1% of the ground state population. (In Cd, generally considered a good example of a

vibrational nucleus, the relative (p,t) strength ratio for $0^+_2/0^+$ g.s. is $\simeq 0.25\%$.)

A second result of the (p,t) experiments is the absence of any strong L = 0 transitions populating excited 0^+ levels. As mentioned in the Introduction, a strong L = 0 transition ($\simeq$ 50–100% of the ground state strength) might have indicated a shape-isomeric level in the residual nucleus related to the γ degree of freedom. The strong transition would occur if there was a large overlap of the target, ground state wave function with the wave function of an excited 0^+ state in the residual nucleus. For this region of nuclei, this would seem to imply a stable triaxial minimum in the potential of each nucleus. Since no transition was observed that was stronger than 10% of the total ground state cross section, the data seem to be consistent with an interpretation of these nuclei as being soft, with shallow minima in the potential surface.

Tables V–1, V–2, and V–3 show three or four excited 0^+ levels weakly populated in each of the (p,t) reactions studied. Most of these 0^+ states are not easily interpreted within current models for this region. The energy is too high in the Pt region ($\simeq$ 1.2 MeV) for the first excited 0^+ state to be a member of the 2–phonon triplet in a strict vibrational sense, although the pairing-plus-quadrupole model predictions of Kumar and Baranger [Ku 68] are quite reasonable: 1.207, 1.101, and 1.018 MeV for the first excited 0^+ states in ^{192,194,196}Pt respectively. The cross

section for populating the first excited 0^+ state in (p,t) is 2–3% of the ground state in each reaction, rather weak for it to be considered the so-called "β–vibrational" state of a symmetric rotor; the typical cross section for the first excited 0^+ levels in deformed nuclei is approximately 5–10% of the ground state. Some of the higher energy 0^+ states may carry more of the β–vibrational strength, as they are populated by stronger L = 0 transitions.

One interpretation of the 0^+ levels may be that they are the K = 0, two γ–phonon bandhead of a symmetric rotor, as possibly seen [Ya 63, Sh 76] in ^{188,190,192}Os. The energy of these 0_2 levels is quite close to the Bohr-Mottelson prediction of twice the single γ–phonon bandhead (≃ 625 keV in Pt). Existing branching data for the decay of the first excited 0^+ state in $^{190-196}$Pt also supports this phonon interpretation with the ratio

$$(B(E2)0_2^+ \rightarrow 2_2^+)/(B(E2)0_2^+ \rightarrow 2_1^+) > > 1.$$

2. L = 4 Transitions

The new 4^+ states near 1.9 MeV in excitation warrant particular attention because of their possible similarities to the third 4^+ states seen in the neighboring Os isotopes. There have been two explanations offered for these states in Os. One possible explanation for these 4_3^+ levels may be that they are the bandheads for the K = 4 component of the 2–phonon γ–vibrations of the symmetric rotor. These states

are seen in the Os(p,t) studies [Sh 76] at an energy near 1.2 MeV. There are problems with this interpretation for the Pt isotopes from an energy standpoint, however, as their energy ($\simeq$ 1.9 MeV) is much too high in the vibrational model, which predicts the energy to be about twice the energy of the 1-γ phonon bandhead (2_2^+), or about 1.2 MeV for Os and Pt. The energies are too low for the triaxial rotor model [Da 58]. Here, the energies can be determined from the sum rule

$$\sum_{i=1}^{3} E(4_i^+) = 5\ E(3^+)\ , \qquad \text{(V-2)}$$

giving $E(4_3^+) \simeq 2.5$ MeV in the Pt nuclides.

On the other hand, the decay properties of these 4_3^+ levels in the Os region [Ca 78] tend to support a 2-phonon interpretation as each level primarily decays to the second 2^+ state rather than the first 2^+. However, additional problems arise from this interpretation due to the strength of the 4^+ transitions in ^{196,198}Pt(p,t). Because (p,t) transitions to 2-phonon states are forbidden to first order in a pure vibrational model, such states should be only weakly populated as a result of multistep effects and anharmonicities in the vibrational potential. In the Cd region, the population of 2-phonon states is typically 1-5% of the ground state population. Similarly, in Os(p,t) the strength of the transition populating the 4_3^+ level is $\simeq$ 1-2% of the ground state. However, in ^{196,198}Pt(p,t) the strength of this transition is $\simeq$ 15% of the ground state while only in ^{194}Pt(p,t) is it as low as 1% of the ground state strength.

Thus, a uniformly simple interpretation of the $K^{\pi} = 4_3^+$ bandheads as vibrational states in the ^{192,194,196}Pt isotopes is doubtful.

Recently, Bagnell et al. [Ba 77] have argued from the calculations explaining the strength of the 4_3^+ states in the ^{191,193}Ir(t,α)^{190,192}Os reactions that these states could be described as single phonon, hexadecapole vibrations. This interpretation was also presented in a recent (α,α') study [Bu 78]. These 4_3^+ states may then be a mixture of both the 2γ–phonon and the hexadecapole-type vibrations. If an attempt is made to extend this interpretation to the Pt isotopes, one must take into account the varying strength that is seen in populating these states in both the (p,t) and (p,p') studies. In the ^{194}Pt(p,t),(p,p') reactions, the population of the 4_3^+ state is comparable to that seen in the analogous Os experiments. However, in the ^{196,198}Pt(p,t),(p,p') reactions, the additional strength of these states indicates a change in their structure. Since to first order (p,t) reactions should populate only one-phonon states, the fact that the 4_3^+ states are populated very strongly indicates only a small 2–phonon component. In addition, a large E4 component is needed to account for the 4^+ strengths seen in the (p,p') reactions (see next Chapter). These observations seem to indicate that as the mass increases in the Pt isotopes, the 4_3^+ seem to be exhibiting a larger hexadecapole component in their wave functions.

In the $^{204}Hg(p,t)^{202}Hg$ reaction at E_p = 17 MeV, a strong L = 4 transition was also seen with 40% of the ground state transition strength [Ma 74]. It was noted by Breity et al. [Br 75] that DWBA calculations for this seem to indicate large in-phase $(2p_{3/2} \otimes 1f_{5/2})$ and $(1f_{7/2} \otimes 2p_{1/2})$ neutron components in the transfer form factor. By using the ^{206}Pb 4_2^+ wave function of Vary and Ginocchio [Va 71] with the $(1f_{7/2} \otimes 2p_{1/2})$ amplitude enhanced by a factor of 2 to 3, the cross section for the 4_2^+ state surpasses that of the first 4^+. In the present study, these same two configurations provided the greatest calculated strengths for all L = 4 transitions and the $(2p_{3/2} \otimes 1f_{5/2})$ configuration was used in calculating the enhancement factors. The suggestion that the lack of large 4^+ cross sections in the lighter Hg isotopes may be due to a depletion of the $2p_{1/2}$ orbital [Br 75] may apply to the lighter Pt nuclides as well. Since these nuclides are farther away from the N = 126 shell closure, decreasing occupancy of the $1f_{5/2}$ orbital now becomes a factor rather than the $2p_{3/2}$ orbital. Thus, this same effect may explain the generally decreasing strength of the 4^+ levels as A decreases (see Table V-5).

3. L = 0, 2 Transitions in the Interacting Boson Approximation

It has been shown by Arima and Iachello [Ar 77a] that the IBA model provides a natural framework for a unified description of 2-nucleon transfer reactions across a complete

shell. The ease of associating the IBA with 2-nucleon transfer reactions is due to the inherent coupling in this model of pairs of fermions to bosons with angular momentum 0 and 2, or s and d bosons. It is also possible to treat higher L-transfers by coupling the bosons to form higher order operators, or alternatively by adding g bosons (L = 4). This discussion is restricted to the L = 0, 2 transitions. Reference [Ar 77a] investigates 2-nucleon transfer reactions in the SU(5) (vibrational) and SU(3) (rotational) limits, while this study presents features of (p,t) reactions near the O(6) limit.

The operators for the (p,t) reaction can be expressed in terms of creation and annihilation operators for the s and d bosons, $s^{\dagger}(d^{\dagger})$ or s(d), depending on whether one is near the end or beginning of a shell. This change of operators is due to a change from particles to holes in describing the system. For the L = 0 transitions in (p,t) reactions the operator, to first order, has the form [FIac]

$$T_{+\nu}^{(0)} = \alpha_{\nu} s^{\dagger} (\Omega_{\nu} - N_{\nu} - N_{d\nu})^{1/2} \quad . \tag{V-3}$$

In this notation a distinction is made between boson operators for neutrons ($s_{\nu}^{\dagger}$) and protons, as the calculations discussed below have been performed [OSch] using a code which allows for both neutron and proton bosons. Other quantities in the operator are a strength factor, α_{ν} ; the effective neutron degeneracies for the sub-shell in question, Ω_{ν} ; the

neutron pair number, N_ν; and the neutron d boson number, $n_{d\nu}$. The factor

$$[\Omega_\nu - N_\nu - n_{d\nu}]^{1/2}$$

is a result of the finite dimensionality of the shells. The eigenfunctions in the O(6) limit are denoted by three primary quantum numbers, σ, τ, and ν_Δ, which were discussed in Chapter II.E.4. The quantum number τ is related to the expectation value of the number of d boson, $n_{d\nu}$,

$$\langle n_d \rangle = \frac{N(N-1)}{2(N+1)} + \frac{\tau(\tau+3)}{2(N+1)} , \qquad \text{(V-4)}$$

where N is the number of bosons in the nucleus. Table V-6 shows the relationship between τ and n_d for the low-lying 0^+ and 2^+ levels in ^{194}Pt. This analogy between τ and the number of d bosons is made to show the correspondence between the change in τ (or n_d) in the O(6) limit for a (p,t) reaction versus the "change in phonons" terminology of the more common pairing vibration model [Br 73]. There is no one-to-one correspondence of the two descriptions due to the inclusion of finite dimensionality of the IBA.

For L = 0 transitions there is a $\Delta\tau = 0$ selection rule which requires that the average number of d bosons does not change. Thus, the relative strengths of these transitions can be predicted by a check of the O(6) wave functions for the 0^+ states. For example, in the ^{196}Pt(p,t)^{194}Pt reaction, the ground states for both nuclei have $\tau = 0$ or $\langle n_d \rangle \simeq 2$, while

Table V-6. Relationship Between the n_d and τ Quantum Numbers for States in the SU(5) Limit (Harmonic Vibrator) and O(6) Limit of the IBA.

State	SU(5)		O(6)			
	n_d	$E_x/E_{2_1^+}$ [a]	τ	$\langle n_d \rangle$	$\langle n_d \rangle - \langle n_d^{g.s.} \rangle$	$E_x/E_{2_1^+}$ [a]
0_1^+ (g.s.)	0	0	0	15/7	0	0
2_1^+	1	1	1	17/7	2/7	1
2_1^+, 4_1^+	2	2	2	20/7	5/7	2.5
3_1^+, 4_2^+	3	3	3	24/7	9/7	4.5

[a] For SU(5) the energies are given by εn_d, and for O(6) they are $(\langle n_d \rangle - \langle n_d^{g.s.} \rangle)$. Values taken from [Ca 78].

the first and second excited 0^+ states in ^{194}Pt have $\tau = 3$ ($\langle n_d \rangle \simeq 3$) and $\tau = 0$ ($\langle n_d \rangle \simeq 2$) respectively. Thus, in the O(6) limit the strongest L = 0 transitions would be the ones populating the ground state and second excited 0^+. This is indeed what is observed experimentally as shown in Table V–5. For two of the three reactions in this study, the second excited 0^+ state is more strongly populated. The exception is the 1479 keV level in ^{194}Pt. However, it is believed that the 1479 KeV level in ^{194}Pt may not be a collective state, but single-particle in nature [FIac], since it lies near the pairing gap for the Pt nuclides. The cross sections reported in Table V–5 have not been corrected for Q–value differences since this has been shown to be a small effect for (p,t) reactions with outgoing triton energies greater than 20 MeV [Sa 79].

The stronger population of the second excited 0^+ state relative to the first in Pt(p,t) reactions has not been satisfactorily explained by any other model. The results of calculations using the $T^{(0)}_{+\nu}$ operator given above are shown in Table V–5. The strengths are calculated in the O(6) limit with a small quadrupole-quadrupole boson interaction which breaks the pure O(6) symmetry and accounts for the changing properties of these nuclei as the O(6) to rotor transition progresses. These calculations also reproduce the increasing strengths for the ground state to ground state transitions as A decreases, a trend which extends to the ^{190}Pt(p,t)^{188}Pt reaction as well [Ve 76].

For the L = 2 transitions the operator becomes somewhat more complex as a change in seniority of 0, ± 2 is allowed. The L = 2 operator can be expressed as [FIac]

$$T^{(2)}_{+\nu} = (\alpha_\nu d^\dagger_\nu + \beta_\nu [d^\dagger_\nu d_\nu s^\dagger_\nu]^{L=2} + \gamma_\nu [d^\dagger_\nu d_\nu d_\nu]^{L=2})A \ ,$$

where the change in seniority for each term is +2, 0, −2 respectively. Here α_ν, β_ν, and γ_ν are relative strength factors for each coupling of s and d bosons and A is a finite dimensionality factor similar to that for $T^{(0)}_{+\nu}$. The brackets represent angular momentum couplings. Calculations have been carried out [OSch] using only the first and second terms of this operator with β_ν chosen to be 0.08. The results are shown in Table V–5. The governing selection rule is $\Delta\tau = +1$, which would allow only the population of the lowest of the first three 2^+ levels in the strict O(6) limit, since the ground state wave function has $\tau = 0$ and the first 2^+ state has $\tau = 1$, while the 2^+_2 state has $\tau = 2$ and the 2^+_3, $\tau = 4$. The addition of the small symmetry breaking term will allow some population of the other 2^+ levels as well, due to the mixing of the wave functions.

For relative populations within a nucleus, the general agreement of the IBA model calculations for the L = 2 transitions is very reasonable, but the calculations do not predict the proper trends from one nucleus to the next. For example, the model predicts a virtually constant 2^+_1 population, while experimentally the population of the 2^+_1 state increases

almost twofold from ^{192}Pt to ^{196}Pt. The calculations also predict a decrease in strength for populating the second 2^+ as A increases, while experimentally one observes a constant strength. It is possible that the calculations could be improved with a more judicious choice of the relative phases and magnitudes for the coefficients in the L = 2 operator, as well as investigating the effects of the third term of Equation (V-5). It should be noted that the smaller values calculated for both the L = 0 and L = 2 transitions (i.e. ^{192}Pt(0_2^+):0.0004) may have large uncertainties, as higher order terms not included in $T_{+\nu}^{(0,2)}$ may provide a significant contribution to these small values.

CHAPTER VI

RESULTS FOR THE ^{194,196,198}Pt(p,p') REACTIONS

A. General Analysis

Approximately 45-50 levels were populated in each of the three reactions up to ≃ 3.0 MeV in excitation energy. In the case of ^{198}Pt(p,p'), 38 of the 44 levels observed are reported for the first time. Only the energy of the first 2^+ state was accurately known before this study. Tables V–2, V–3, and VI–1 summarize the excitation energies, cross sections ($\theta_{Lab} = 30^o$) and assignments of J^π in the ^{194,196,198}Pt(p,p') reactions. The results from previous studies of these nuclei are included in addition to the results of the (p,t) reaction studies of ^{194,196}Pt for comparison. The energy measurements for levels in ^{198}Pt and ^{196}Pt were made from plate data taken at $\theta_{Lab} = 43^o$. Accurately known levels from the ^{206}Pt(p,p') reaction, recorded on the same plate, were used as additional calibration lines. The energy measurements for levels in ^{194}Pt were taken from plate data ($\theta_{Lab} = 25^o$) using internal, well-known level energies. Some levels do not have values for the cross section because these states were generally too weak to obtain a complete angular distribution.

Table VI-1. States Populated in the $^{198}Pt(p,p')$ Reaction.

Present Experiment			Previous Results[a]	
$^{198}Pt(p,p')$				
E_x[b] (MeV)	J^π	$\sigma(30^o)$ (μb/sr)	E_x[b] (MeV)	J^π
0.0	0^+	4.92×10^5	0.0	0^+
0.407[c]	2^+	3.24×10^3	0.4072	2^+
0.775	2^+	55.1(40^o)	0.775	2^+
0.984	4^+	1.05×10^3	0.991	4^+
1.246(3)	(3^+)	21.9		
1.287	4^+	252	1.305	
1.367	(5^-)	142		
1.445(3)		56.6		
1.502(3)	(7^-)	82.8		
1.657		119		
1.682	3^-	845		
1.722(3)		25.5(40^o)	1.722	(3^-)
1.785	(4^+)	150		
1.827(4)				
1.900		113		
1.949				
1.971(4)				
2.000				
2.070		46.6(40^o)		
2.100		74.9		
2.120		57.9		
2.155		137		
2.178		52.7		
2.319				
2.339				

Table VI-1 (cont'd.)

Present Experiment			Previous Results[a]	
$^{198}Pt(p,p')$				
E_x[b] (MeV)	J^π	$\sigma(30^o)$ (μb/sr)	E_x[b] (MeV)	J^π
2.356				
2.387				
2.441		369		
2.469		49.9		
2.514		108		
2.573		36.3	} 2.53	
2.611		762		
2.633				
2.666		96.5		
2.726		62.3		
2.782				
2.796		325		
2.826		385		
2.884		38.4		
2.910		38.0		
3.005				
3.018				
3.170(5)				
3.197(5)				

[a] References [Mu 65, Br 70, Ba 76].

[b] Uncertainties in the excitation energies are approximately 2 keV below 2.5 MeV and 0.1% above 2.5 MeV, except where indicated.

[c] Used as calibration point along with the 0.80310, 6.68408, 2.20023, and 2.64790 MeV levels from ^{206}Pb.

An attempt was made to assign spin and parity to many of the states seen in each reaction using the DWBA code DWUCK [PDKu] and standard, collective model form factors (see Chapter II.B.4). Except for the ground state, and to some extent the first 2^+ level, the DWBA calculations provided very poor fits to the data. The few spin assignments made relied on empirical shapes of angular distributions for states with well-known J^π. This method, in addition to energy and spin systematics in the Pt nuclei, has allowed several new spins to be proposed and a few assignments to be confirmed. These techniques were particularly successful for ^{198}Pt since the spin and parity of only three levels had been previously determined. The following sections will discuss many of the levels populated in all three reactions according to the particular L-transfer.

1. Elastic Scattering and L = 0 Transitions

The shape of the elastic angular distributions (Figure VI-1) is virtually the same in each reaction. The most notable features at this energy are the "plateau" around 40°, a decrease in cross section of three orders of magnitude within the angular range studied, and three distinct minima between 50° and 100°. The ratio of the elastic scattering to the classical, Rutherford scattering is shown in Figure VI-1 for ^{194}Pt(p,p'). The Rutherford differential cross section is given by

$$\left(\frac{d\sigma}{d\Omega}\right)_R^{c.m.} = \left(\frac{Z_1 Z_2}{4E_{c.m.}}\right)^2 \frac{1}{\sin^4(\theta/2)} ,$$

Figure VI-1. Elastic Scattering and L = 0, 2 Angular Distributions Seen in the ^{194,196,198}Pt(p,p') Reactions. The curves are the results of DWBA calculations using a collective model form factor. Energies are given in keV.

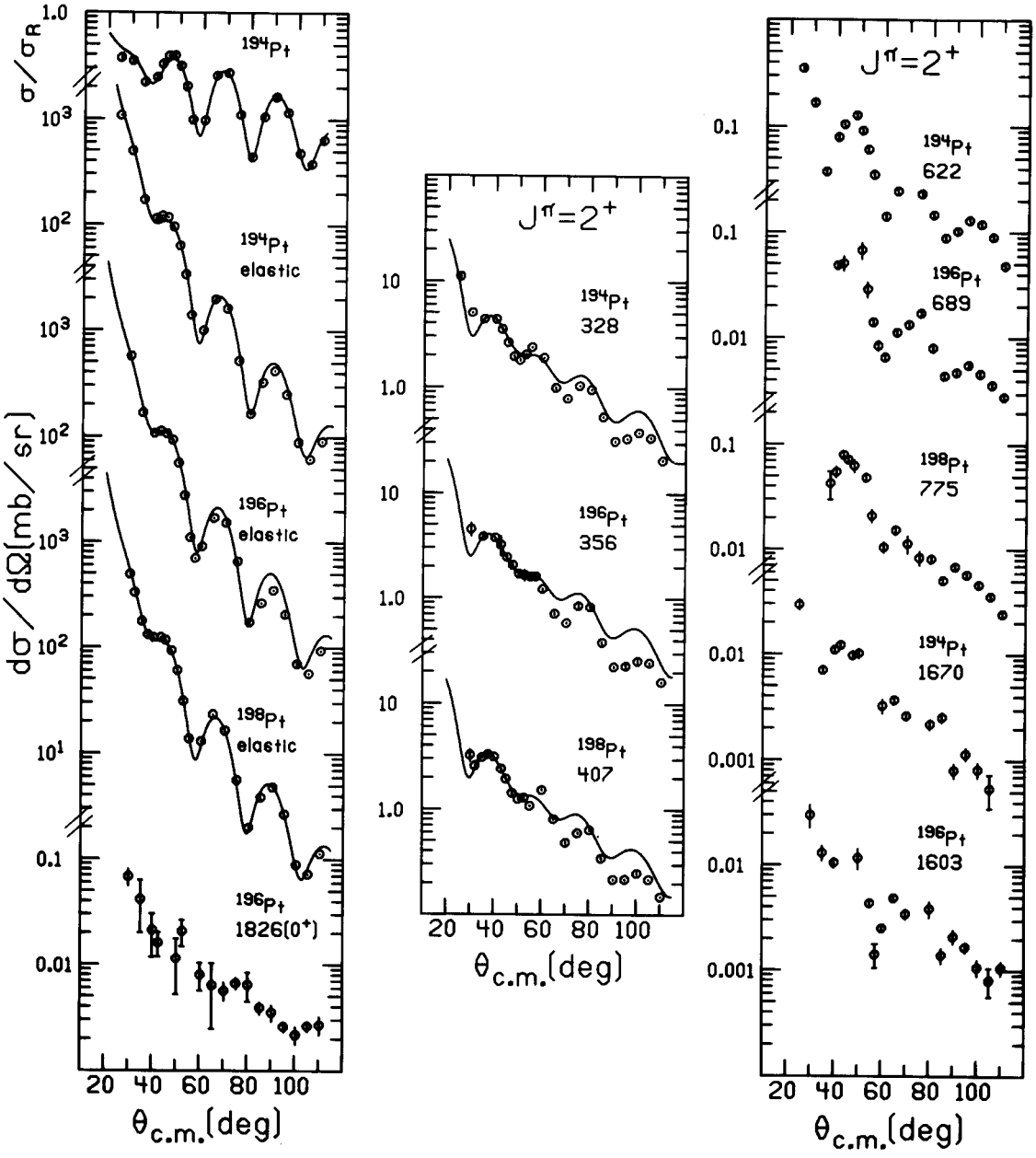
σ/σR
dσ/dΩ(mb/sr)
194Pt
194Pt elastic
196Pt elastic
198Pt elastic
196Pt 1826(0+)
θc.m.(deg)
Jπ=2+
194Pt 328
196Pt 356
198Pt 407
θc.m.(deg)
Jπ=2+
194Pt 622
196Pt 689
198Pt 775
194Pt 1670
196Pt 1603
θc.m.(deg)

Figure VI-1.

where Z_1 and Z_2 are the atomic masses of the target and projectile, E is the energy of the projectile, and θ is the center of mass scattering angle. The large deviation from unity is evidence for the influence of nuclear forces in the scattering process, which produce an optical-like diffraction pattern.

In ^{194}Pt the two states at 1.547 and 1.892 MeV may be the well-known 0^+ states seen in several decay studies and in the (p,t) reaction study described in Chapter V. Unfortunately these states are only weakly populated, and are not clearly resolved from nearby states in the wire counter data, so no angular distributions could be extracted. A level is seen at 1.826(3) MeV in ^{196}Pt which may be the known [Ci 79, De 79] 0^+ state at 1.823 MeV. An angular distribution was extracted for this level (see Figure VI–1), however no definite spin assignment could be made due to a lack of any characteristic L = 0 shape.

2. L = 2 Transitions

A total of eight known 2^+ levels were populated in the three reactions, and in each case an angular distribution was obtained. Two different shapes were seen for the L = 2 angular distributions in the (p,p') reactions: one for transitions populating the first 2^+ level (K = 0), and another, having more structure, for the second 2^+ (K = 2) and higher-lying 2^+ levels. The angular distributions (Figure VI–1) of the 0.328 MeV level in ^{194}Pt, the 0.355 MeV

level in ^{196}Pt, and the 0.407 MeV level in ^{198}Pt all display only a mildly oscillatory shape, while the 0.622 MeV level in ^{194}Pt, the 0.689 MeV level in ^{196}Pt, and the 0.775 MeV level in ^{198}Pt exhibit more pronounced oscillations. However, the shape of the transition populating the 0.775 MeV level in ^{198}Pt shows substantially fewer oscillations than those for ^{194}Pt or ^{196}Pt. This may be the result of the decreasing deformation as A increases. This is observable in the angular distributions for the first 2^+ states populated in (p,p') scattering at 35 MeV on rare-earth nuclei [Ki 78]. There, $\beta_2 \geq 0.23$, and the shapes display even more diffractive shapes than the 2_2^+ states seen here.

The assignment of a spin and parity of 2^+ for the 1.603 MeV level in ^{196}Pt supports the assignment made in the (p,t) study discussed in Chapter V.

3. L = 3 Transitions

States with $J^\pi = 3^-$ were very strongly excited at 1.433 MeV in ^{194}Pt, 1.447 MeV in ^{196}Pt, and 1.682 MeV in ^{198}Pt. The shape of the angular distributions for these states is very characteristic (see Figure VI–2) and thus enabled the assignment of the 1.682 MeV level in ^{198}Pt as the 3^- state. A state has been reported [Ba 76] at 1.722 MeV in ^{198}Pt(α,α') and tentatively assigned as 3^-, however the energies determined in [Ba 76] are systematically too high for most of the levels populated in ^{198}Pt as well as in ^{194,196}Pt. This is particularly true for the 3^- states in

Figure VI-2. L = 3, 4 Angular Distributions Seen in the ^{194,196,198}Pt(p,p') Reactions. Energies are given in keV.

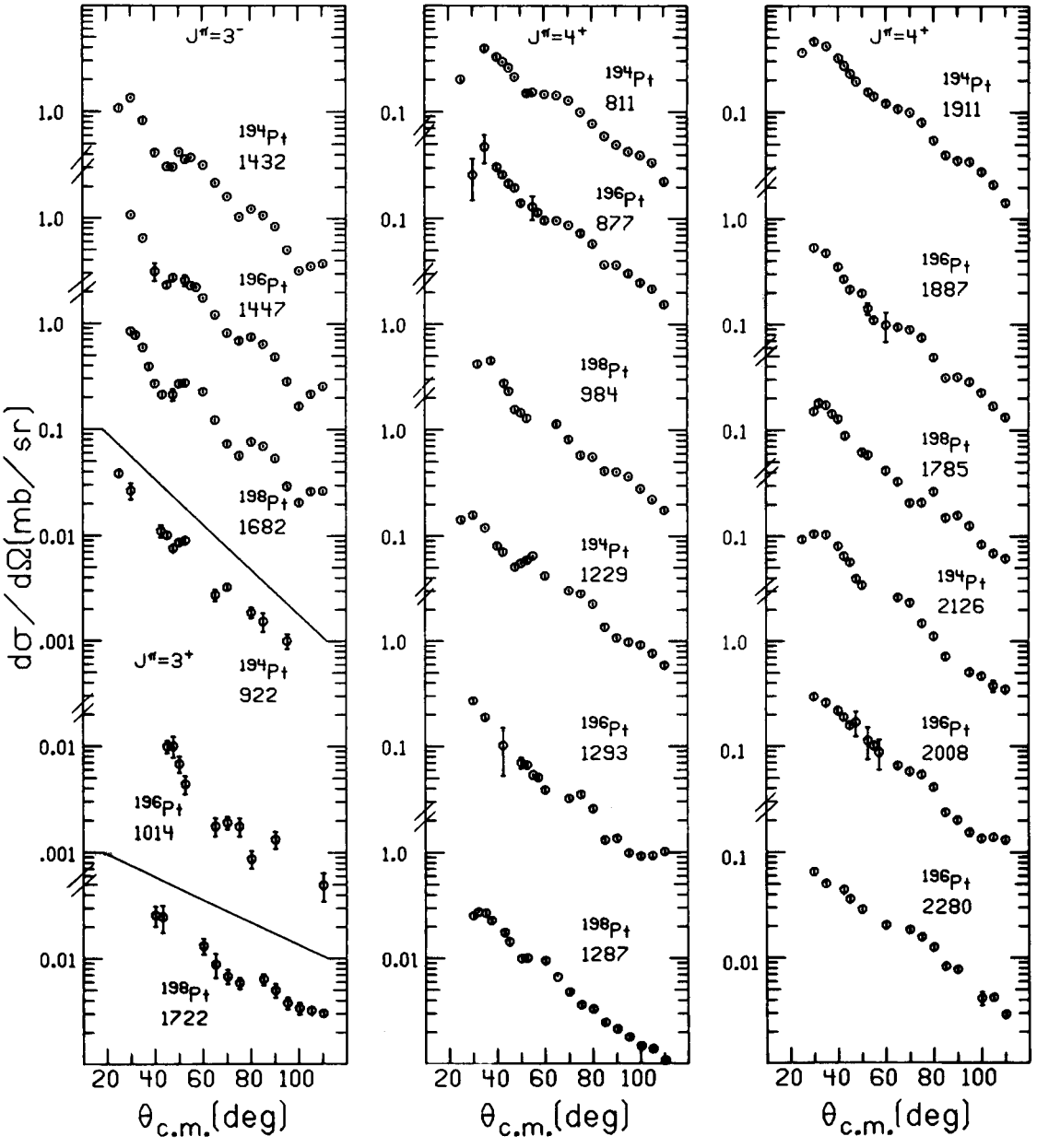
Jπ=3⁻
194Pt
1432
196Pt
1447
198Pt
1682
Jπ=3⁺
194Pt
922
196Pt
1014
198Pt
1722
Jπ=4⁺
194Pt
811
196Pt
877
198Pt
984
194Pt
1229
196Pt
1293
198Pt
1287
Jπ=4⁺
194Pt
1911
196Pt
1887
198Pt
1785
194Pt
2126
196Pt
2008
196Pt
2280
dσ / dΩ(mb/sr)
θc.m.(deg)
20 40 60 80 100

Figure VI-2.

each reaction. Figure VI–2 includes the angular distribution for a 1.722 MeV level only weakly populated in the (p,p') reaction. The difference in strength of this level and the known 3^- states in $^{194,196}Pt$ is a factor of 20. Although a definite assignment cannot be made for the 1.722 MeV level, the shape of the angular distribution for the 1.682 MeV level supports its assignment as the lowest 3^- state.

Two unnatural parity 3^+ states are also seen in two of the reactions studied. Both states, 0.922 MeV in ^{194}Pt and 1.014 MeV in ^{196}Pt, are populated very weakly and thus complete angular distributions were not possible due to background from large impurity peaks (oxygen, carbon, and silicon). The partial angular distributions have been included in Figure VI–2 to illustrate their low cross section. A possible 3^+ level was also seen in ^{198}Pt at 1.246 MeV, however, this assignment is based on systematics and tentative agreement with recent (n,n') data [Ya 79] since a full angular distribution was not obtained. Unnatural parity states have no direct excitation mechanism via inelastic scattering unless a tensor component is included in the nuclear potential, but may be populated by several multiple excitation routes, which explains the weak cross section.

4. L = 4 Transitions

At least three states with $J^\pi = 4^+$ were populated in each reaction. Each displays a similar although rather

structureless angular distribution. The various transitions are shown in Figure VI–2. The major characteristics of the L = 4 transitions are a gradual decrease in strength towards backward angles, a slight plateau at 60^{o}, and a forward peak near 35^{o}. In ^{194}Pt four 4^{+} states are seen and identified. Two of these, at 0.811 MeV and 1.229 MeV, were known from previous studies, while the level at 1.911 MeV was first seen in the (p,t) study (Chapter V). The state at 2.126 MeV is tentatively assigned 4^{+} and agrees with the assignment made in the (p,t) study.

In ^{196}Pt, five states with $J^{\pi} = 4^{+}$ were observed, including two previously known at 0.876 and 1.293 MeV. A third, at 1.887 MeV, may be the same state seen in the ^{198}Pt(p,t)^{196}Pt reaction (see Table V–3) although the energy is 3 keV higher for the state seen in the proton scattering (the energy uncertainties are about 2 keV for each level). Two additional 4^{+} states have been tentatively assigned at 2.008 and 2.280 MeV. These states may also have been observed in the (p,t) study.

Three states in ^{198}Pt have been assigned $J^{\pi} = 4^{+}$, including the one known 4^{+} seen at 0.984 MeV in this study and at 0.991 MeV in (α,α') [Ba 76]. A state seen at 1.287 MeV is also assigned as 4^{+} and is probably the same state seen at 1.305 MeV in the (α,α') study [Ba 76]. The third 4^{+} in ^{198}Pt is at 1.785 MeV excitation. This state completes a series of 4^{+} states seen at $\simeq$ 1.8 to 1.9 MeV in $^{192-198}$Pt in both the (p,t) and (p,p') reactions. The nature

of these states is unknown, but their strength in the inelastic proton scattering may indicate a considerable hexadecapole component (see Chapter V).

5. Transitions with $L \geq 5$

Five L = 5 transitions have been assigned on the basis of the empirical shape (Figure VI–3) for the angular distribution populating the probable 5^- state at 1.374 MeV in ^{194}Pt. The 5^- state seen in ^{196}Pt at 1.270 MeV was previously assigned [Ja 68] as $(4,5)^-$ but the (p,t) study (Chapter V) prefers 5^-. A new level at 1.367 MeV in ^{198}Pt, seen for the first time, is assigned as (5^-) on the basis of its shape and level energy systematics. The remaining two assignments (both tentative) were made in ^{194}Pt for levels at 1.932 and 2.165 MeV.

Only one angular distribution (Figure VI–3) was obtained for a level known to have $J^\pi = 6^+$, the 1.412 MeV level in ^{194}Pt. The error bars are quite large at most angles because of the weak population of the 6^+ state and the proximity of the very strongly populated 3^- level at 1.432 MeV. No attempt was made to extract an angular distribution for the 6^+ level in ^{196}Pt because the strongly populated 3^- level is only 17 keV away.

Angular distributions are obtained for levels seen at 1.485 MeV in ^{194}Pt and 1.374 MeV in ^{196}Pt (Figure VI–3). The level at 1.485 MeV in ^{194}Pt was previously known from in-beam γ–decay studies [Ya 74] to have $J^\pi = 7^-$, thus affording an

Figure VI-3. $L \geq 5$ Angular Distributions Seen in the $^{194,196,198}Pt(p,p')$ Reactions. Also shown in the third and fourth column are angular distributions with a unique but unidentifiable shape. Energies are given in keV.

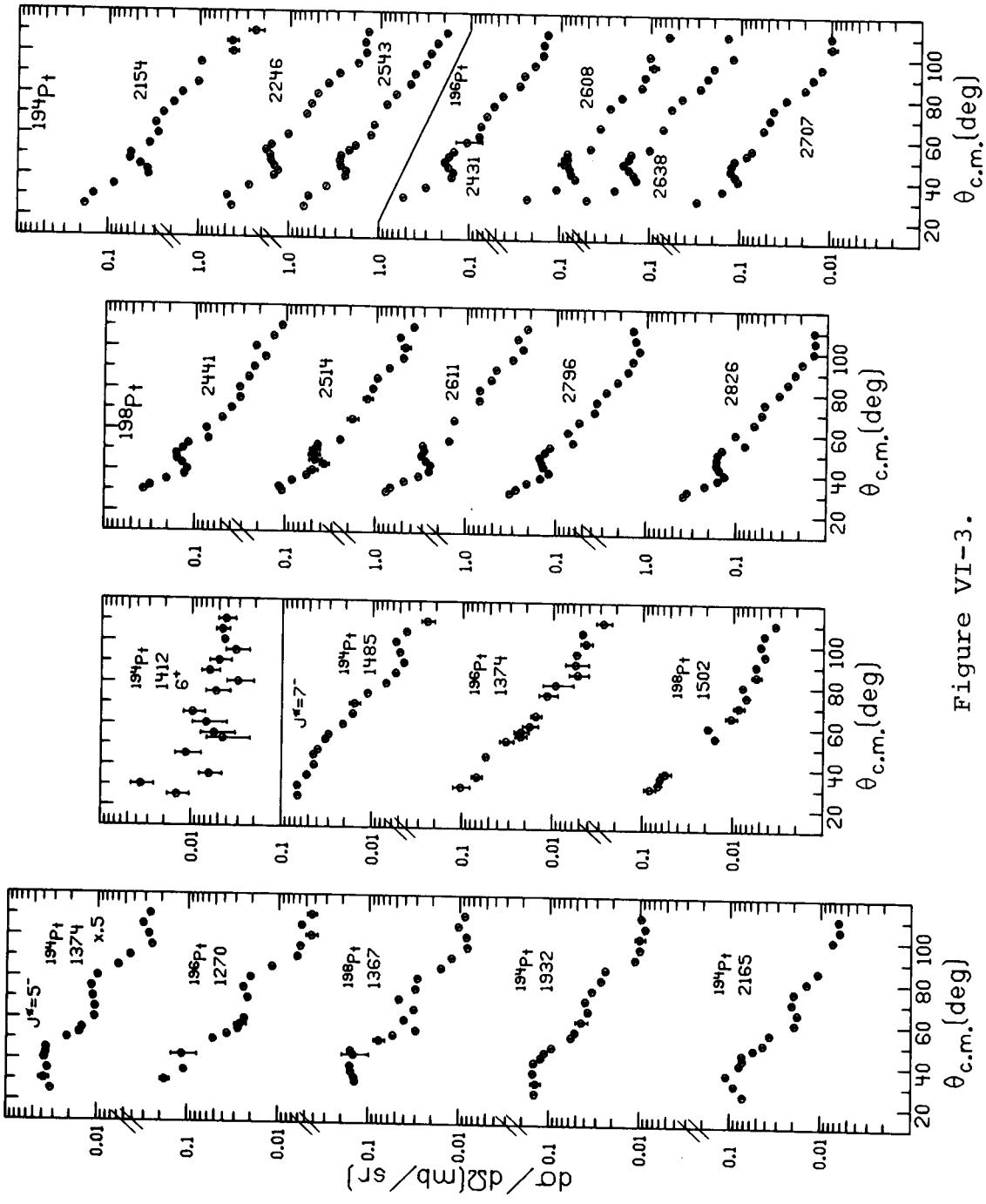
dσ/dΩ(mb/sr)
θc.m.(deg)
194Pt
1374
x.5
Jπ=5−
196Pt
1270
198Pt
1367
194Pt
1932
194Pt
2165
194Pt
1412
6+
Jπ=7−
194Pt
1485
196Pt
1374
198Pt
1502
198Pt
2441
2514
2611
2796
2826
194Pt
2154
2246
2543
196Pt
2431
2608
2638
2707

Figure VI-3.

empirical shape for comparison in the ^{196,198}Pt(p,p') reactions. The level at 1.374 MeV in ^{196}Pt had been previously assigned as $(6^+,7^-)$, but its angular distribution has the shape for $J^\pi = 7^-$. A tentative assignment of $(6^+,7^-)$ has also been made for the level at 1.502 MeV in ^{198}Pt. The level at 1.722 MeV in ^{198}Pt oculd not be given a definite assignment because of its weak population and uncharacteristic shape.

Figure VI-3 includes twelve seemingly unique angular distributions, three from ^{194}Pt, four from ^{196}Pt, and five from ^{198}Pt, all with essentially the same distinctive features. The most prominent of these is a peak at 50^o on a gradually sloping curve. This shape is seen for transitions populating various new levels from 2.1 to 2.8 MeV of excitation, and in each case the transition is one of the strongest in the reaction. Unfortunately there are no known levels in any of the reactions with a similar shape, so no spin information can be obtained. However, the strength of these transitions and their high excitation energy (approximately 1 MeV above the pairing gap, $\simeq$ 1.4 MeV) may indicate these states are composed of highly correlated, particle-hole configurations. Further investigation is needed, though, before a definite characterization of these states can be made.

Several additional angular distributions are shown in Figure VI-4. No spin assignments were made for these transitions due to the lack of any similar empirical shape or

Figure VI-4. Angular Distributions Seen in the ^{194,196,198}Pt(p,p') Reactions With Unknown L Transfer. Energies are given in keV.

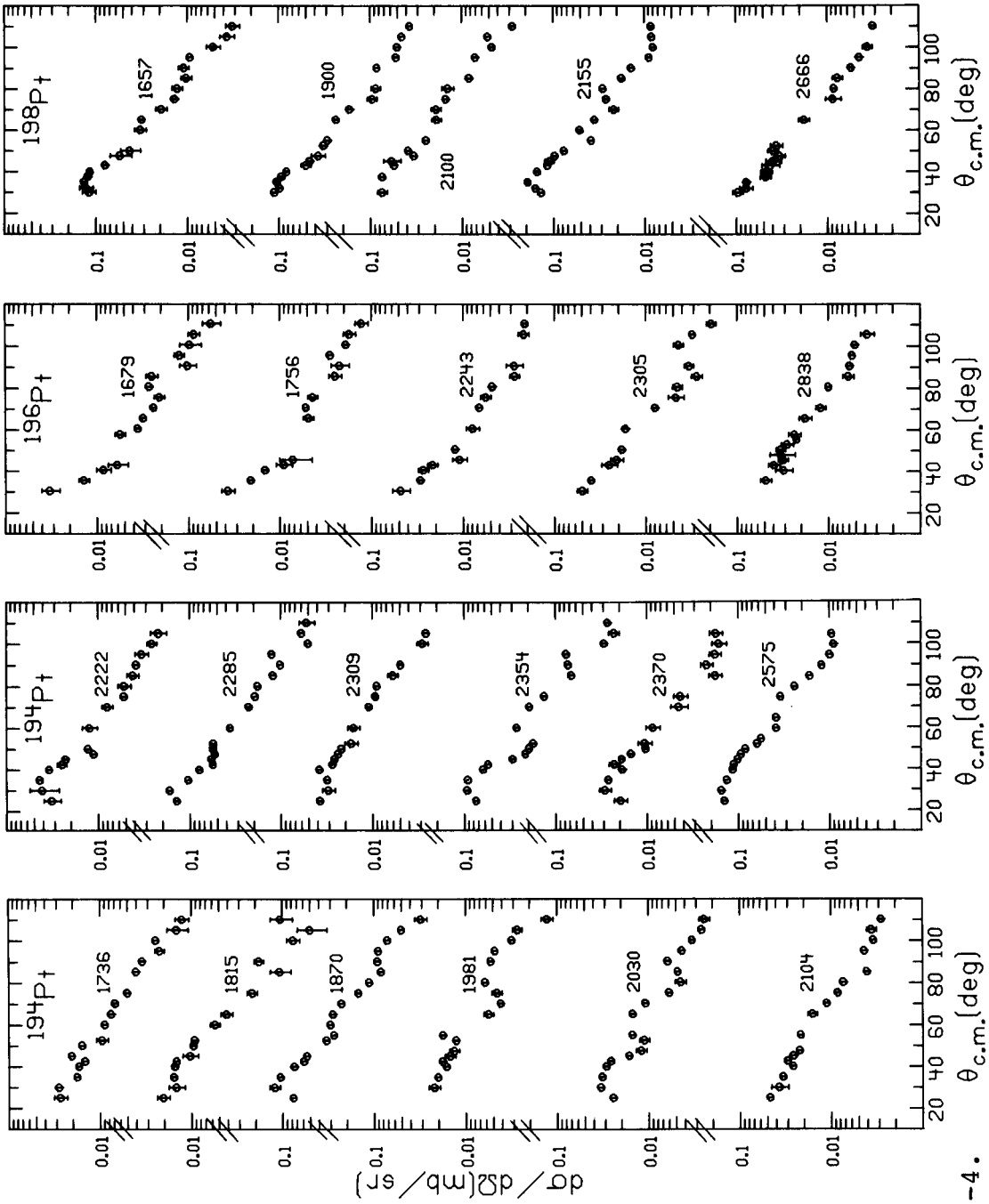
194Pt
1736
1815
1870
1981
2030
2104
194Pt
2222
2285
2309
2354
2370
2575
196Pt
1679
1756
2243
2305
2838
198Pt
1657
1900
2100
2155
2666
dσ/dΩ(mb/sr)
θc.m.(deg)
0.01
0.1
20 40 60 80 100

Figure VI-4.

because of large uncertainties in the angular distribution data.

B. Coupled Channel Analysis of the Inelastic Scattering Data

1. Introduction

Attempts to describe the inelastic scattering data with the one-step DWBA were not very successful. Only the shape of the first 2^+ angular distribution for the three reactions could be reproduced by the DWBA calculations (see Figure VI-1). Since there is only one form factor for a given L-transfer in the collective model approach, there is no means to account for the dramatically different 2_2^+ angular distribution. Hence, these limitations of the DWBA formalism suggest that a more complete and complex coupled channels approach is necessary if one is interested in studying the higher energy states of the Pt nuclides.

The procedures used in this study for the coupled channel analysis are very similar to those employed for the analysis of proton scattering from well-deformed nuclei [Ki 79]. Basically this method involves an iterative searching procedure to determine the best set of optical model parameters for reproducing the elastic scattering data. Next the deformation parameters, β_λ, are determined for the ground band by a similar searching procedure, where a "best fit" is obtained for the inelastic data as well as the

elastic. Both of these searches are performed with the coupled channel code ECIS [Ra 73], which is capable of carrying out a grid or gradient-type search.

Additionally, the effects of several other features of the data and theory were investigated, such as spin-orbit effects, the coupling of the "γ-band", the choice of matrix elements, and the effect of β_6 on the extraction of β_2 and β_4. The details of these effects will be discussed later in this chapter. Two additional aspects of this analysis will be addressed: the use of matrix elements derived from the IBA model to describe the coupling between the nuclear states, and a comparison of the charge component of the nuclear moments extracted in the analysis with those previously determined by other methods.

2. The Optical Model Analysis

The usual starting point of a DWBA or full coupled channel calculation is the determination of the best set of parameters for the optical potential which will reproduce the experimental elastic scattering. In this study the shape of the potential was assumed to be the standard Woods-Saxon form (as described in Chapter III.B.3) with the deformation parameterized via the expansion

$$R = R_o \left[1 + \sum_\lambda \beta_\lambda Y_\lambda^o(\theta,\phi) \right] , \qquad \text{(VI-1)}$$

and the Coulomb part of the potential is derived from a deformed uniform charge distribution with a sharp cutoff

$$V_c = Z_1 Z_2 \, e^2/r \qquad \text{for } r > R_c$$

$$V_c = \frac{Z_1 Z_2 \, e^2}{2R_c}\left[3 - \left(\frac{r}{R_c}\right)^2\right] \qquad \text{for } r < R_c \,, \tag{VI-2}$$

where R_c, the Coulomb radius, is expressed in terms of the charge deformation parameters (β_λ^c) and spherical harmonics shown above. Thus, in practice, for proton scattering there are eleven optical model parameters that could be included in a search: V, W, W_D, V_{SO}, r_R, r_I, r_{SO}, r_c, a_R, a_I, and a_{SO}, plus several deformation parameters, β_λ^N and β_λ^c. The procedure used in this study for determining the optical parameters limited the number of parameters to be varied to V, W_D, V_{SO}, a_R, and a_I (defined in Table V-4 and listed in Table VI-2), to simplify the searching process and avoid well-known ambiguities [Au 70]. However, the parameters held constant throughout the searches were not chosen arbitrarily. The radius parameters were not included since in this deformed optical model potential (DOMP) they enter the potential as a product with their respective deformation parameters. The Coulomb parameters, r_c, β_2^c, β_4^c, were taken from Reference [Ba 76]. The imaginary well depth was held constant primarily for simplification.

The optimum parameters were determined by use of the automatic searching features in ECIS by minimizing

$$\chi^2_{g.s.} = \sum_i^N \left(\sigma_{th}(\theta_i) - \sigma_{exp}(\theta_i)\right)/\Delta\sigma_{exp}(\theta_i)^{\,2} \tag{VI-3}$$

where $\sigma_{exp}(\theta_i)$ is the measured, and $\sigma_{th}(\theta_i)$ the calculated differential cross section at angle θ_i, and $\Delta\sigma_{exp}$ is the

Table VI-2. Optical Model Parameters Used in E.C.I.S. Calculations.

Nuclide	V^a (MeV)	a_R (fm)	W_D (MeV)	a_I (fm)	V_{SO} (MeV)	χ^2/N (ground state)
^{194}Pt						
L*S:						
κ=0.0375 keV	53.40	0.712	4.70	0.663	6.497	7.0
κ=0.5375 keV	53.12	0.723	4.82	0.658	6.466	8.6
L*S = 0:						
κ=0.0375 keV	51.84	0.659	8.13	0.594	0.0	14.3
κ=0.5375 keV	51.64	0.656	7.99	0.604	0.0	15.1
^{196}Pt						
L*S	51.78	.786	5.46	0.666	6.551	17.1
L*S = 0	50.79	.734	7.86	0.644	0.0	29.9
^{198}Pt						
L*S	53.35	0.709	4.72	0.667	6.475	5.5
L*S = 0	52.53	0.624	7.60	0.611	0.0	10.2

[a] The β_λ^c and r_c values are taken from [Ba 76]. All radii were held constant, r_R = 1.17 fm, r_I = 1.32 fm, r_{SO} = 1.01 fm, and r_c = 1.2 fm. Also, the spin-orbit and diffuseness, a_{SO}, was held constant (1.01 fm), and W retained the Becchetti-Greenlees value, 5.1 MeV for ^{194}Pt and 5.0 MeV for $^{196,198}Pt$.

error associated with σ_{exp}. An error of ± 3% was added in quadrature with the statistical errors from the peak fitting routine to account for uncertainties in relative normalization. The overall normalization of the data, N, was also varied to minimize χ^2 where

$$\chi^2_{g.s.} = \sum_i^N [(N\sigma_{th} - \sigma_{exp})/\Delta\sigma_{exp}]^2 + [(N - N^x)\Delta N^x]^2 , \quad \text{(VI-4)}$$

where N^x and ΔN^x are the estimated value for the normalization and the approximate error in N^x to reduce the range of variation of N. Since the absolute normalization was not known (an approximate value was obtained from target thickness values determined from the (p,t) study), this feature of ECIS was used during the optical model parameter searches and the final value was used in computing the cross sections for the (p,p') reactions in Tables V-2, V-3, and VI-1. ECIS was used for these searches because of the need to include inelastic channels for non-spherical nuclei when calculating the elastic scattering. This allows one to account for flux usually absorbed by the imaginary part of the potential. In these searches a $0^+-2^+-4^+$ level space was used which includes the couplings shown in Figure VI-5a.

The parameter search was conducted by simultaneously varying either the three potential depths or both the diffuseness parameters. This avoided well-known ambiguities such as $W_D - a_I$. The sequence of searches used for each

Figure VI-5. Coupling Schemes Used in the Coupled Channels Calculations.

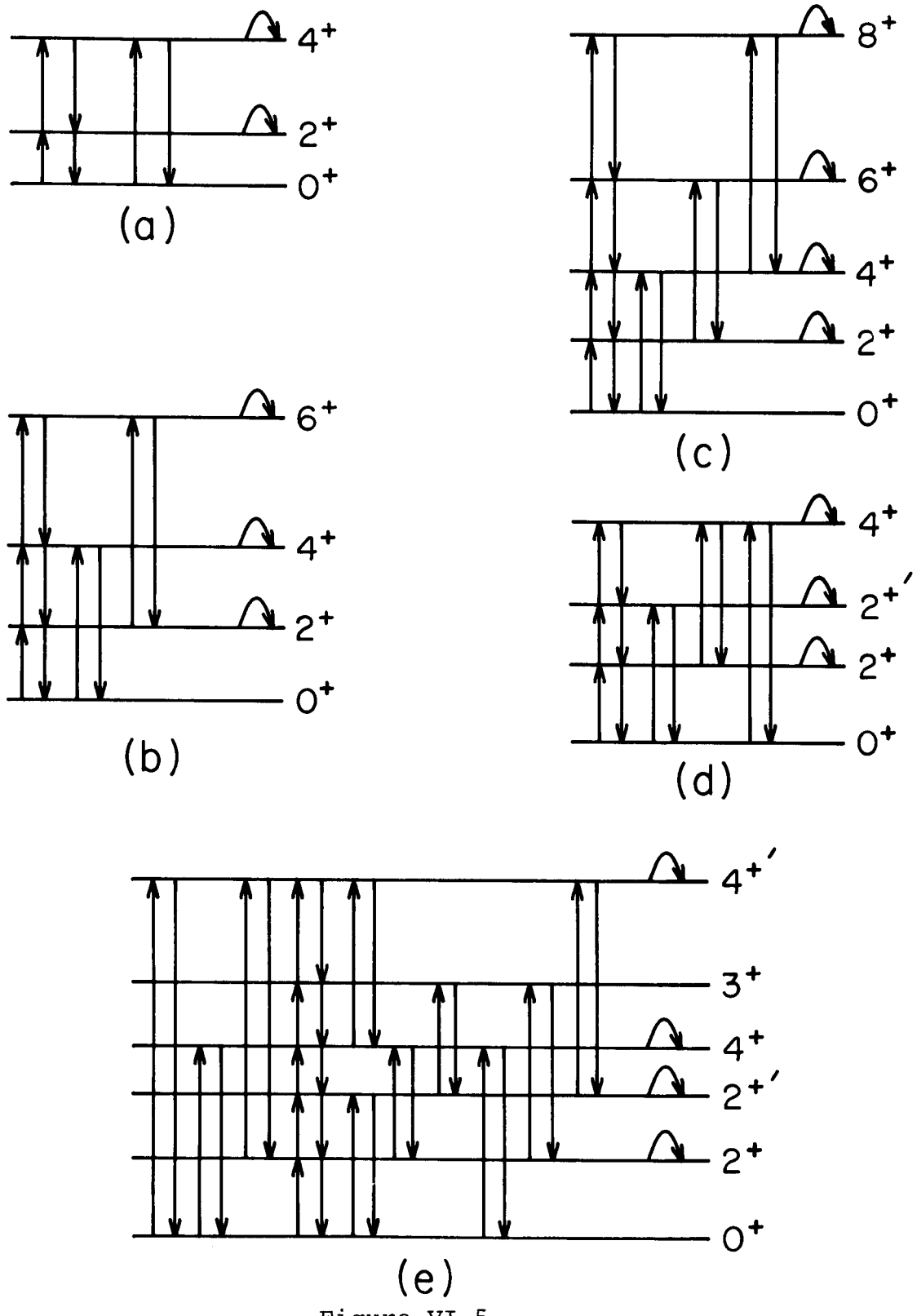

Figure VI-5.

nucleus typically involved two iterations of a potential search followed by a search on the diffuseness parameters, one search on the deformation parameter, β_2, while minimizing $\chi^2_{2^+}$, then two more iterations on (V, W_D, V_{SO}) and (a_R, a_I). The search methods employed in ECIS are a "grid search" for a one variable search and a "gradient search" for two or more variables [Be 69a, Ra 72]. For ^{196}Pt the starting β_λ^N values have been $\beta_\lambda r$-scaled from values in [Ba 76], while for ^{194,198}Pt the initial values for the β_λ^N are those which produce the same quadrupole and hexadecapole moment as the β_λ^N's of Reference [Ba 76]. The initial relative values for the matrix elements used for the optical model searches are shown in Table VI-3. The Coulomb and nuclear matrix elements are assumed to have the smae relative values, although each set is normalized to a different $0^+ \rightarrow 2^+$ and $0^+ \rightarrow 4^+$ matrix element. These values are determined in ECIS from the deformation parameters by evaluating the integral

$$M(E\lambda,\ 0^+ \rightarrow L^+) = i^L \frac{3ZR^L}{4\pi(L+3)} \int \left(1 + \sum_\lambda \beta_\lambda Y_\lambda^o\right)^{L+3} Y_L^o d\Omega \ , \qquad \text{(VI-5)}$$

where R and β_λ can be the nuclear or Coulomb values. For each nucleus, previously measured matrix elements were used when available, otherwise values were taken from the axially symmetric rotational model for a K = 0 band. All the calculations described in this and the following sections have been performed using 25 partial waves, an integration

Table VI-3. Relative Matrix Elements, $\langle f||M(E\lambda)||i\rangle$, Used for Initial Optical Model Searches.

		^{194}Pt		^{196}Pt		^{198}Pt	
|i>	|f>	E2	E4[a]	E2	E4[a]	E2	E4[a]
0^+	2^+	-1.0		-1.0		-1.0	
0^+	4^+		1.0		1.0		1.0
2^+	2^+	-0.637[b]	1.195	-0.657[c]	1.195	-1.49[c]	1.195
2^+	4^+	-1.518	-1.140	-1.570[d]	-1.140	-1.604	-1.140
4^+	4^+	0.815	1.207	1.529	1.207	1.529	1.207

[a] E4 values are from symmetric rotational model.

[b] Reference [Ba 76].

[c] Reference [Gl 69].

[d] Reference [Mi 71]; remaining E2 values are from symmetric rotational model.

step size of ≃ 0.33 fm, and a matching radius of 20.0 fm. The multipole expansion (Equation (III–53)) included couplings of $\lambda = 2$ and $\lambda = 4$ terms to $L = 8$. For simplicity, the nuclear deformations were equal for each portion of the potential.

The results of the optical model parameter searches are given in Table VI–2 for a potential with a full Thomas form [Au 70] for the spin-orbit term (L*S), and one without (L*S = 0). Also reported are the values of chi-squared-per-point for the ground state, χ^2/N, which is a measure of the "goodness of the fit", and is used for comparison purposes. The changes in the parameters from the initial Becchetti-Greenlees parameters are relatively small except for the real diffuseness, a_R, and the imaginary surface term, W_D, which decreases ≃ 7% and ≃ 12%, respectively. There do appear to be some problems with the parameters for ^{196}Pt with spin-orbit as the changes in V, a_R, and W_D do not follow the trends seen in ^{194,198}Pt. This is also reflected in the χ^2/N value, 17.1, which is almost three times the value for ^{194}Pt and ^{198}Pt. The cause for this apparent discrepancy is unknown, although a more detailed grid search on V and a_R may be necessary to bring the values more in line with the other two nuclides. The overall effect of these difficulties has a very minor influence on the moments extracted as noted in a later section. Changes in the optical model parameters should be expected, because the Becchetti-Greenlees parameters are an average set of parameters for spherical

nuclei. However, since the Pt nuclei are only slightly deformed ($\beta_2 \simeq -.15$), the couplings introduced in the searching procedure should result in only minor adjustments of the values, as was seen for most of the paraemters.

3. The Extraction of Deformation Parameters

Once a set of "best fit" optical model parameters is obtained, attention can be focused on the extraction of deformation parameters of the nuclear potential. At this juncture one may input all previously measured matrix elements, with the remaining values taken from a collective model, then vary the β_λ's and several of the more crucial, previously unmeasured matrix elements to fit the inelastic data, or, one may use a complete set of matrix elements taken from some nuclear model and fit the data by varying only the β_λ's. This study follows the second approach for several reasons. Since relatively little is known about the matrix elements which connect the low-lying states of the Pt nuclides (except ^{194}Pt [Ba 78a]), one is forced to work with some model to make predictions for these matrix elements. This provides a special opportunity to stringently test the predictive qualities of a model rather than comparing energy levels and a few E2 matrix elements. With the recent success of the O(6) limit of the IBA in the Pt–Os region for energy levels, E2 branching ratios [Ci 78, Ca 78], and (p,t) strengths (Chapter V) [De 79], the CC-analysis would provide a natural framework for further testing the E2 and E4 matrix

elements. This approach may not result in the best overall fit to the data, but one can judge the effectiveness of a complete set of matrix elements in describing the data rather than a partial set with uncertain significance.

The matrix elements used in the following analysis were obtained from the IBA code, PHINT [Sc 77], which was modified to output matrix elements rather than B(Eλ) values. The O(6) parameters used as input to PHINT (see Equation (II-42)) are taken from Reference [Ca 78] and listed in Table VI-4. The values used in the ^{198}Pt calculation have been extrapolated by extending the prescribed [Ca 78] relationships: A is held constant, B and C are varied linearly with mass, and κ, the strength of the quadrupole-quadrupole interaction between the bosons, is varied logarithmically with mass. Casten and Cizewski [Ca 78] point out that the transition rates are really only sensitive to the ratio κ/B, which specifies the location of the nucleus relative to the O(6) or rotor limits, so the actual value of the individual parameters is not critical. The calculated matrix elements are shown in Tables VI-5, 6, 7, and 8. The values listed in Table VI-6 were calculated with a larger value of κ (= 0.5375 keV). Calculations using these matrix elements will be discussed in the next section.

The results of the CC-analysis of the states in the ground band (up to the 6^+ state) for ^{194,196,196}Pt are shown in Figures VI-6, VI-7, and VI-8 as the solid line fits.

Table VI-4. IBA Parameters Used in the Perturbed O(6) Calculations. A, B, and C are the coefficients of Equation (II–40) and κ is the strength of the quadrupole-quadrupole interaction. N is the total number of bosons for each nucleus.

Nucleus	N	A (keV)	B (keV)	C (keV)	κ (keV)	κ/B
^{194}Pt						
Set 1	7	186	42.0	17.5	0.0375	0.0009
Set 2	7	186	42.0	17.5	0.5375	0.0128
^{196}Pt	6	186	43.0	19.0	0.025	0.0006
^{198}Pt	5	186	43.5	20.5	0.016	0.0004

Table VI-5. Relative Eλ IBA Matrix Elements for ^{194}Pt Calculated Using O(6) Symmetry and κ = 0.0375 keV.

$\|i\rangle$	$\|f\rangle$	$\langle f\|\|M(E2)\|\|i\rangle^a$	$\langle f\|\|M(E4)\|\|i\rangle^a$
0^+	2^+	-1.0	
0^+	2^+_2	0.0046	
0^+	4^+		1.0
0^+	4^+_2		-0.00267
2^+	2^+	-0.0142	1.380
2^+	2^+_2	-1.156	-0.00370
2^+	4^+	1.551	-0.0152
2^+	3^+	-0.0061	0.559
2^+	4^+_2	0.0011	0.818
2^+	6^+		-1.426
2^+_2	2^+_2	0.0142	0.656
2^+_2	4^+	-0.0029	-1.721
2^+_2	3^+	-1.186	-0.00359
2^+_2	4^+_2	-1.152	-0.0152
4^+	4^+	-0.0127	0.0878
4^+	3^+	0.750	-0.00399
4^+	4^+_2	1.098	-0.00572
4^+	6^+	-1.913	0.0130
4^+	8^+		-1.622
3^+	3^+		-1.767
3^+	4^+_2	0.00742	-0.748

Table VI-5.(cont'd.).

$\|i\rangle$	$\|f\rangle$	$\langle f\|\|M(E2)\|\|i\rangle^a$	$\langle f\|\|M(E4)\|\|i\rangle^a$
3^+	6^+		-1.452
4_2^+	4_2^+	0.00694	1.525
6^+	6^+	-0.0101	0.965
6^+	8^+	2.120	-0.011
8^+	8^+	-0.00752	1.133

[a]Matrix elements calculated with program PHINT [Sc 77].

Table VI-6. Relative Eλ IBA Matrix Elements for ^{194}Pt Calculated Using O(6) Symmetry and κ = 0.5375 keV.

|i>	|f>	<f||M(E2)||i>[a]	<f||M(E4)||i>[a]
0^+	2^+	-1.0	
0^+	2_2^+	0.0627	
0^+	4^+		1.0
0^+	4_2^+		0.0369
2^+	2^+	-0.196	1.376
2^+	2_2^+	-1.142	-0.0508
2^+	4^+	1.552	-0.209
2^+	3^+	-0.0838	0.557
2^+	4_2^+	-0.0155	-0.802
2^+	6^+		-1.425
2_2^+	2_2^+	0.196	0.659
2_2^+	4^+	-0.0397	1.269
2_2^+	3^+	-1.186	-0.0494
2_2^+	4_2^+	1.155	0.210
4^+	4^+	-0.175	0.883
4^+	3^+	0.0748	0.0551
4^+	4_2^+	-1.090	0.0787
4^+	6^+	-1.914	0.180
3^+	3^+		-1.765
3^+	4_2^+	0.103	0.744

Table VI-6 (cont'd.).

$\|i>$	$\|f>$	$<f\|\|M(E2)\|\|i>$ [a]	$<f\|\|M(E4)\|\|i>$ [a]
3^+	6^+		-1.446
4_2^+	4_2^+	0.0949	1.512
6^+	6^+	-0.141	0.969

[a] Matrix elements calculated with program PHINT [Sc 77].

Table VI-7. Relative E IBA Matrix Elements for ^{196}Pt Calculated Using O(6) Symmetry and κ = 0.025 keV.

$\|i\rangle$	$\|f\rangle$	$\langle f\|\|(ME2)\|\|i\rangle$	$\langle f\|\|M(E4)\|\|i\rangle$
0^+	2^+	-1.0	
0^+	2^+_2	0.00242	
0^+	4^+		1.0
0^+	4^+_2		-0.00131
2^+	2^+	-0.0073	1.436
2^+	2^+_2	-1.144	-0.0020
2^+	4^+	-1.535	0.0081
2^+	3^+	0.00314	-0.544
2^+	4^+_2	0.0006	0.797
2^+	6^+		-1.388
2^+_2	2^+_2	0.0073	0.694
2^+_2	4^+	0.0016	1.818
2^+_2	3^+	1.155	0.0017
2^+_2	4^+_2	-1.121	-0.00795
4^+	4^+	-0.0063	0.927
4^+	3^+	0.730	-0.0023
4^+	4^+_2	-1.069	0.0030
4^+	6^+	1.862	0.0069
3^+	3^+		1.901
3^+	4^+_2	-0.0064	0.804
3^+	6^+		1.564
4^+_2	4^+_2	0.0036	1.641
6^+	6^+	-0.0048	1.038

Table VI-8. Relative Eλ IBA Matrix Elements for ^{198}Pt Calculated Using O(6) Symmetry and κ = 0.016 keV.

|i>	|f>	<f||M(E2)||i>[a]	<f||M(E4)||i>[a]
0^+	2^+	1.0	
0^+	2^+_2	-0.00123	
0^+	4^+		1.0
0^+	4^+_2		-0.00060
2^+	2^+	-0.0035	1.521
2^+	2^+_2	-1.127	-0.0011
2^+	4^+	-1.512	0.00415
2^+	4^+_2	-0.00036	-0.763
2^+	6^+		-1.329
2^+_2	2^+_2	0.00353	0.751
2^+_2	4^+	0.00085	1.970
2^+_2	4^+_2	1.073	0.00398
4^+	4^+	-0.00295	1.004
4^+	4^+_2	1.024	-0.00156
4^+	6^+	1.783	-0.00346
4^+_2	4^+_2	0.00179	1.820
6^+	6^+	-0.00204	1.152

[a]Matrix elements calculated with program PHINT [Sc 77].

These calculations used the optical model parameters of Table VI–2 and the IBA matrix elements of Tables VI–5, 7, and 8. Figure VI–5b schematically shows all the couplings included in the calculations. These fits to the data were obtained by varying β_2 and β_4 simultaneously, while minimizing the total chi-squared χ^2_T, defined as the sum of the chi-squared for the ground state, 2^+, and 4^+. The χ^2 for the 6^+ angular distribution was not included in the calculations since the effect of the 8^+ couplings was not accounted for due to computer limitations. The absence of the β_6 term in the expansion of the nuclear surface has consequences for the determination of β_2 and β_4 that will be discussed in a later section.

Table VI–9 summarizes the deformation parameters and corresponding moments determined for ^{194,196,198}Pt. These moments have been calculated using the methods described in Section C of Chapter III. The negative values for both β_2 and β_4 are consistent with previous measurements [Ba 76] for the Pt nuclides and are in qualitative agreement with theoretical predictions of Reference [Go 72]. A negative value for β_2 also implies an oblate shape for the nucleus, which is consistent with the quadrupole measurements from Coulomb excitation studies.

The overall quality of the fits is quite good considering no matrix elements were varied in the search. The major problem appears in ^{196}Pt between 70^o and 90^o in the

Figure VI-6. Data and Coupled Channels Calculations for ^{194}Pt(p,p') With and Without the Spin-Orbit Interaction. The calculations included the couplings shown in Figure VI-5b, the matrix elements of Table VI-5, and DOMP parameters from Tables VI-2 and 9.

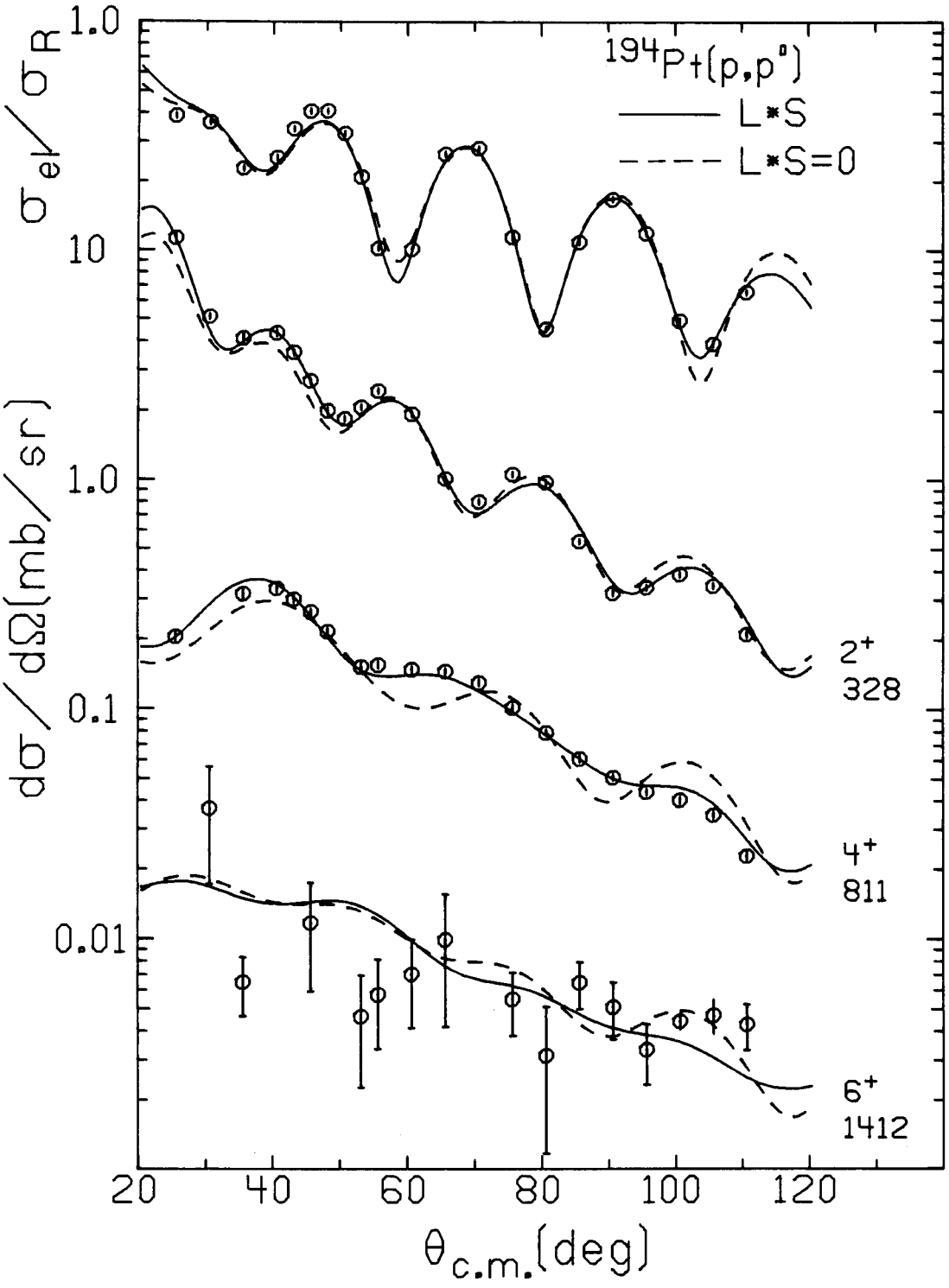
^{194}Pt(p,p')
L*S
L*S=0
2+
328
4+
811
6+
1412
dσ / dΩ(mb/sr)
σel / σR
1.0
10
1.0
0.1
0.01
20
40
60
80
100
120
θc.m.(deg)

Figure VI-6.

Figure VI-7. Data and Coupled Channels Calculations for ^{196}Pt(p,p') With and Without the Spin-Orbit Interaction. The calculations included the couplings shown in Figure VI-5b, the matrix elements of Table VI-7, and DOMP parameters from Tables VI-2 and 9.

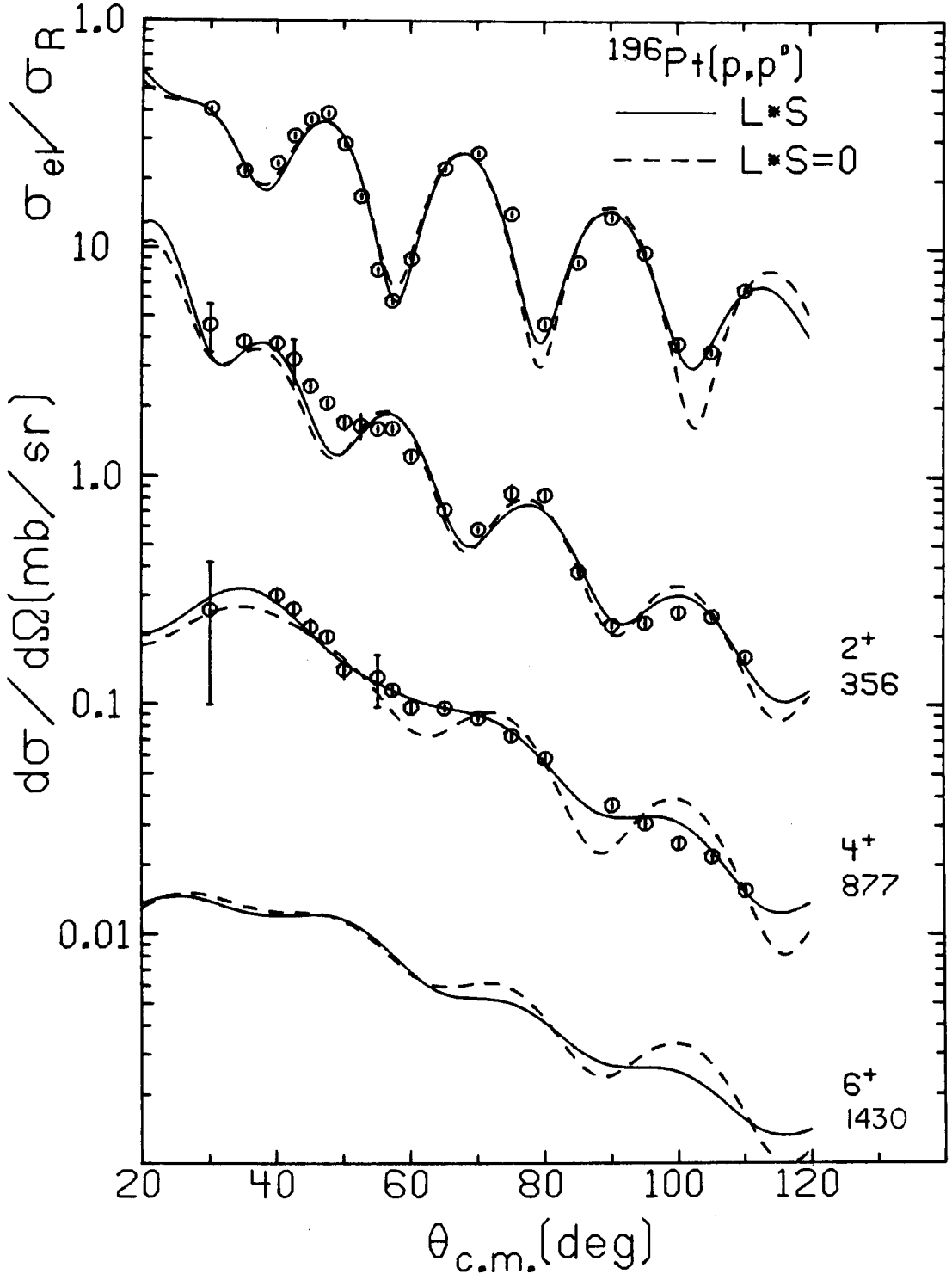
σ_{el}/σ_R
1.0
10
1.0
0.1
0.01
$d\sigma/d\Omega$[mb/sr]
^{196}Pt(p,p')
L*S
L*S=0
2+
356
4+
877
6+
1430
20
40
60
80
100
120
$\theta_{c.m.}$[deg]

Figure VI-7.

Figure VI-8. Data and Coupled Channels Calculations for ^{198}Pt(p,p') With and Without the Spin-Orbit Interaction. The calculations included the couplings shown in Figure VI-5b, the matrix elements of Table VI-8, and DOMP parameters from Tables VI-2 and 9.

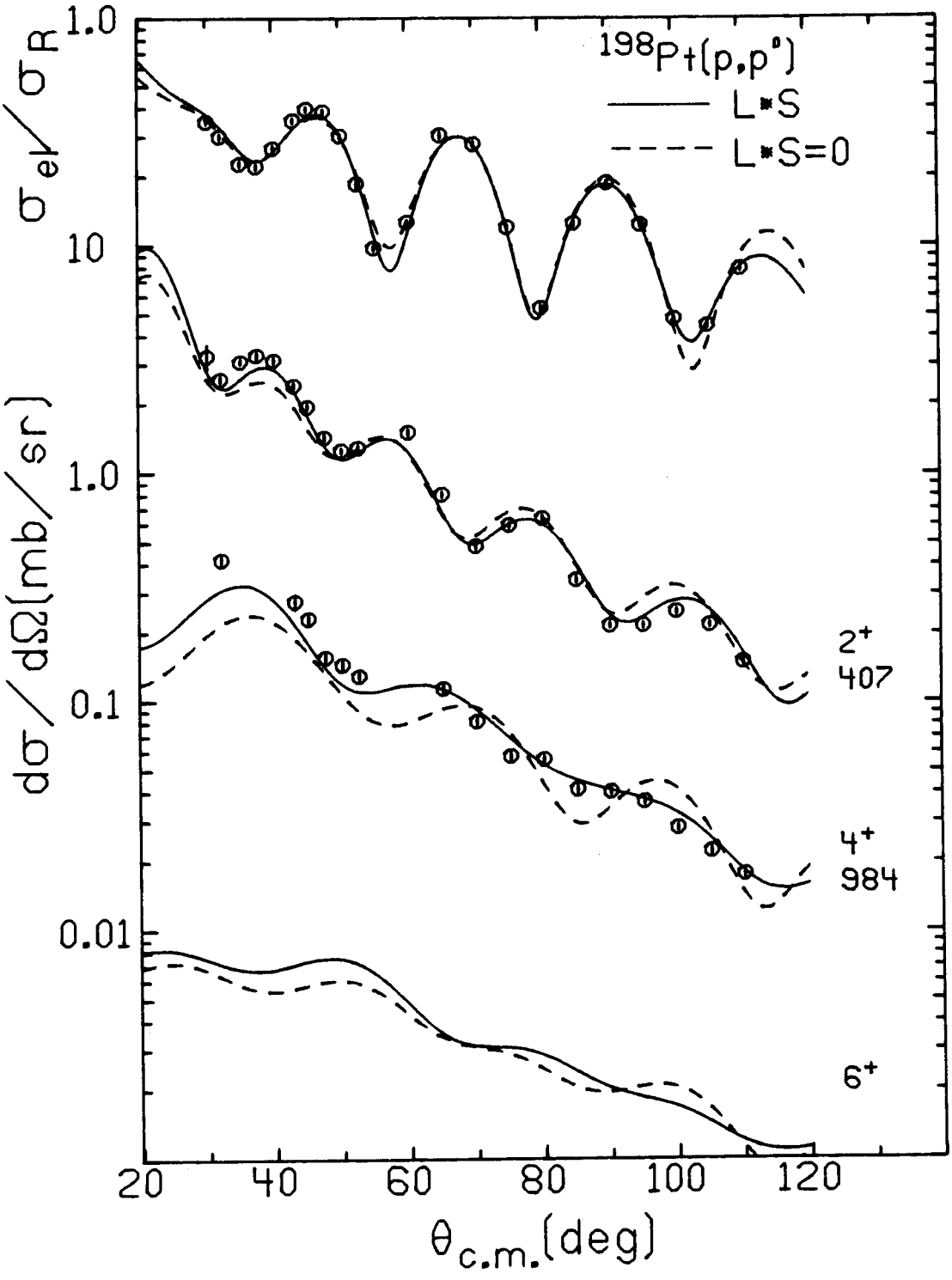
198Pt(p,p')
L*S
L*S=0
2+
407
4+
984
6+
dσ/dΩ(mb/sr)
σel/σR
θc.m.(deg)
1.0
10
1.0
0.1
0.01
20
40
60
80
100
120

Figure VI-8.

Table VI-9. Deformation Parameters and Potential Moments Obtained from 0-2-4-6 Coupled Channel Calculations for ^{194,196,198}Pt. Values from calculations with and without a spin-orbit (L*S) interaction are included.

Nucleus	β_2	β_4	q_2 (b)	q_4 (b^2)
^{194}Pt				
$\kappa = 0.0375$[a]				
L*S	-0.154(2)	-0.0455(10	-1.32(2)	-0.156(7)
L*S = 0	-0.168(3)	-0.0566(17)	-1.40(2)	-0.184(12)
$\kappa = 0.5375$				
L*S	-0.151(2)	-0.0453(10)	-1.30(2)	-0.160(6)
L*S = 0	-0.164(3)	-0.0550(20)	-1.37(3)	-0.181(12)
^{196}Pt				
$\kappa = 0.025$				
L*S	-0.142(3)	-0.0485(13)	-1.25(3)	-0.202(11)
L*S = 0	-0.152(5)	-0.0573(21)	-1.31(5)	-0.226(16)
^{198}Pt				
$\kappa = 0.016$				
L*S	-0.119(2)	-0.0422(20)	-1.05(2)	-0.177(7)
L*S = 0	-0.128(4)	-0.0479(30)	-1.09(4)	-0.181(18)

[a]The units for κ are keV.

ground state angular distribution and near 50^{o} in the 2^{+} angular distribution. The ratio-to-Rutherford calculation seems to be out of phase a few degrees between 70^{o} and 90^{o}, while the 2^{+} shape exhibits a pronounced minimum at 50^{o} unlike the shape calculated in ^{194,198}Pt(p,p'). These discrepancies may be the result of the problems with the optical model parameters for ^{196}Pt mentioned above.

Additional calculations were performed for each nucleus to investigate the effects of the spin-orbit interaction. Searches were performed on the optical model parameters with a spin of zero for the proton and with zero spin-orbit well depths. The major change in the parameters was in W_D, which increased significantly to decrease the depths of the minima (increase absorption) from the deep ones which result if the average parameters are used with spin-orbit effects turned off. Table VI-2 lists the results of these parameter searches for each nucleus. One can see the comparison of the spin-orbit versus non-spin-orbit (L*S) = 0) calculation in Figures VI-6, 7, and 8. The most obvious difference in each figure is the more pronounced oscillations in the L*S = 0 calculations. Each calculated shape displays this characteristic, with the 4^{+} shapes the most obvious. The poorer quality of these fits is borne out by chi-squared values which are nearly twice as large for each level as values from the calculations with spin-orbit. However, even though the L*S = 0 β_λ's values are significantly different

from the spin-orbit ones, the moments calculated in each case are comparable.

Although these calculations have shown the importance of spin-orbit effects in reproducing the data, there are still some practical advantages to investigating calculations without spin-orbit as long as one realizes their limitations. The major advantage of L*S = 0 calculations is the immense savings in computer time. As pointed out in Chapter III, the inclusion of a non-zero spin projectile in the CC calculations can more than double the number of coupled equations that must be solved. For proton scattering this translates into calculations that will require ten times as much computer time as the same calculation with a spin-zero projectile. With fewer coupled equations in an L*S = 0 calculation, the effective size of the computer is also increased. For example, on the Xerox Σ-7 computer at this laboratory, a 0-2-4-6-8-10 calculation is possible, while with spin-orbit included only a 2-2-4-6 calculation space can be used. The following section has capitalized on the advantages of calculations without spin-orbit to investigate the effect of a variety of couplings (some not possible with the inclusion of spin-orbit terms) and matrix elements on the quality of the fits and ultimately the extraction of the deformation parameters.

4. Sensitivity of CC Calculations to Higher Order Couplings and Selected Matrix Elements

a. The Sign of β_4

Earlier theoretical calculations [Ge 72] and experiments [Ba 76]have indicated the need for a negative value of β_4 to account for certain features of the Pt nuclides. A series of calculations were performed to investigate the sensitivity of the (p,p') data to the sign of β_4. Figure VI-9 compares the result of a 0-2-4-6 calculation for ^{194}Pt (without spin-orbit) with a positive, negative, and zero value for β_4. The χ^2 values for the 2^+ and 4^+ angular distributions are also given. Although the fit to the 4^+ level with a negative β_4 value is quite poor (mostly due to exclusion of spin-orbit effects), the overall slope and the fit to the first maximum are in agreement with the data. However, in the case of a positive β_4 (dashed line fit in Figure VI-9) the oscillations are almost completely out of phase with the example for $\beta_4 < 0$, and the cross section is overestimated at backward angles. Also, the value of $\chi^2_{2^+}$ increases by a factor of 2. The calculation with $\beta_4 = 0$ clearly fails to reproduce the data. The necessity of including a β_4 component is discussed further in a later section concerning the second 4^+ level. The present results seem to support earlier findings of a negative value of β_4 in the shape of the Pt isotopes.

Figure VI-9. Data and Coupled Channels Calculations in a 0–2–4–6 Space for ^{194}Pt(p,p') With Positive, Negative, and Zero Values for β_4. These calculations used the IBA matrix elements of Table VI–5 and the DOMP parameters of Table VI–2. No spin-orbit interaction was included. $\beta_2 = -0.172$.

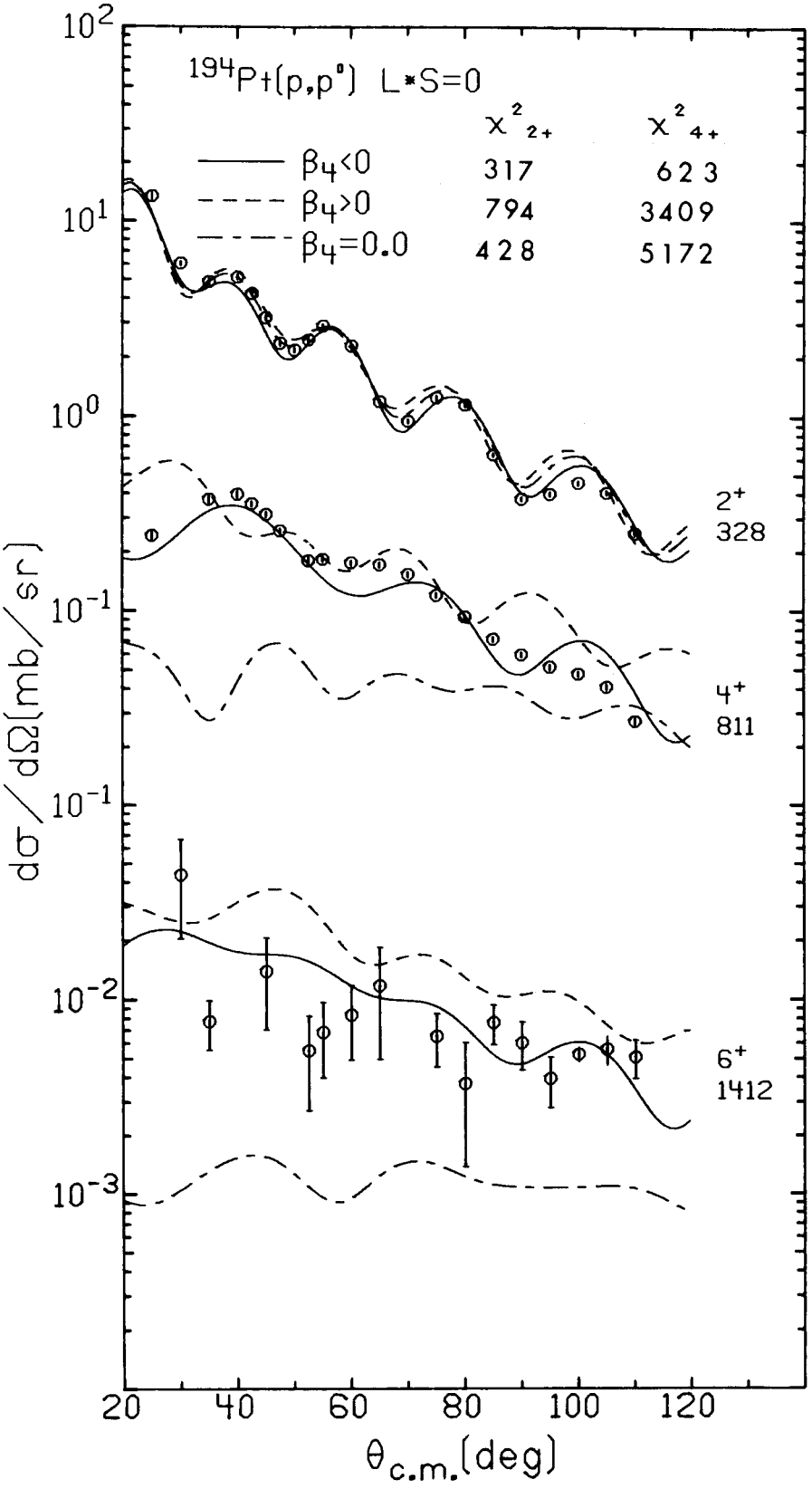
194Pt(p,p') L*S=0
χ²2+ χ²4+
β4<0 317 623
β4>0 794 3409
β4=0.0 428 5172
2+ 328
4+ 811
6+ 1412
dσ/dΩ(mb/sr)
θc.m.(deg)

Figure VI-9.

b. Investigation of a β_6 Deformation

Several calculations have been performed to examine the need for a β_6 component in the nuclear shape of the Pt nuclides. Figure VI-10 shows three situations for ^{194}Pt(p,p') with $\beta_6 = -0.01$, $\beta_6 = 0.0$, and $\beta_6 = +0.01$. These calculations were carried out in a $0^+-2^+-4^+-6^+-8^+$ level space using the couplings shown in Figure VI-5c, with no spin-orbit potential, and all angular momentum couplings up to L = 10. Although there does seem to be evidence in the rare-earth nuclei for a small β_6 shape component [He 68], the data for the 6^+ angular distribution for ^{194}Pt do not indicate any preference for a nonzero value. Even with improved data for the 6^+ state, it is doubtful whether any more information could be gained due to the similarities of each calculated 6^+ shape. As Figure VI-10 shows, the inclusion of a β_6 term also has very little effect on the shapes of the 2^+ and 4^+ angular distributions. A calculation was also performed allowing β_2, β_4, and β_6 to vary simultaneously to study the effects of β_6 on determining β_2 and β_4 values. Figure VI-11 compares this calculation with the final calculation of a β_2, β_4 search for ^{194}Pt with the same initial β_λ's and no spin-orbit potential. Although the deformation parameters have changed significantly, and the fit to the 4^+ is improved (at the expense of the 2^+ fit), this is the result of a final value for β_6 of +0.067, which seems physically unlikely (see e.g. [He 68]).

Figure VI-10. Comparison of Data and Coupled Channels Calculations for ^{194}Pt(p,p') With the Couplings of Figure VI-5C, and Three Values for β_6. The calculations included the matrix elements of Table VI-5, and the DOMP parameters of Table VI-2 with no spin-orbit interaction. $\beta_2 = -0.172$, $\beta_4 = -0.0567$.

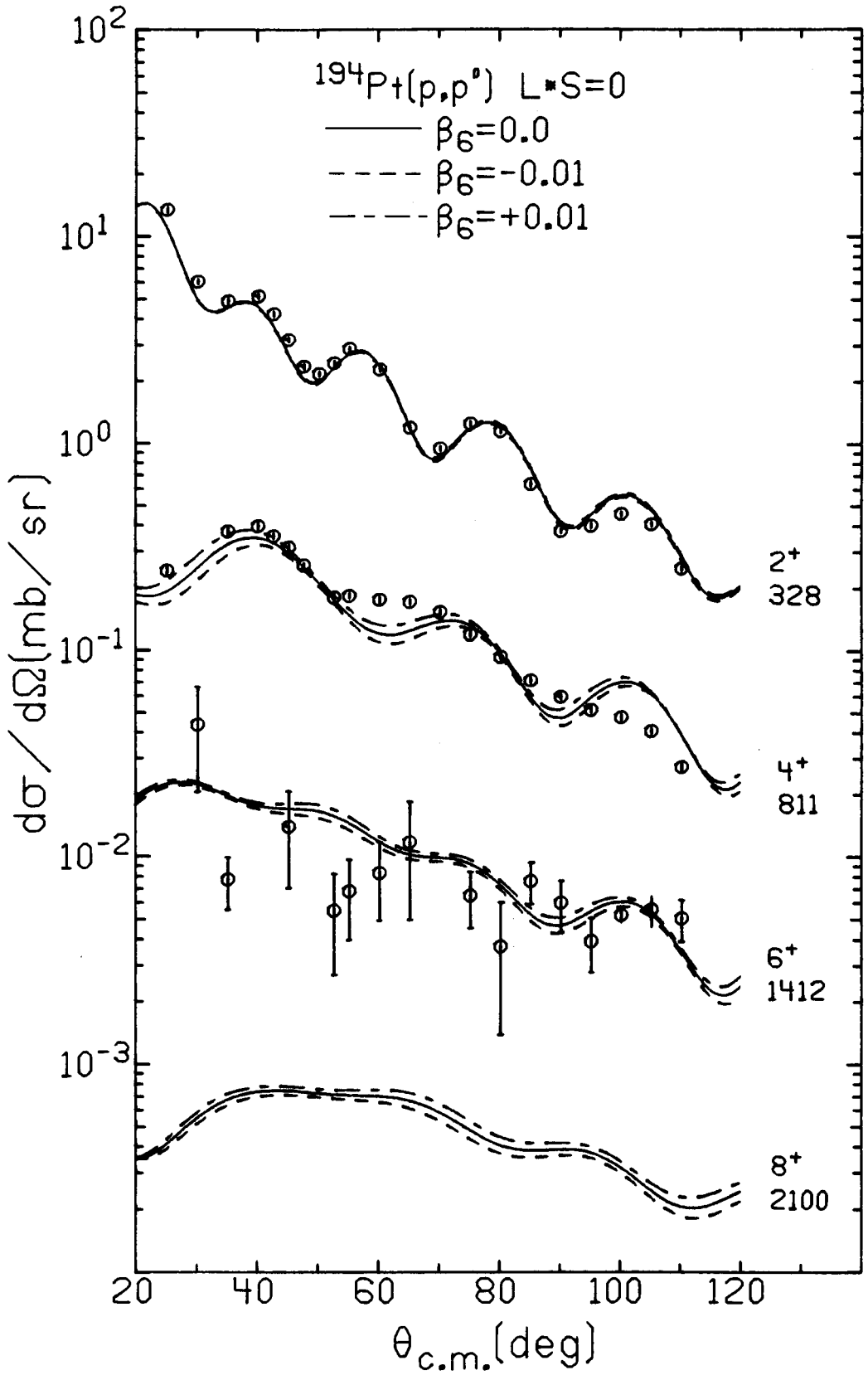
^{194}Pt(p,p') L*S=0
β_6=0.0
β_6=-0.01
β_6=+0.01
2+
328
4+
811
6+
1412
8+
2100
dσ / dΩ(mb/sr)
θc.m.(deg)
10^2
10^1
10^0
10^-1
10^-2
10^-3
20
40
60
80
100
120

Figure VI-10.

Figure VI-11. Data and Coupled Channels Calculations for $^{194}Pt(p,p')$ With Search on β_2, β_4, and With $\beta_6 = 0$ (Dashed Curve) and for Search on β_2, β_4, and β_6 (Solid Curve). No spin-orbit interaction was included. Both calculations had the same initial values for $\beta_2 (= -0.172)$ and β_4 (−0.0567). The matrix elements were taken from Table VI−5 and DOMP parameters from Table VI−2.

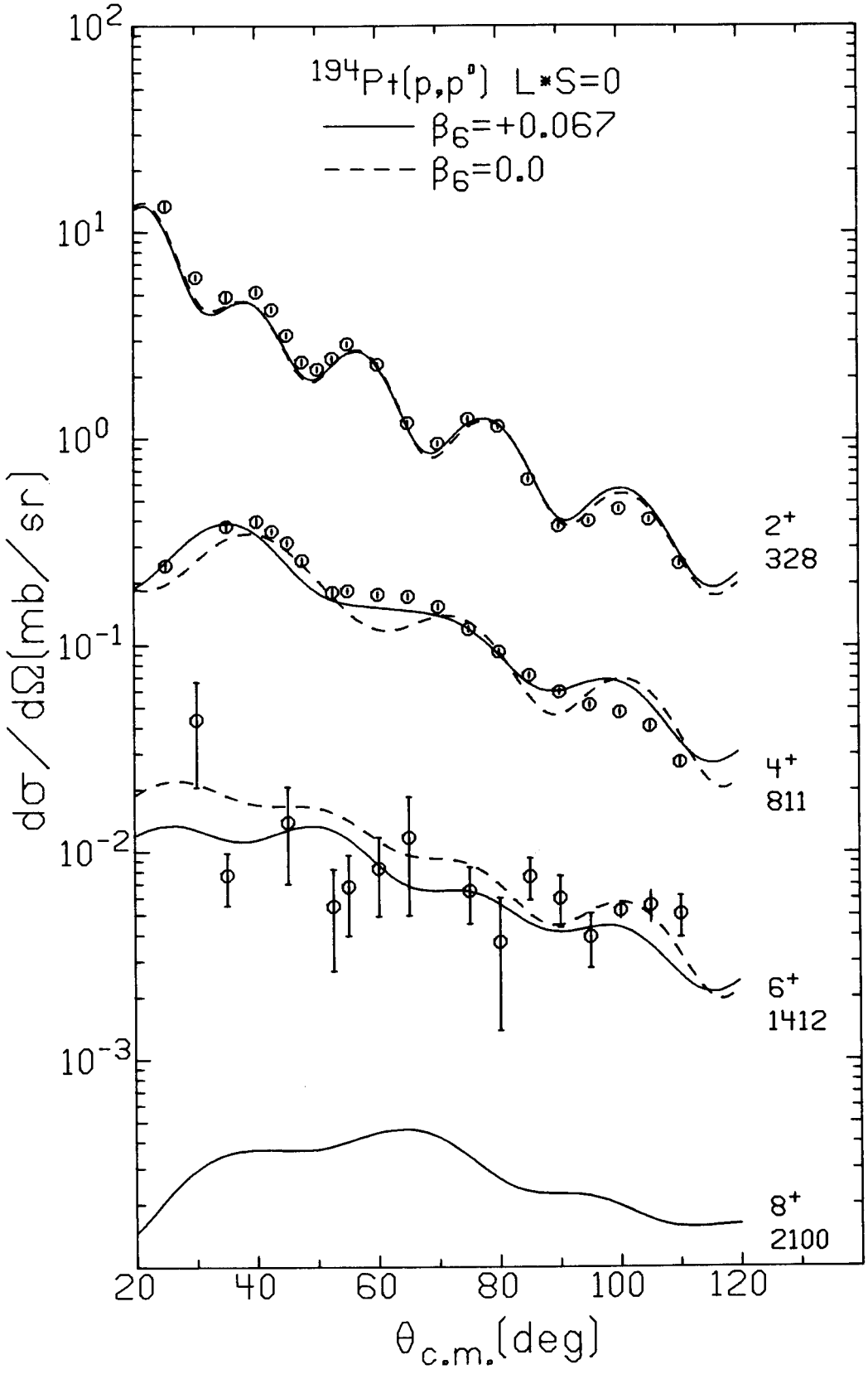
$^{194}Pt(p,p')$ L*S=0
β_6=+0.067
β_6=0.0
10^2
10^1
10^0
10^{-1}
10^{-2}
10^{-3}
$d\sigma / d\Omega$(mb/sr)
2+
328
4+
811
6+
1412
8+
2100
20
40
60
80
100
120
$\theta_{c.m.}$(deg)

Figure VI-11.

c. The Effect of γ-band Couplings

In order to test further the O(6) IBA matrix elements, calculations were initiated to include the lowest states of the γ-band, whose bandhead is the second 2^+ state. Three previous inelastic scattering studies of the Pt nuclei have included results for the γ-band. Only the 2^+ state of the γ-band in ^{194}Pt was studied in References [Ba 76, Ba 79]. The former investigation used a combination of empirical and rotational matrix elements, while the later analysis was performed within a triaxial rotor framework. Reference [Ba 78] included both the 2^+ and 4^+ members of the γ-band for ^{192}Pt and also used empirical and rotational matrix elements. The later two studies also seemed to indicate that the inclusion of β_4 deformations was important in obtaining a more thorough understanding of these nuclei.

In the present study, data were obtained for the 2^+, 3^+, and 4^+ states of the γ-band in ^{194,196}Pt and for the $2^{+'}$ and $4^{+'}$ states in ^{198}Pt. The calculations included both β_2 and β_4 deformations, and initially, a full set of IBA matrix elements. As discussed later in this Chapter, the IBA $0 \rightarrow 4^{+'}$ matrix element was extremely small and a larger value was necessary to reproduce the data.

The results of these calculations for ^{194}Pt are shown in Figure VI-12 for two different sets of matrix elements. Both calculations included the couplings of Figure VI-5e with the L*S interaction and the appropriate deformation parameters

Figure VI-12. Data and 0-2-4-2'-3-4' Calculations for ^{194}Pt(p,p') With the Spin-Orbit Interaction and Two Sets of IBA Matrix Elements, Table VI-6 (Solid Curve), and Table VI-5 (Dashed Curve). The couplings included those of Figure VI-5e. The appropriate DOMP parameters were taken from Tables VI-2 and 9.

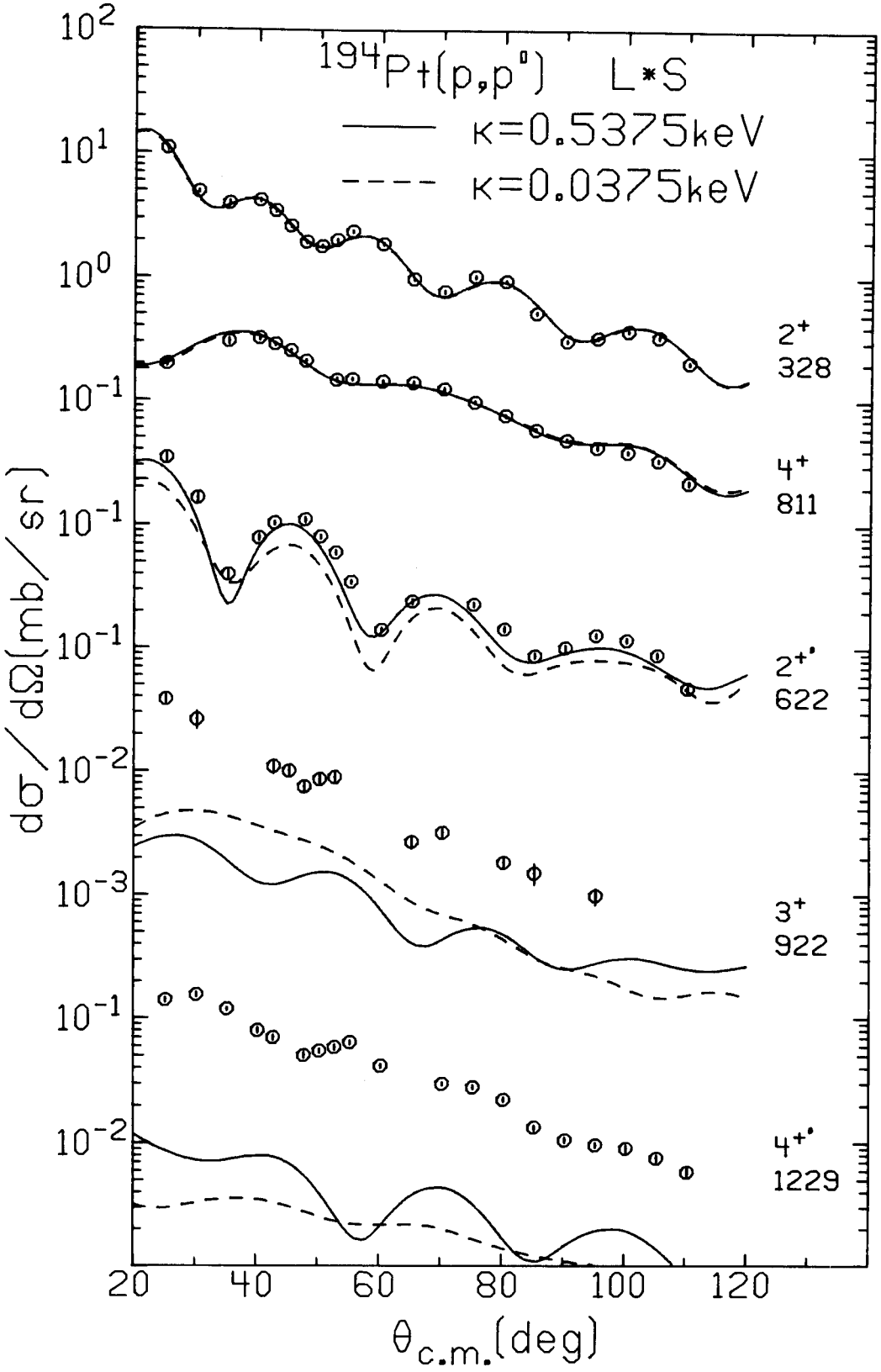
^{194}Pt(p,p$'$) L*S
κ=0.5375keV
κ=0.0375keV
2+
328
4+
811
2+•
622
3+
922
4+•
1229
dσ/dΩ(mb/sr)
θc.m.(deg)
10^2
10^1
10^0
10^-1
10^-2
10^-3
20
40
60
80
100
120

Figure VI-12.

from Table VI-9. One set (κ = 0.0375 keV) is the set mentioned earlier, which was derived from the parameters of [Ca 78]. The second set was obtained from PHINT by increasing the strength of the quadrupole force between the bosons (κ = 0.5375 keV) while the remaining O(6) parameters retained their previous values (see Table VI-4). The two calculations provide nearly identical fits to the ground band states (comparable fits to those shown in Figure VI-6 with no γ-band couplings). The γ-band fits, however, show distinct differences. The calculation with κ = 0.5375 (solid line) yields a definite improvement in the fit of the $2^{+'}$ state, both in strength and the depth of the minima. However, even though both calculations underestimate the strengths of the $3^{+'}$ and $4^{+'}$ angular distributions, the solid line fit for κ = 0.5375 introduces far more structure into the shapes of both angular distributions. This may be due to the order of magnitude differences in the matrix elements between the levels of the γ-band, as well as between the $3^{+'}$, $4^{+'}$, and the first 2^{+} state. This changes the interference between the many coupling paths, and thus the shape of the angular distributions.

As stated above, the difference between the two sets of matrix elements is a larger value of κ, the strength of the quadrupole-quadrupole boson force. Small values for this parameter primarily affect the magnitude of transitions which were not allowed in the strict O(6) limit due to the $\Delta\tau = \pm 1$

selection rule. As Figure II-7 shows, the affected transitions are $M_{02'}$, $M_{23'}$, $M_{24'}$, $M_{34'}$, and $M_{2'4}$, where

$$M_{jk} = -\langle k||M(E2)||j\rangle .$$

Also affected are the reorientation matrix elements because of the increased mixing of the wave functions. Thus, both sets of matrix elements result in nearly identical fits for the ground band, since the intraband transitions are virtually unchanged.

The value of κ for the matrix elements of Table VI-6, which gives the solid line fit in Figure VI-12, was determined by varying κ in the IBA code PHINT until the ratio of $B(E2; 2^{+'} \rightarrow 0^{+}/B(E2; 2^{+'} \rightarrow 2^{+})$ approached the experimental value of 0.0031 [Ca 78]. This increase in $M_{02'}$ provides the necessary strength to fit the $2^{+'}$ state, however, at the expense of the already poorly fit 3^{+} and $4^{+'}$ states. The new value of κ is not an unrealistic value even though it is about 20 times as large as the value taken from [Ca 78]. The larger value is still an order of magnitude smaller than the values used in the Os nuclei calculations of Reference [Ca 78], which show considerably more rotational character, the feature which κ actually represents. A search on $M_{02'}$ was performed using the couplings of Figure VI-d and the κ = 0.0375 keV matrix elements. The "best fit" value for $M_{02'}$ was determined to be 0.046, compared to 0.063 from the PHINT calculations when κ = 0.5375 keV.

The implication for such small values of $M_{02'}$ is that the population of the $2^{+'}$ state is achieved primarily through a two-step process, $0 \rightarrow 2 \rightarrow 2^{+'}$, where the two matrix elements involved are each two orders of magnitude larger than $M_{02'}$.

Another IBA matrix element that is very small compared to the experimental value is M_{22}, the reorientation matrix element. The present calculations are not very sensitive to this matrix element, because the reorientation effect is proportional to Z^2 of the projectile and produces the largest effect at backward angles. Thus, the proton scattering data are a relatively weak probe of this effect. For calculations involving the scattering of low energy alpha particles, where this effect is important, significantly larger values would be needed for κ than the values from Casten and Cizewski [Ca 78].

d. The Effect of the $2^{+'}$ State on the β_λ's

To test the influence the $2^{+'}$ state may have on extracting the deformation parameters, a simultaneous search was made on β_2 and β_4 using a $0^+-2^+-4^+-2^{+'}$ coupling scheme and the IBA matrix elements with κ = 0.5375 keV while minimizing the chi-squared values for each level. Table VI-10 compares the results of the above L*S = 0 calculation with those for a similar β_λ search also minimizing all four χ^2 values in a $0^+-2^+-4^+-6^+$ level space. Both calculations had the same initial values for β_2 and β_4

Table VI-10. Comparison of Initial and Final Values for β_λ and χ^2 Between a $0^+-2^+-4^+-6^+$ and $0^+-2^+-4^+-2^{+\prime}$ Calculation, Both With L*S = 0 and κ = 0.5375 keV.

	$0^+-2^+-4^+-6^+$ Calculation		$0^+-2^+-4^+-2^{+\prime}$ Calculation	
	Initial Values	Final Values	Initial Values	Final Values
β_2	-0.1773	-0.1683	-0.1773	-0.1648
β_4	-0.0575	-0.0550	-0.0575	-0.0554
χ^2_{0+}	317	315	328	351
χ^2_{2+}	414	283	746	346
χ^2_{4+}	927	669	876	658
χ^2_T	1658	1267	1950	1355

and in each calculation, χ_T^2 ($= \chi_0^2 + \chi_2^2 + \chi_4^2$) minimized on the same final values within statistical uncertainties. However, the better fit was obtained in the $0^+-2^+-4^+-6^+$ calculation as indicated by the total chi-squared, 1267, compared to 1355 for the $0^+-2^+-4^+-2^+$ calculation. The relatively weak coupling of the $2^{+'}$ state, and thus the entire γ-band, indicates that calculations involving only ground band couplings are sufficient for determining the deformation parameters.

e. The Sign of P_3

One of the principal motivations for the earlier inelastic scattering studies on the Pt nuclides [Ba 76, Ba 78, Ba 79] was to determine the sign of the E2 interference term $P_3 = M_{02'}M_{02}M_{22'}$, where

$$M_{jk} = -\langle k||M(E2)||j\rangle .$$

The CC calculations are sensitive to the relative signs of these matrix elements, because of the interference between the one-step and two-step paths that can be used to populate the second 2^+ state, $0 \rightarrow 2'$ and $0 \rightarrow 2 \rightarrow 2'$, respectively. The studies of Baker et al. indicate that a negative value of P_3 is needed to fit the data. This was an unexpected finding since both the asymmetric rotor [Ba 58] and pairing-plus-quadrupole [Ku 69] models predict $P_3 > 0$. These same experimental studies also conclude that large values of M_{04} and $M_{04'}$ are needed to explain the shape and strength of the

4^+ angular distributions. However, in [Ba 79] it was shown that by including only the symmetric, E4 components to the usual E2 asymmetric rotor shape (Davydov model [Da 58]) the fit to the first 4^+ level was improved and that a negative value of P_3 was now consistent with the predictions of this "extended" asymmetric rotor model.

In the present study calculations have been performed, with the L*S interaction, to investigate the sensitivity of the (p,p') data to the sign of this interference term. Since the proton scattering also indicates the need for large, direct E4 matrix elements, the first 4^+ state and a β_4 deformation were included in the calculations. The couplings used are shown in Figure VI-5d and the β_λ's were those from Table VI-9. The major differences in these calculations and those from Reference [Ba 79] are the use of O(6) IBA matrix elements and a symmetric parameterization of the shape of the nucleus having a diffuse cutoff. Figure VI-13 shows the results of a 0-2-4-2' calculation for ^{194}Pt performed with the matrix elements of Table VI-6. The sign of P_3 was changed by changing the sign of $M_{02'}$. The data are fit much better when $P_3 < 0$, in agreement with earlier studies [Ba 76, Ba 79]. This is also true in similar calculations for ^{196}Pt. Interestingly, the O(6) IBA calculations correctly predict the sign of P_3 in both sets of matrix elements calculated for ^{194}Pt and for ^{196}Pt. So, the present analysis and that of Baker et al. [Ba 79] both agree that $P_3 < 0$ and yield

Figure VI-13. Data and Coupled Channels Calculations for $^{194}Pt(p,p')$ With Positive (Dashed Curve) and Negative (Solid Curve) Values for the Interference Term, P_3. Note that the data and theory for the 2^+ state have been multiplied by 2. The couplings of Figure VI-5d were used with $\beta_2 = -0.151$ and $\beta_4 = -0.0453$.

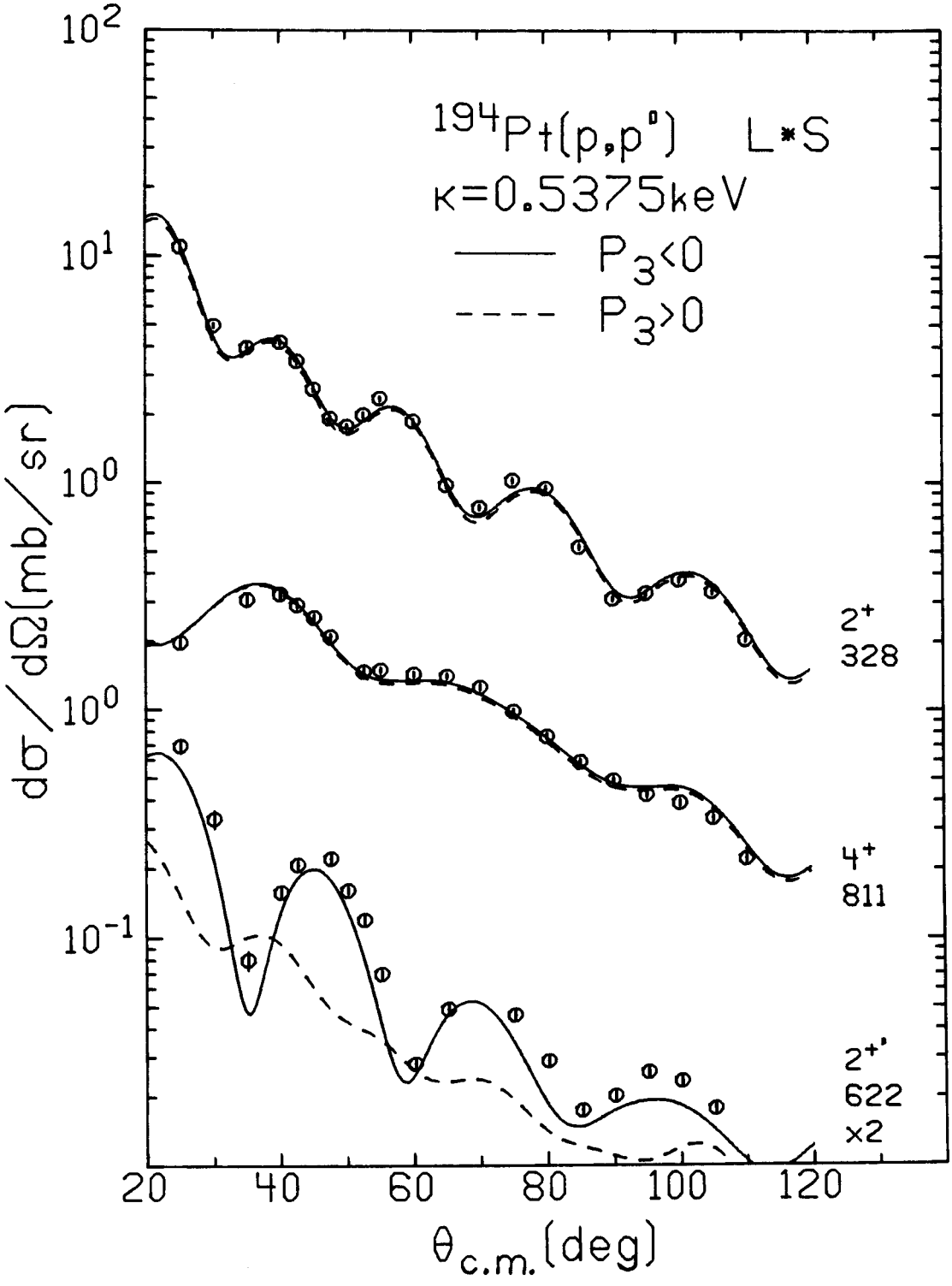
^{194}Pt(p,p') L*S
κ=0.5375keV
P3<0
P3>0
2+
328
4+
811
2+'
622
x2
dσ/dΩ(mb/sr)
θc.m.(deg)
10^2
10^1
10^0
10^0
10^-1
20
40
60
80
100
120

Figure VI-13.

essentially the same q_2 and q_4 charge moments (see Section B.4.g of this Chapter), but with each method assuming a different shape for the nucleus. Thus, the scattering data analysis, much like the case of odd-A nuclei coupled to a variety of even-even cores, does not give unambiguous results as to the shape of these transitional nuclei. The scattering data predict no apparent distinction between a rigid, asymmetrically deformed nucleus, and a γ-unstable (O(6)) nucleus, "frozen" in a symmetric oblate shape.

For ^{198}Pt(p,p') the calculations with $P_3 > 0$ provide slightly better fits to the data, even though the O(6) calculations predict $P_3 < 0$. However, in these calculations, $M_{02'}$ is a small negative number, -0.0012. This change of sign compared to the ^{194,196}Pt O(6) calculations is understandable because in the strict O(6) limit $M_{02'} = 0$ due to the $\Delta\tau$ selection rule. With the addition of a small perturbation (κ), the selection rule is broken and small values of about zero are obtained. The reason P_3 remains negative is because the sign of M_{02} unexpectedly changes as well. The cause of this sign change is not understood. To draw any conclusions about the role of P_3 in the analysis of the data for ^{198}Pt it seems best to secure first a better value for κ because of its influence on the small matrix elements.

f. The $M_{04'}$ E4 Matrix Element

The CC calculations obviously fail to reproduce the data for the $4^{+'}$ angular distribution in ^{194}Pt(p,p') with O(6)

matrix elements (see Figure VI-12). This was true in similar calculations for ^{196,198}Pt(p,p') (see Figure VI-15, dashed curves). The major cause of this failure is the small, predicted E4 matrix elements between the ground state and second 4^+ level, resulting in a calculated cross section which is more than an order of magnitude weaker than the data. A similar effect was seen in the (α,α') study of Reference [Ba 78]. To improve such calculations a search was performed on the $0-4^{+'}$ matrix element to fit the $4^{+'}$ angular distribution. The remaining matrix elements were the IBA values of Tables VI-5, 6, 7, and 8, scaled with the appropriate L*S = 0 β_λ's from Table VI-9. The search was performed without the spin-orbit term so that a 0-2-4-2'-3-4' level space could be used with the couplings of Figure VI-5e (except for ^{198}Pt where no 3^+ couplings were included). Computer limitations precluded a search in this level space with a spin-orbit interaction. However, as shown in Figure VI-14a, the shape of the $4^{+'}$ angular distribution with and without spin-orbit are similar enough that the values of $M_{04'}$ from these L*S = 0 searches were also used in the calculations with spin-orbit included. The results of these calculations are shown as the solid curves in Figures VI-14 and 15 for ^{194,196,198}Pt. For comparison the calculations with the full IBA matrix elements are also shown. The best fit is obtained in the ^{198}Pt case, with the rather structureless shape except for a maximum at 35^o. The other three

Figure VI-14. Data and Coupled Channels Calculations for $^{194}Pt(p,p')$ With $\kappa = 0.0375$ and 0.5375 keV. The dashed curve represents calculations with the full set of IBA matrix elements, while the solid curve represents calculations with the best fit value for M_{04}, included. The calculations used the couplings of Figure VI-5e and the DOMP parameters of Tables VI-2 and 9.

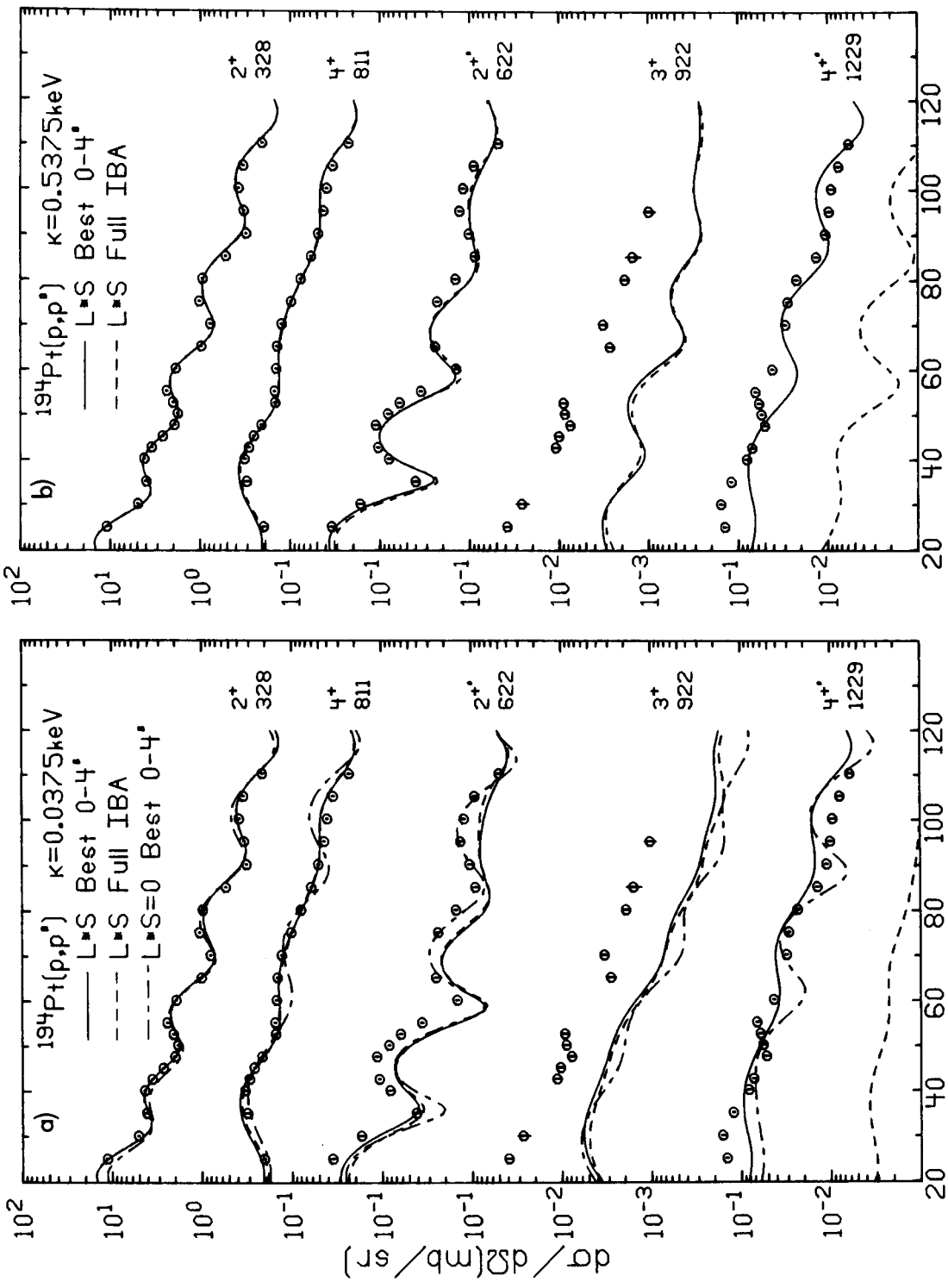
a) ^{194}Pt(p,p') κ=0.0375keV
L*S Best 0-4+
L*S Full IBA
L*S=0 Best 0-4+
b) ^{194}Pt(p,p') κ=0.5375keV
L*S Best 0-4+
L*S Full IBA
2+ 328
4+ 811
2+' 622
3+ 922
4+' 1229
dσ/dΩ(mb/sr)
θc.m.(deg)

Figure VI-14.

Figure VI-15. Data and L*S Coupled Channels Calculations for ^{196,198}Pt(p,p'). The dashed curve represents a calculation with the full set of IBA matrix elements, while the solid curve represents a calculation with the best fit value for M_{04}, included. The calculations used the couplings of Figure VI-5e (except ^{198}Pt(p,p') did not include 3^+ couplings) and the DOMP parameters of Table VI-2 and 9.

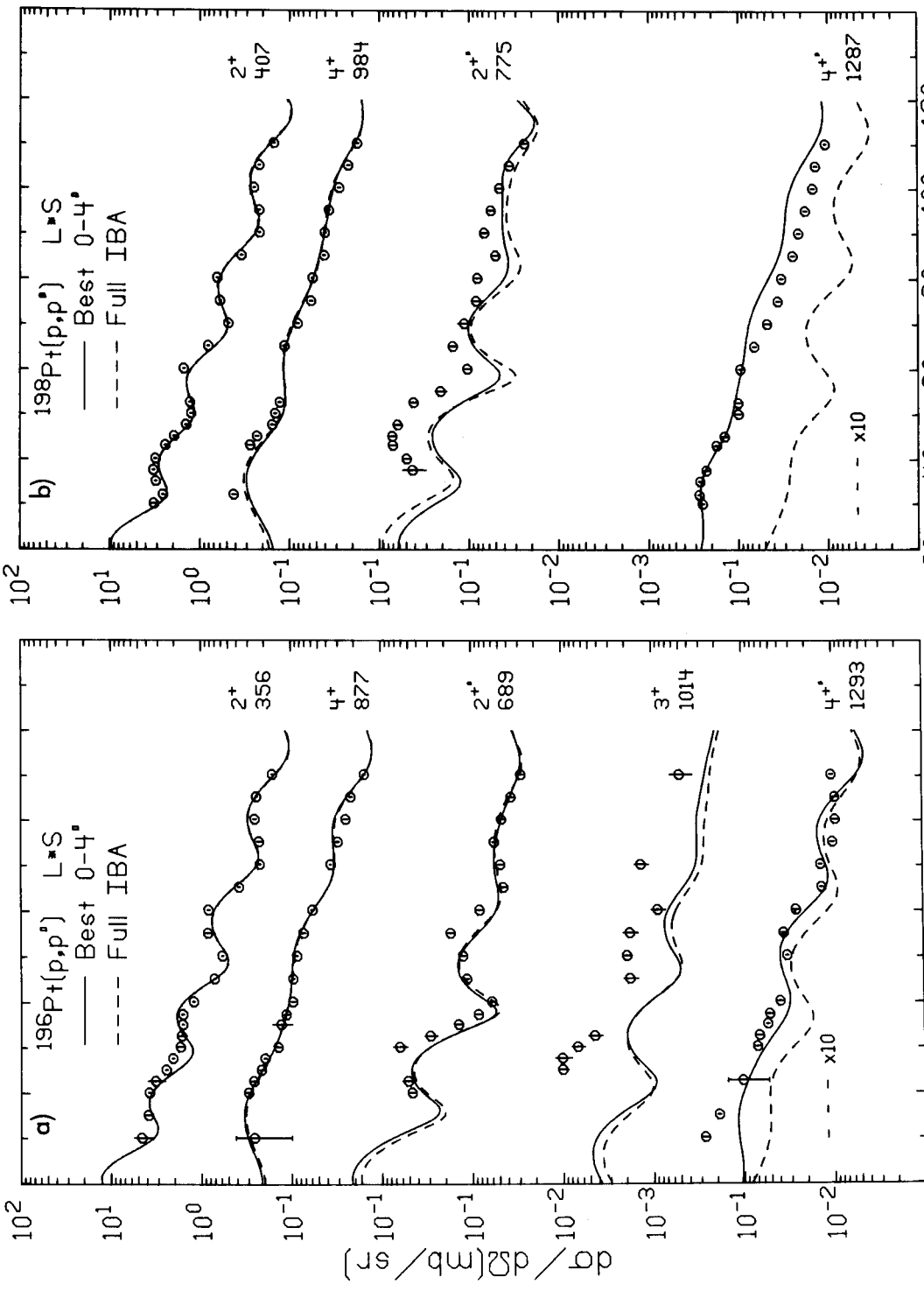
a) ^{196}Pt(p,p') L=S
Best 0-4'
Full IBA
2+ 356
4+ 877
2+' 689
3+ 1014
4+' 1293
x10
b) ^{198}Pt(p,p') L=S
Best 0-4'
Full IBA
2+ 407
4+ 984
2+' 775
4+' 1287
x10
dσ/dΩ(mb/sr)
θc.m.(deg)

Figure VI-15.

calculations show a considerably more diffractive shape for this angular distribution. Table VI-11 summarizes the $M_{04'}$ and B(E4) values as well as these values from $^{192}Pt(\alpha,\alpha')$ [Ba 78]. Baker et al. obtained a better fit with the positive value for $M_{04'}$, however, the (p,p') results give B(E4) values that are more comparable to the magnitude for the negative value for $M_{04'}$.

It should be noted that the sign of these matrix elements is relative to the two-step and three-step excitation routes for the $4^{+'}$ level. The interferences between the routes may be causing the varying amplitudes of the oscillations. This uncertainty in sign can also lead to an uncertainty in magnitude as is shown in Table VI-11 for ^{192}Pt. The best fit values from this study are thus relevant only in regard to the signs and magnitudes of $M_{02'}$, $M_{22'}$, $M_{2'4'}$, $M_{4'}$, and $M_{02'}$.

g. Comparison of Charge and Nuclear Potential Moments

As discussed in Chapter III.C, this study has followed the suggestion of Mackintosh [Ma 76] and reports the results of the CC calculations in terms of q, a potential multipole moment. Mackintosh, using a theorem due to Satchler [Sa 78], has shown that the multipole moments of the potential, q, are proportional to moments of the nuclear matter density, if the deformed optical model potentials (DOMP) for protons are derivable from a reformulated optical model potential, where one assumes the nucleon-nucleon interaction is independent of

Table VI-11. Summary of $0 \rightarrow 4'$ Matrix Elements and B(E4) Values for $^{192-198}Pt$.

Nucleus	$M_{04'}$ (eb^2)	B(E4; 0-4') (e^2b^4)	B(E4; 0-4) (e^2b^4)
^{192}Pt[a]	+0.34	0.12	0.041
	-0.20	0.040	0.041
^{194}Pt			
$\kappa = 0.0375$	-0.12	0.014	0.024
$\kappa = 0.5375$	-0.11	0.012	0.026
^{196}Pt	+0.14	0.020	0.041
^{198}Pt	+0.21	0.043	0.031

[a]Values from [Ba 78].

density, and the proton and neutron distributions have the same deformation. This multipole moment method is used here because in addition to being a more fundamental approach, it also facilitates the comparison of results from Coulomb and nuclear scattering experiments.

The q_2 and q_4 calculated using Equation (III-71) and the DOMP parameters of Table VI-2 are listed in Table VI-12 and displayed schematically in Figure VI-16, along with moments from Coulomb excitation [Ba 79, Ba 78a, Gl 69], and those calculated from an (α,α') Coulomb-nuclear interference experiment [Ba 76], in which both charge and potential moments can be obtained. Also shown are the moments deduced from the theoretical predictions of β_2 and β_4 from Gotz et al. [Go 72] determined by a Strutinsky renormalization method. These moments were calculated using the parameters of the single particle potential for neutrons. The Coulomb deformation parameters obtained in [Ba 79] and [Ba 76] used a uniform charge distribution with a sharp cutoff for asymmetrically and symmetrically deformed shapes, respectively. The potential moments in the present study and in [Ba 76] used a deformed Fermi distribution.

A comparison of the (p,p') results with those from the previous experiments indicates the q_2 potential moments from proton scattering are in much better agreement with the charge moments from Coulomb excitation values than the potential moments of Baker et al. [Ba 76] determined by

Table VI-12. E2 and E4 Moments in $^{192,196,198}Pt$.

Nuclide	Method	q_2^a (b) or (eb)	q_4^a (b^2) or (eb^2)
^{194}Pt			
	(p,p') at 35 MeV[b]	-1.32(2)	-0.156(7)
	Coulomb excitation[c]	-1.273(6)	
	(^{12}C,$^{12}C'$)[d]	-1.269	-0.1486
	(α,α')[e] P	-1.52	-0.30
	C	-1.31	-0.12
	Theory[f]	-1.468	-0.129
^{196}Pt			
	(p,p') at 35 MeV[b]	-1.25(3)	-0.202(11)
	Coulomb excitation[g]	-1.22(5)	
	(α,α')[e] P	-1.38	-0.24
	C	-1.17	-0.097
	Theory[f]	-1.380	-0.142

Table VI-12 (cont'd.).

Nuclide	Method	q_2^a (b) or (eb)	q_4^a (b^2) or (eb^2)
^{198}Pt			
	(p,p') at 35 MeV[b]	-1.05(2)	-0.177(7)
	Coulomb excitation[g]	-1.00(3)	
	(α,α')[e] P	-1.12	-0.32
	C	-1.08	-0.14
	Theory[f]	-0.579	-0.106

[a] The units for the charge component moments are b^λ, λ = 2 or 4. The units for the electromagnetic moments are eb^λ.

[b] These moments were obtained using the DOMP parameters, including the spin-orbit interaction, contained in Tables VI-2, 9.

[c] Reference [Ba 78a].

[d] Reference [Ba 79].

[e] Reference [Ba 76]. The first value reported is for the potential moment (P) calculated from Baker et al. and the second value is for the charge moment (C).

[f] Reference [Go 72].

[g] Reference [Gl 69].

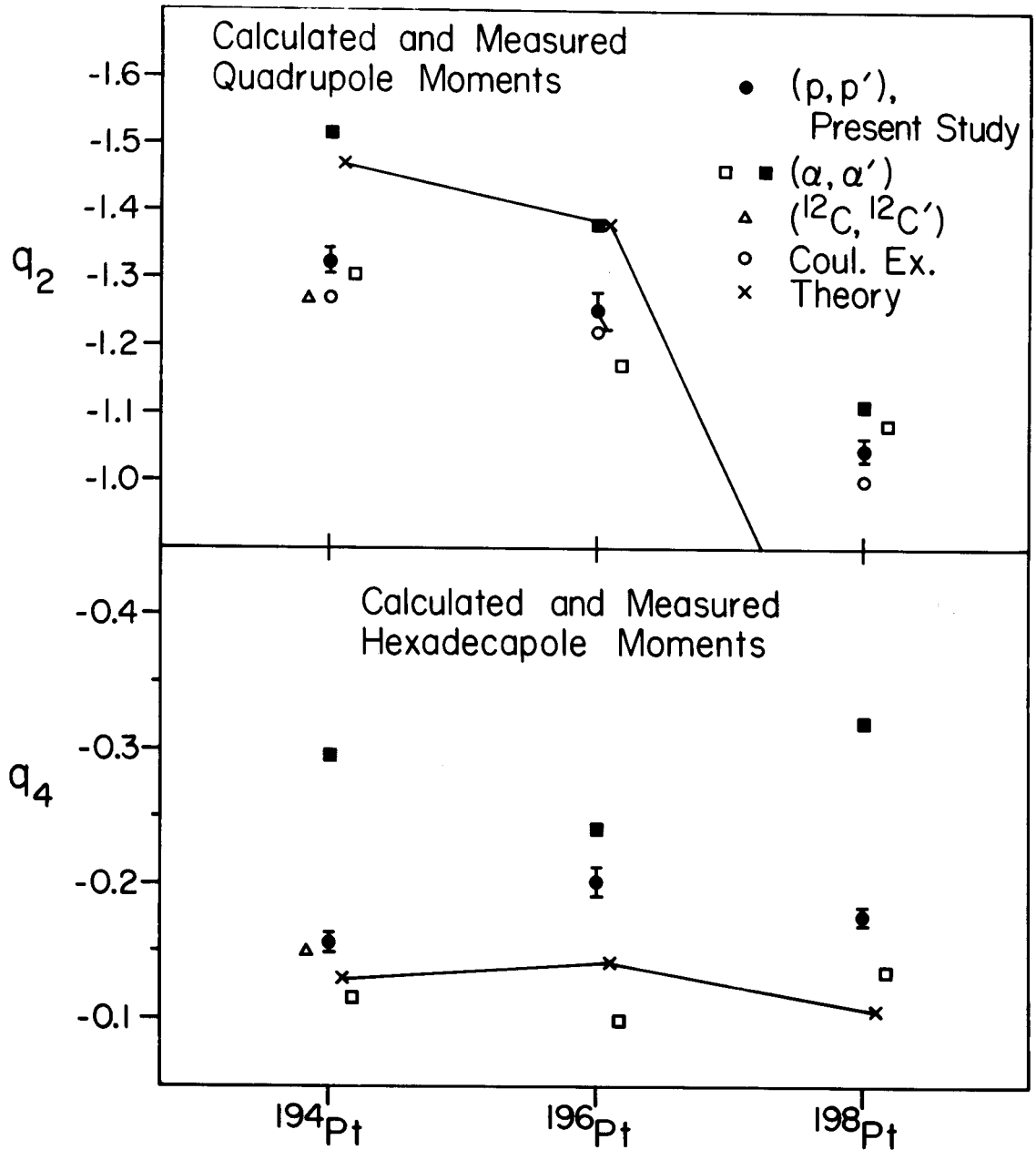

Figure VI-16. Plot of Quadrupole and Hexadecapole Moments for ^{194,196,198}Pt Given in Table VI-12.

(α,α'). This is also the trend of the q_4 moments. In each nucleus the charge component of the proton potential moment is in better agreement with the charge moment from [Ba 76, Ba 79] and also the theoretical values of Gotz et al. These same theoretical values for the q_2 moments, however, are nearer the values for the potential moments of [Ba 76], except in ^{198}Pt where the predicted q_2 value is only one-half the smallest experimental value.

This discrepancy between α scattering, potential moments, and Coulomb excitation values has been discussed by Mackintosh [Ma 76] and is thought to be an indication that the α scattering potentials cannot be derived from reformulated optical model potentials. If this is true it may mean that high energy α-scattering is not a reliable probe for measuring nuclear shapes. It has long been thought that α-particles should be an excellent surface probe because of their strong absorption by the nucleus and the simplifications resulting from being a spin zero projectile. However, in most analyses the structure of the α-particle itself has been ignored. There is less of a problem of this type with a proton as the projectile.

A fundamental question can now be asked about the data in Table VI-12. Do the differences between the potential (matter) moments from Coulomb scattering imply that neutron and proton distributions are not the same? Calculations by Hamilton and Mackintosh [Ha 77] indicate that differences of

20 to 30% could exist between neutron and proton moments in ^{154}Sm. Even though each potential moment calculated in this study is larger than the charge moment for all three nuclei, the differences are statistically significant only for the q_2 moment of ^{194}Pt and the q_4 value in ^{196}Pt. This fact, in addition to questions concerning the strict validity of this multipole moment procedure, prohibit one from seriously considering such small differences. Even though this approach to analyzing scattering data is believed to be the most fundamental phenomenological method available, there are several facets which must be investigated, such as: how should the imaginary part of the DOMP be included in the moments; are the DOMP's derivable from a reformulated optical model potential; are density dependent effects important in the interaction potentia; how does one scale β_λ and r_o? Once these are understood, it may be possible to interpret extracted moments with more confidence.

CHAPTER VII

CONCLUDING REMARKS

The recent interest in the study of the shape transitional Pt nuclei is because of the key role they possibly play in understanding collective nuclear behavior. These nuclei span a region between the relatively well understood limits of the standard hydrodynamic collective model, and thus provide an experimental test for new models in this region or for variations on the simple collective model. When the present study began most of the data on these nuclei were from (n,γ) experiments or decay studies, except for two transfer studies [Mu 65, Ma 72]. Thus, the present high-resolution reaction study has contributed much new data on the Pt nuclides to aid in distinguishing between the variety of models applied in this region.

Recently Casten and Cizewski [Ca 78, Ci 78] have shown that the O(6) limit of the IBA model does a remarkable job in explaining the branching ratios and energies of all positive parity levels below 2 MeV. As shown in this thesis, some of the features of this model can also be used to interpret several aspects of the (p,t) and (p,p') data with reasonable success. In the (p,t) reaction studies, the strengths of the

L = 0 and L = 2 transitions have been compared to the predictions of the IBA model. This model provides a natural framework for discussing multi-particle transfer reactions because of its inherent feature of pairing fermions to form bosons. The general agreement of these calculations with the data is quite good, particularly in the trend of ground state strengths and in the preferential population of the second excited 0^+ level over the first. For the L = 2 transitions the model correctly predicts the relative magnitudes for the cross section for the first and second 2^+ levels within a particular nucleus, although the calculated trends versus changes in A are not seen in the data. These problems are possibly related to the choice of the coefficients in the L = 2 operator. The values used in these calculations ($\alpha = 1$, $\beta = 0.08$, and $\gamma = 0$) were chosen without any previous knowledge of the (p,t) data. A more judicious choice of these parameters may give results in better agreement with the data. Also, by including some of the smaller terms of the L = 0 and L = 2 operators, some of the very small cross sections predicted for the third and fourth 0^+ and 2^+ states may be altered.

The O(6) limit of the IBA has also been utilized in interpreting the inelastic proton scattering data. Specifically, the matrix elements for both E2 and E4 transitions have been used in a series of coupled channels calculations to relate the strengths of the various coupling routes

between levels. These matrix elements were calculated using the O(6) parameters of Reference [Ca 78]. The resulting fits to the data are quite good for the angular distributions populating states in the ground band up to $J^{\pi} = 4^{+}$ and for the second 2^{+} level. In most of the calculations the full set of matrix elements was used without any searches on a particular matrix element. An additional set of matrix elements was used for ^{194}Pt(p,p') to investigate the sensitivity of the CC calculations to the value of κ, the strength of the quadrupole-quadrupole force between bosons. The primary effect of a larger value of κ was to change a few small matrix elements, particularly the $0 \rightarrow 2^{+'}$ value, which improved the fit to the $2^{+'}$ angular distribution. It is important to note that the fits obtained in this study do not rely on any special "best fit" group of matrix elements from the O(6) limit, either from searching on energy levels and B(Eλ) values or from the CC searches. The sets used in these calculations were not determined individually for each nucleus, but were generated from one set, which is applicable in the entire Pt region with only a small mass dependence in the O(6) parameters. It would be worthwhile in the future to carry out these CC calculations with a better determined set of matrix elements from the IBA, preferably with the inclusion of neutron and proton bosons.

Nevertheless, the present calculations have provided sufficient information to confirm the results of earlier

inelastic scattering experiments, which found a negative value of P_3 is needed to fit the $2^{+'}$ data in ^{194}Pt. The present calculations also indicate $P_3 < 0$ for ^{196}Pt(p,p') as well, but there are some uncertainties in ^{198}Pt(p,p') that need further study. It is interesting to note that in each case the O(6) limit also gives a negative P_3 interference term.

The present study also is in agreement with recent α-scattering studies [Ba 78] that indicate a strong E4 transition is needed to account for the strength of the $4^{+'}$ angular distribution in ^{192}Pt. Although the magnitude for this matrix element has been determined, there is still some uncertainty in its sign due to the competing multistep E2 routes that can populate the $4^{+'}$ state. This sign discrepancy also results in a factor-of-2 uncertainty in the magnitude of $M_{04'}$ for ^{192}Pt [Ba 78]. It is unfortunate that the third 4^+ level seen in all three (p,p') reactions could not be included in the CC calculations, for these strongly excited states may be similar to those populated in ^{190,192}Os [Ba 77, Bu 78], which were interpreted as hexadecapole vibrational states. Considering the cross section for these states compared to that for the first and second 4^+ (including their rather large E4 component), this may indicate the possibility of a hexadecapole vibrational component in these states as well.

One question not addressed in this study was the influence on the CC calculations that would result from

including the 3^- level in the couplings. This level is one of the more strongly excited levels in each reaction and thus might be involved in a number of coupling routes. Since the IBA code PHINT also can calculate E1 and E3 matrix elements, it should be possible to determine B(E3) values for ^{194,196,198}Pt with a $0^+-2^+-3^-$ coupling scheme and study the effects of the 3^- level in more complex coupling schemes.

An additional feature of the CC calculations was the determination of moments for the deformed optical model potential. The method used to extract these values from the DOMP parameters proved to be most valuable in comparing the proton scattering values with moments determined by other methods. Many of the uncertainties and simplifications that were used in previous studies are overcome by this more fundamental method. Even though this method facilitates comparisons with other methods and gives moments that are in better agreement with the charge moments than an earlier (α,α') experiment, it is premature to draw any conclusions from the apparent discrepancies between the charge (proton) and potential (neutron) moments. More study is needed on the possible influences of factors mentioned in Chapter VI in determining the moments, such as βr scaling each potential and including the imaginary part of the DOMP.

There are also many interesting alternative approaches to the analysis of the inelastic proton scattering data that might provide additional insight into the nature of these

nuclei. For example, CC calculations could be performed using form factors from the vibrational model with either IBA or vibrational matrix elements. This type of analysis would provide E2 and E4 moments that are uncoupled. It would also be of interest to analyze the (p,p') data within the extended triaxial rotor model framework available in ECIS, much like that carried out in the ^{12}C-scattering study [Ba 79]. It is possible that a comparison of moments calculated from the same data with differently shaped potentials may provide information on the equilibrium shapes of these nuclei.

In summary, this study has extended the predictive properties of the O(6) limit of the IBA model in the Pt region to interpret the strengths and shapes of transitions seen in the (p,t) and (p,p') reactions. It is hoped that the success of the O(6) limit in the Pt region shown in this work and in [Ca 78, Ci 78] will spur continued interest in this new approach, based on the symmetries of collective intrinsic structure rather than their geometries, in understanding nuclei in several mass regions. And since this approach provides a uniform treatment for many aspects of most heavy even-even nuclei, there seem to be innumerable opportunities to test and extend this model.

LIST OF REFERENCES

LIST OF REFERENCES

A

[Ar 76] A. Arima and F. Iachello, Ann. Phys. (N.Y.) 99, 253 (1976).

[Ar 76a] A. Arima and F. Iachello, Phys. Rev. C14, 761 (1976).

[Ar 77] A. Arima, T. Ohtsuka, F. Iachello, and I. Talmi, Phys. Lett. 66B, 205 (1977).

[Ar 77a] A. Arima and F. Iachello, Phys. Rev. C16, 2085 (1977).

[Ar 78] A. Arima and F. Iachello, Ann. Phys. (N.Y.) 111, 201 (1978).

[Ar 78a] A. Arima and F. Iachello, Phys. Rev. Lett. 40, 385 (1978).

[As 70] R.J. Ascuitto and N.K. Glendenning, Phys. Rev. C2, 1260 (1970).

[As 72] R.J. Ascuitto, N.K. Glendenning, and B. Sorensen, Nucl. Phys. A183, 60 (1972).

[Au 70] N. Austern, Direct Nuclear Reaction Theories (Wiley-Interscience, New York, 1970).

B

[Ba 62] R.H. Bassel, G.R. Satchler, R.M. Drisko, and E. Rost, Phys. Rev. 128, 2693 (1962).

[Ba 71] B.F. Bayman, Nucl. Phys. A168, 1 (1971); B.F. Bayman and D.H. Feng, Nucl. Phys. A205, 513 (1973).

[Ba 73] H.W. Baer et al., Ann. Phys. (N.Y.) 76, 437 (1973).

[Ba 76] F.T. Baker, A. Scott, T.H. Kruse, W. Hartwig, E. Ventura, and W. Savin, Nucl. Phys. A266, 337 (1976).

[Ba 77] R.D. Bagnell, Y. Tanaka, R.K. Sheline, D.G. Burke, and J.D. Sherman, Phys. Lett. 66B, 129 (1977).

[Ba 78] F.T. Baker, A. Scott, R.M. Ronningen, T.H. Kruse, R. Suchannek, and W. Savin, Phys. Rev. C17, 1559 (1978).

[Ba 78a] C. Baktash, J.X. Saladin, J.J. O'Brien, and J.G. Alessi, Phys. Rev. C18, 131 (1978).

[Ba 79] F. Todd Baker et al., Nucl. Phys. A321, 222 (1979).

[Be 64] O. Bergman and G. Backstrom, Nucl. Phys. 55, 529 (1964).

[Be 69] F.D. Becchetti and G.W. Greenlees, Phys. Rev. 182, 1190 (1969).

[Be 69a] P.R. Bevington, Data Reduction and Error Analysis for the Physical Sciences (McGraw-Hill, New York, 1969).

[Be 70] G.D. Benson, A.U. Ramayya, R.G. Albridge, and G.D. O'Kelley, Nucl. Phys. A150, 311 (1970).

[Be 78] G. Berrier-Ronsin et al., Phys. Rev. C17, 529 (1978).

[Bj 66] J. Bjerregaard, O. Hansen, O. Nathan, and S. Hinds, Nucl. Phys. 86, 145 (1966).

[Bl 71] H.G. Blosser, G.M. Crawley, R. De Forest, E. Kashy, and B.H. Wildenthal, Nucl. Instr. Meth. 91, 61 (1971).

[Bo 53] A. Bohr and B.R. Mottelson, Mat. Fys. Medd. Dan. Vid. Selsk. 27, No. 16 (1953).

[Bo 69] A. Bohr and B.R. Mottelson, Nuclear Structure, Vol. 1, (Benjamin, New York, 1969).

[Br 70] E.J. Bruton, J.A. Cameron, A.W. Gibb, D.B. Kenyon, and L. Keszthelyi, Nucl. Phys. A152, 495 (1970).

[Br 73] R.A. Broglia, O. Hansen, and C. Riedel, Advances in Nuclear Physics, edited by M. Baranger and E. Vogt (Plenum Press, New York, Vol. 6, 1973) p. 287.

[Br 75] D. Breitig et al., Phys. Rev. C11, 546 (1975).

[Bu 78] D.G. Burke, M.A.M. Shahabuddin, and R.N. Boyd, Phys. Lett. 78B, 48 (1978).

C

[Ca 78] R.F. Casten and J.A. Cizewski, Nucl. Phys. A309, 477 (1978).

[Ca 78a] R.F. Casten, private communication.

[Ci 78] J.A. Cizewski et al., Phys. Rev. Lett. 40, 167 (1978).

[Ci 79] J.A. Cizewski and R.F. Casten, to be published.

[Cl 76] W.E. Cleveland and E.F. Zganjar, Z. Physik A279, 195 (1976).

[Co 59] B.L. Cohen, Rev. Sci. Instr. 30, 415 (1959).

[Co 72] J.R. Comfort, W.J. Braithwait, J.R. Duray, and S. Yoshida, Phys. Rev. Lett. 29, 441 (1972).

D

[Da 58] A.S. Davydov and G.F. Fillippov, Nucl. Phys. 8, 237 (1958).

[Da 60] A.S. Davydov and A.A. Chaban, Nucl. Phys. 20, 499 (1960).

[De 63] A. de Shalit and I. Talmi, Nuclear Shell Theory (Academic Press, New York, 1963).

[De 79] P.T. Deason, C.H. King, T.L. Khoo, J.N. Nolen, Jr., and F.M. Bernthal, to be published, Phys. Rev. C20, (1979).

[Do 77] F. Donau and S. Frauendorf, Phys. Lett. 71B, 263 (1977).

F

[Fa 65] A. Faessler, W. Greiner, and R.K. Sheline, Nucl. Phys. 70, 33 (1965).

[Fe 53] H. Feshbach, C.E. Porter, and V.F. Weisskopf, Phys. Rev. 90, 166 (1953); Phys. Rev. 96, 448 (1954).

[FIac] F. Iachello, private communication.

[Fi 72] M. Finger et al., Nucl. Phys. A188, 369 (1972).

[FKar] Targets prepared by Frank Karasek, Argonne National Laboratory.

[Fl 69] E. Flynn, D.D. Armstrong, J.G. Beery, and A.G. Blair, Phys. Rev. 182, 1113 (1969).

[Fr 75] S. Frauendorf and V.V. Pashkevich, Phys. Lett. 55B, 365 (1975).

[Fu 75] L. Funke et al., Phys. Lett. 55B, 436 (1975).

G

[Ga 69] G.T. Garvey et al., Rev. Mod. Phys. 41, Part II, S1 (1969).

[Gl 62] N.K. Glendenning, Nucl. Phys. 29, 109 (1962).

[Gl 67] N.K. Glendenning, Proc. Int. School of Physics "Enrico Fermi", Course XL (1967), edited by M. Jean (Academic Press, New York, 1969) p. 332.

[Gl 68] J.E. Glenn and J.X. Saladin, Phys. Rev. Lett. 20, 1298 (1968).

[Gl 69] J.E. Glenn, R.J. Pryor, and J.X. Saladin, Phys. Rev. 188, 1905 (1969).

[Gn 71] G. Gneuss and W. Greiner, Nucl. Phys. A171, 449 (1971).

[Go 72] U. Gotz, H.C. Pauli, K. Alder, and K. Junker, Nucl. Phys. A192, 1 (1972).

[Gr 68] L.V. Groshev, A.M. Demidov, and A.S. Rakimor, Sov. J. Nucl. Phys. 7, 563 (1968).

H

[Ha 77] J.K. Hamilton and R.S. Mackintosh, J. Phys. G. Nucl. Phys. Vol. 3, No. 2, L19 (1977); Vol. 4, No. 4, 557 (1978).

[HDav] SCOPEFIT, unpublished, written by H. David, Michigan State University.

[He 68] D.L. Hendrie et al., Phys. Lett. 26B, 127 (1968).

[Hj 76] S.A. Hjorth et al., Nucl. Phys. A262, 328 (1976).

I

[Ia 78] F. Iachello, Comments Nucl. Part. Phys. Vol. 8, No. 2, 59 (1978).

J

[Ja 68] J.F.W. Jansen, H. Pauw, and C.J. Toest, Nucl. Phys. A115, 321 (1968).

[JRCo] AUTOFIT, unpublished, written by J.R. Comfort, Argonne National Laboratory.

K

[Ki 72] T. Kishimoto and T. Tamura, Nucl. Phys. A192, 247 (1972).

[Ki 72a] C.H. King, R.J. Ascuitto, N. Stein, and B. Sorensen, Phys. Rev. Lett. 29, 71 (1972).

[Ki 76] T. Kishimoto and T. Tamura, Nucl. Phys. A270, 317 (1976).

[Ki 78] C.H. King, G.M. Crawley, J.A. Nolen, Jr., and J. Finck, J. Phys. Soc. Japan 44, 564 (1978).

[Ki 79] C.H. King et al., to be published.

[Kr 77] K. Krien, I.C. Oelrich, R.M. Del Vecchio, and R.A. Naumann, Phys. Rev. C15, 1288 (1977).

[Ku 68] K. Kumar and M. Baranger, Nucl. Phys. 122, 273 (1968).

[Ku 69] K. Kumar, Phys. Lett. 29B, 25 (1969).

L

[La 73] W.A. Lanford and J.B. McGrory, Phys. Lett. 45B, 238 (1973).

[La 77] W.A. Lanford, Phys. Rev. C16, 988 (1977).

[Le 76] G. Leander, Nucl. Phys. A273, 286 (1976).

[Le 77] I.Y. Lee et al., Phys. Rev. Lett. 39, 684 (1977).

M

[Ma 72] J.V. Maher, J.R. Erskine, A.M. Friedman, and R.H. Siemssen, Phys. Rev. C5, 1380 (1972).

[Ma 74] J.V. Maher et al., Bull. Am. Phys. Soc. 19, 104 (1974).

[Ma 74a] R.S. Mackintosh and L.J. Tassie, Nucl. Phys. A222, 187 (1974).

[Ma 75] R.G. Markham and R.G.H. Robertson, Nucl. Instr. Meth. 129, 131 (1975).

[Ma 76] R.S. Mackintosh, Nucl. Phys. A266, 379 (1976).

[Me 75] J. Meyer-ter-Vehn, Nucl. Phys. A249, 111, 141 (1975).

[Mi 71] W.T. Milner et al., Nucl. Phys. A177, 1 (1971).

[Mu 65] P. Mukherjee, Nucl. Phys. 64, 65 (1965).

N

[No 75] J.A. Nolen, Jr. and P.S. Miller, Proc. 7th Int. Conf. on Cyclotrons and Their Applications (Birkhausser, Bassel, 1975) p. 249.

[No 78] J.A. Nolen, Jr., M.S. Curtin, and T.E. Dyson, Nucl. Instr. Meth. 150, 581 (1978).

[Ny 66] B. Nyman, A. Johansson, D. Bergman, and G. Backstrom, Nucl. Phys. 88, 63 (1966).

O

[OSch] Calculations performed by Olaf Scholton, KVI, Gronningen, The Netherlands.

P

[Pr 70] R.J. Pryor and J.X. Saladin, Phys. Rev. C1, 1573 (1970).

[Pa 77] V. Paar, Ch. Vieu, and J.S. Dionisio, Nucl. Phys. A284, 199 (1977).

[PDKu] DWUCK, unpublished, written by P.D. Kunz, University of Colorado.

[Pr 75] M.A. Preston and R.K. Bhaduri, Structure of the Nucleus (Addison-Wesley, Reading, Mass., 1975).

R

[Ra 72] J. Raynal, Computing as a Language of Physics, IAEA-SM3-918, Vienna (1972) p. 281.

[Ra 73] ECIS, unpublished, written by J. Raynal, Saclay, France.

[Ra 75] J.O. Rasmussen, Nuclear Spectroscopy and Reactions, Part D, edited by J. Cerny (Academic Press, New York, 1975) p. 97.

[RCMe] R.C. Melin and J.A. Nolen, Jr., to be published.

[Ro 57] M.E. Rose, Elementary Theory of Angular Momentum (Wiley, New York, 1957).

[Ro 77] R.M. Ronningen et al., Phys. Rev. C16, 571 (1977).

S

[Sa 64] G.R. Satchler, Nucl. Phys. 55, 1 (1964).

[Sa 68] C. Samour et al., Nucl. Phys. A121, 65 (1968).

[Sa 72] G.R. Satchler, J. Math. Phys. 13, 1118 (1972).

[Sa 77] S.K. Saha et al., Phys. Rev. C15, 94 (1977).

[Sa 79] A. Saha and H.T. Fortune, Phys. Rev. C19, 2065 (1979).

[Sc 77] PHINT, unpublished, written by O. Scholten, KVI, Gronningen, The Netherlands.

[Sc 78] O. Scholten, F. Iachello, and A. Arima, Ann. Phys. (N.Y.) 115, 325 (1978).

[Sh 76] H.L. Sharma and N.M. Hintz, Phys. Rev. C13, 2288 (1976).

[Sm 77] G.R. Smith, N.J. DiGiacomo, M.L. Munger, and R.J. Peterson, Nucl. Phys. A290,72 (1977).

[St 77] K. Stelzer et al., Phys. Lett. 70B, 297 (1977).

[Su 68] A.W. Sunyar, G. Scharff-Goldhaber, and M. McKeown, Phys. Rev. Lett. 31, 237 (1968).

T

[To 61] W. Tobocman, Theory of Direct Nuclear Reactions (Oxford University Press, London, 1961).

[To 76] H. Toki and Amand Faessler, Z. Physik A276, 35 (1976).

U

[Ud 74] T. Udagawa, Phys. Rev. C9, 270 (1974).

V

[Va 71] J. Vary and J.N. Ginocchio, Nucl. Phys. A166, 479 (1971).

[Ve 76] M. Vergnes, INS Symposium on Collectivity of Medium and Heavy Nuclei, Tokyo (1976).

[Ve 78] M. Vergnes et al., Journal de Physique-Letters 17, 291 (1978).

W

[Wi 56] L. Wilets and M. Jean, Phys. Rev. 102, 788 (1956).

Y

[Ya 63] T. Yamazaki, Nucl. Phys. 49, 1 (1963).

[Ya 74] S.W. Yates, J.C. Cunnane, R. Hochel, and P.J. Daly, Nucl. Phys. A222, 301 (1974).

[Ya 76] Y. Yamazaki and R.K. Sheline, Phys. Rev. C14, 531 (1976).

[Ya 78] Y. Yamazaki, R.K. Sheline, and E.B. Shera, Phys. Rev. C17, 2061 (1978).

[Ya 79] S.W. Yates, private communication.